Novel Approach for Designing Dual-Band 5G Antenna Integrated Reflector

By

Mohammad Faridani

A thesis presented to the Ottawa Carleton Institute for Electrical and Computer Engineering
in partial fulfillment to the thesis requirement for the degree of

Doctor of Philosophy

in

Electrical and Computer Engineering

uOttawa

L'Université canadienne
Canada's university

University of Ottawa

Ottawa, Ontario, Canada

Abstract

As the world continues to adopt the next generation of mobile technology, dual-band 5G wireless communications are becoming increasingly significant. 5G technology operates on two different frequency bands, the sub-6 GHz Frequency Range (FR1) and the millimeter wave (MMW) Frequency Range (FR2).

The special features in each band enable 5G dual-band communication to provide better coverage and capacity than previous generations of wireless networks. This is especially essential for applications that need high-bandwidth and low-latency connections, such as virtual and augmented reality, autonomous vehicles, and industrial automation. Furthermore, dual-band 5G can help alleviate network congestion in urban areas by redirecting traffic to the MMW band, which has considerably greater capacity. As a result, dual-band 5G is expected to play a critical role in facilitating the next wave of technological innovation and revolutionizing the way we live and work. A dual-band antenna with a large frequency ratio (FR) is required due to the significant difference between each frequency band in 5G.

Research on dual-band antennas is facing challenges such as low FR and a lack of a specific design methodology. Despite attempts to develop dual-band antennas with large FRs, there are still issues with low performance and limited bandwidth.

This study introduces a novel approach for designing a dual-band antenna with a large FR. The proposed solution draws inspiration from a hybrid design of a dual-band antenna to achieve a large FR, and from the parabolic reflector antenna design to significantly enhance gain in the upper band. The lower band antenna in this design serves as both a radiator for the lower band and a reflector to align the beam in the upper band. This approach can be used to design dual-band antennas for various frequencies.

In this thesis, we present a comprehensive model and framework for designing an antenna integrated reflector that offers a large FR. The proposed model is capable of producing an antenna that meets the requirements of the targeted application, namely 5G. This antenna exhibits wideband characteristics and high gain.

Two different antenna integrated reflectors, named AIR-I and AIR-II, were designed based on the proposed model. AIR-I has a FR of 10.1. As for AIR-II, due to the presence of dual-band upper antennas, it has a lower band at 1.35 GHz and two upper bands at 13 GHz and 24 GHz thus, a FR of 9.5 and 18, respectively.

The above design followed a specific purpose. It uses a 24 GHz/1.35 GHz frequency ratio of 18 to showcase the antenna performance in the context of dual-band 5G. However, the measurement facilities being limited to 20 GHz, a frequency ratio of 9.5 at 13 GHz/1.35 GHz was measured for the AIR-II, as proof of concept. Then, two prototypes were fabricated from AIR-II namely, Prototype-I and Prototype-II. While it would have been possible to demonstrate a proof of concept from a single prototype, it has been decided to produce and test two samples to enable a more exhaustive examination of the subject and obtain additional data that would lend greater support to the model outlined in this thesis.

Prototype-I had the same structure as AIR-II and had an operational bandwidth of 0.69 GHz–1.74 GHz / 6 GHz–18 GHz and a FR of 9.9. On the other hand, Prototype-II had an operational bandwidth of 0.69 GHz–1.74 GHz / 13 GHz–18 GHz and a FR of 12.8. These prototypes exhibited maximum bandwidths of 100% and 86%, respectively. Furthermore, at the upper band, Prototype-I achieved a peak gain improvement of 12.6 dB, while Prototype-II achieved an improvement of 8.7 dB. These results demonstrated the significant advantages of our proposed methodology in dual-band antenna design.

Contents

List of Figures

List of Tables

List of Symbols

A	Vector potential
$\widehat{a_z}$	Unit vector in the z-direction
D	Reflector diameter
σ	Radar cross section
f	Operational Frequency
f_r	Resonant frequency
f_H	Highest operating frequency
f_L	Lowest operating frequency
f_c	Central operating frequency
$\mathrm{G}_{\mathrm{dipole}}$	Dipole antenna gain
I_0	Constant electric current
G_R	Receiver antenna gain
G_R	Transmitter antenna gain
P_T	Transmitted power
P_R	Received power
P_{Dr}	power density of the scattered wave at the receiving radar
ε	Dielectric constant
ε_r	Effective dielectric constant
ω_r	Angular resonant frequency
λ	Wavelength
λ_{gl}	Guided wavelength
μ	Permeability
η	Antenna aperture efficiency
p	Normalized radiation pattern
U	Radiation intensity
v_0	Velocity of light in free space
y'	First derivative of y

List of Acronyms

3G	Third Generation of Wireless Mobile Telecommunications Technology
4G	Fourth Generation of Broadband Cellular Network Technology
5G	Fifth Generation of Mobile Networks New Radio
AEP	Advanced Electronics and Photonics Research Centre
AF	Array Factor
AMD	Advanced Micro Devices
APT	Asia-Pacific Telecommunity
AUT	Antenna Under Test
AWS	Advanced Wireless Services
BDMA	Beam-Division Multiple-Access
BLE	Bluetooth Low Energy
BW	Bandwidth
CBCPW	Conductor-Backed Coplanar Waveguide
CDMA	Code-Division Multiple Access
CPW	Coplanar Waveguide
CPWG	Coplanar Waveguide with Ground
CRR	Closed Ring Circuits
CST	Computer Simulation Technology
DD	Frequency Division Duplex
DGS	Defected Ground Structure
DMC-MSL	Dual-Mode Composite Microstrip Line
DR	Dielectric Resonator
EBG	Electromagnetic Band Gap
EHF	Extremely High Frequency
ESD	Electrostatic Discharge
FBW	Fractional Bandwidth
FCC	The Federal Communications Commission
FHD	Full High Definition
FR	Frequency Ratio
FR1	Frequency Range 1
FR2	Frequency Range 2

FSS	Frequency Selective Structures
GPR	Ground-Penetrating Radar
GPS	Global Positioning System
GW	Gap Waveguide
HD	High Definition
HDMI	High Definition Multimedia Interface
HDTV	High Definition Television
IEEE	Institute of Electrical and Electronics Engineers
IoE	Internet of Everythings
IoT	Internet of Things
ISM	Industrial, Scientific, and Medical
LED	Light-Emitting Diode
LoRa	Long Range
LoS	Line-of-Sight
LTE	Long-Term Evolution
LW	A Leaky-Wave Antenna
M2M	Machine-to-Machine
MMW	Millimeter-Wave
NRC	National Research Council Canada
OP	Orthogonal Polarization
OSL	Open - Short - Load
PCB	Printed Circuit Board
PET	Polyethylene Terephthalate
PLA	Polylactic Acid
PP	Principal Polarization
PS	Public Safety
RAM	Random-Access Memory
RCS	Radar Cross Section
RF	Radio Frequency
RLC	Resistor-Inductor-Capacitor
Rx	Receiver
SIW	Substrate Integrated Waveguide
SLL	Side Lobe Level
SMA	Sub Miniature version A

SNR	Signal to Noise Ratio
SRR	Split Ring Resonator
SW-SIW	Slow-Wave Substrate Integrated Waveguide
TDD	Time Division Duplex
TE	Transverse Electric
TM	Transverse Magnetic Wave
Tx	Transmitter
UV	Ultraviolet
UWB	Ultra-Wideband
V2I	Vehicle-to-Infrastructure
V2V	Vehicle-to-Vehicle
VNA	Vector Network Analyzer
WG-MTM	Waveguided Metamaterial
WiFi	Wireless Fidelity
WiGig	Wireless Gigabit Alliance
WPAN	Wireless Personal Area Network

Chapter 1 - Introduction

1.1 Motivations

As antennas remain one of the key elements in transmitting/receiving data, their design is critical to enhance the whole communication system performance. A dual-band antenna is an antenna that has been specifically designed to operate across two different frequency ranges. This type of antenna is capable of transmitting and receiving signals at two distinct frequencies, which can be particularly useful for communication systems that require access to different frequency bands such as 5G systems [1].

Dual-band wireless communication systems are those that utilize two distinct frequency bands for wireless communication. The purpose of incorporating two distinct frequency bands is to enhance the effectiveness of wireless communication systems. Each frequency band possesses its unique set of advantages and disadvantages.

These systems are in demand because firstly, there is an increased bandwidth as two frequency bands are available for communication. This leads to the transmission of more information at once, resulting in faster communication speeds [2].

Secondly, dual-band communication improves reliability by reducing interference and signal degradation, which may cause dropped calls and poor connection quality [3]. Using two different frequency bands allows the system to switch to the other band if one band experiences interference, improving overall reliability [4].

Thirdly, dual-band communication increases flexibility in terms of network design and deployment. For instance, a system can use one band for short-range communication and the other one for longer-range communication, enabling more efficient use of resources [5].

However, while talking about dual-band antennas, their frequency ratio (FR), defined as the ratio of the upper band frequency central frequency divided by the lower band frequency, is one of the key parameters to consider. In fact, FR plays a significant role in the development of dual-band antennas as it sets the distance between the resonant frequencies of each frequency band.

If one of the early applications of a dual-band antenna was to cover the 2.4 GHz/5 GHz bands [6], which did not require a high frequency range (FR), recent applications for dual-band microwave and millimeter-wave (MMW) wireless communications [7], as well as 5G applications at sub-6 GHz and above 24.5 GHz [8, 9], have spurred extensive research into designing a dual-band antenna with a large FR [10].

1.2 Problem Statement

There exist different techniques to design a dual-band antenna such as hybrid structure [11], aperture-coupled patches [12], dual-feed designs, and fractal antenna design [13]. Hybrid structure has a higher radiation efficiency compared to other methods [14].

A hybrid structure in a dual-band antenna refers to a design that enables the antenna to operate effectively on two distinct frequencies. The high radiation efficiency of this method is because each of the two radiation elements oversees a different frequency band [14].

Typically, this involves the integration of two different types of radiating elements within the same antenna structure, each of them being optimized for a specific frequency band to ensure good performance characteristics [15].

Raising the FR, however, poses a challenge to antenna designers, as it necessitates a clear separation between the resonant frequencies of each band and the inclusion of multiple resonant modes. The antenna's structure and design techniques will be determined by the desired FR and the particular application's demands [14]. However, even if the hybrid structure remains one of the best approaches to achieve a high FR, achieving an FR higher than 3 is still challenging, as highlighted in [16].

In [12], the authors presented a single-feed dual-band aperture-coupled antenna designed for 5G applications. The antenna utilizes the aperture slot to operate as a dual-band radiator, providing independent resonators that allow for flexible frequency scaling. The first band operates at 28 GHz, while the second band operates at 38 GHz.

Upper and lower band antennas were designed separately in [17], and each one was fed directly by a microstrip feed line. Separate array antennas for dual-band LTE and 5G were designed on the same substrate, and each of them was fed separately [18]. A large fractional bandwidth of 6.2 was achieved in [19] by employing a vertical stack of frequency selective structures (FSS).

In [20], an FR of 1.6 for X and Ku band applications was achieved by using a square ring and a patch with slots on it. [21] achieved an FR of approximately 4 for Offset-Fed X and Ka Band Reflectarray using thin membranes. [22] achieved an FR of around 2 by utilizing a separated feed and constructing the element from a split ring with two phase delay lines and a phoenix patch.

Although the current methods have achieved a FR of around 4, they do not meet the required FR for dual-band applications in 5G FR1/FR2 bands, i.e., a FR ≥ 8 (i.e., with FR1 n78 band at 3.5 GHz and FR2 band n261 at 28 GHz, leading to a $f1/f2 = FR \geq 8$ [23]).

So, one of the main challenges in designing a dual-band antenna for 5G systems remains achieving the desired bandwidth for frequency bands that have a high FR [24, 25]. This challenge arises because the bandwidth of each band often differs, and creating an antenna that operates efficiently over a wide frequency range can be a difficult task. Consequently, dual-band antennas often suffer from low bandwidth [26].

A Co-Aperture Planar structure was employed in [27] to achieve a maximum bandwidth of 9%. However, only a bandwidth of less than 2% was attained using 8 Loop Antenna Elements in [28] and the metasurface-based decoupling technique in [24].

A sub-6 GHz antenna with a filtering structure, described in [29], was able to achieve a bandwidth of 9%, while a waveguided metamaterial (WG-MTM) antenna in [25] achieved a bandwidth ≤ 2%.

One of the challenges in a hybrid structure, where each antenna is separately designed, is how to ensure efficient operation in close proximity. Consequently, the presence of the other antenna can decrease the performance of each antenna, including gain and bandwidth [30].

When designing an antenna, the radiation pattern is another crucial aspect that must be taken into consideration. In a stacked configuration, the interaction between antennas can result in a complex radiation pattern. To ensure that the desired pattern is achieved, designers must meticulously analyze the radiation pattern of each antenna and factor in the effects of mutual coupling [31].

1.3 Proposed Design Approach

To address the issues listed above and achieve high gain, reflector antennas have been first considered.

A reflector antenna is a type of antenna that utilizes a metal surface (known as a reflector) to concentrate or redirect radio waves onto a single point, where a transmitter or receiver is positioned. A reflector can effectively increase antenna gain by redirecting energy that would otherwise be radiated in unwanted directions, thereby improving the antenna's efficiency. The use of a reflector also reduces the amount of energy that is radiated towards the ground or into the sky, which are not of interest. As a result, more of the radiated energy is directed towards the desired location, such as a distant receiver or satellite [32].

There are different configurations of reflectors, including the flat reflector, which is a simple planar surface placed behind the antenna's radiating element. This reflector is easy to manufacture and commonly used in applications where a relatively simple radiation pattern is desired [33].

Another type of reflector is the corner reflector, consisting of two flat reflectors that meet at a 90-degree angle, forming a corner. The radiating element is located at the corner's apex. This reflector is often used in radar and communication systems that require high gain and wide beamwidth [34].

Parabolic reflectors are also commonly used and they are the most popular ones [35], consisting of a curved surface shaped like a paraboloid of revolution. The radiating element is located at the reflector’s focal point. This reflector is often used in high-gain antennas [36].

To obtain a dual-band reflector antenna, the feed must be able to support two frequency bands. One option is to use a dual-band antenna as the feed for the reflector. However, this approach still has the same drawbacks as dual-band antennas.

Another option is to use separate feeds for each band. In this case, two feed antennas are placed at the reflector's focal point. However, adding another antenna to the feed system would block the reflector surface and reduce the reflector antenna's gain, which is known as feed blockage.

Other disadvantageous of the parabolic antenna is the size, weight, and high fabrication cost. The parabolic reflector is a solid piece of metal which has a significant weight and this can make it difficult to install or use in certain applications. Also because of the manufacturing process of the parabolic dish they can be costly compared to other antennas.

So, to solve some of the issues raised by reflector antennas, a new type of antenna called the reflect array antenna was introduced [37]. While both antennas use reflection to direct electromagnetic waves, they differ in their design and construction.

A reflectarray antenna utilizes a flat surface consisting of an array of small reflectors, typically metal patches or dipoles, to reflect and concentrate electromagnetic waves. The elements within the array can be controlled electronically to adjust the phase and amplitude of the reflected waves, which, in turn, creates a desired radiation pattern that can be directed in various directions [38].

To achieve dual bandwidth in a reflectarray antenna, both the feed and the reflectarray elements must have dual bandwidth capability. This can be accomplished through the implementation of two methods. The first method involves using two sets of reflectarray elements for dual-band operation [21]. The second method involves utilizing dual-band reflectarray elements [20].

The proposed approach will use a reflector to function as the lower band antenna. This is because the reflector is larger in size than the feed, and the physical size of the lower band antenna is larger compared to the upper one. The substantial difference in size between the reflector and feed should enable our model to achieve a large FR.

1.4 Contributions

The research described in this thesis focuses on providing methods to design a new type of dual-band antenna. This novel antenna could offer a solution for applications that require a large FR.

The proposed approach is inspired by the hybrid dual-band antenna structure, which enables the creation of a dual bandwidth. It is also inspired by the reflector/reflectarray antenna structure, which allows for achieving high gain at the upper band. Our antenna will be specifically designed for 5G dual-band FR1 and FR2 applications.

Here are the lists of PhD contributions and significant achieved results:

1. The development of a new dual-band antenna design approach that involves combining a hybrid dual-band antenna structure with a reflector/reflectarray structure. Similar to a hybrid structure, there is one distinct antenna that is responsible for radiating at each frequency. However, like a reflector antenna, it includes both a reflector and feed. In this case, the lower band antenna is similar to a traditional parabolic reflector, while the upper band antenna is a feed. The large FR is a result of the hybrid structure, while the directive gain at the upper band is due to the reflector properties.
   Note that the proposed technique with an integrated reflector could be adjusted to operate at any desired frequency with large FR.
2. The exceeding of the FR forecasts (i.e., FR ≥ 8) by designing two antenna integrated reflectors with a FR of 10 and 18.
3. The development of a step-by-step approach that allows improving the antenna performance and structure through a series of steps supported by calculations and theory, from the basic model to the final prototype, suitable for 5G dual-band applications.

This work has resulted in the following publications:

1. M. Faridani, G. Xiao, R. E. Amaya, N. Javanbakht, and M. C. E. Yagoub, “A Kapton-Based Flexible Wideband Antenna with Metamaterial Resonators for Millimeter-Wave Wireless Applications,” IEEE International Symposium on Antennas and Propagation and USNC-URSI Radio Science Meeting (APS/URSI), 2021, pp. 1055–1056.
2. M. Faridani, G. Xiao, R. E. Amaya, and M. C. E. Yagoub, “A Compact Beam-Steerable Integrated Reflectarray Antenna for LEO Applications,” IEEE 19th International Symposium on Antenna Technology and Applied Electromagnetics (ANTEM), 2021, pp. 1–2.
3. Y. Liu, M. Faridani, and M. C. E. Yagoub, “Compact Wideband Linear Antenna Array Using Substrate Integrated Waveguide Cavity for 5G Communication Systems,” IEEE MTT-S International Conference on Numerical Electromagnetic and Multiphysics Modeling and Optimization (NEMO), 2020, pp. 1–4.
4. M. Faridani, M. C. E. Yagoub, and R. E. Amaya, “Novel Body Matched Millimeter-Wave Sandwiched Antenna for Advanced Medical Communications,” in 2020 International Conference on Microwave and Millimeter Wave Technology (ICMMT), 2020, pp. 1–3.
5. M. Faridani and M. C. E. Yagoub, “12-Element Wideband Microstrip Array Antenna for High Data Rate Terahertz Communications,” Optik (Stuttg)., vol. 171, 2018.
6. M. Faridani and M. C. E. Yagoub, “Novel Planar Wideband Antenna Integrated with Compact Flat Reflector for Millimeter-wave Communications,” Fifth International

Conference on Millimeter-Wave and Terahertz Technologies (MMWaTT), 2018, pp. 31–33.

1.5 Thesis Outline

Chapter 2 first broadly reviewed the subject of 5G and the new applications of this technology. The chapter discussed why it is important to have a large FR for 5G dual applications and delved into the different categories of 5G and the unique specifications of each frequency band. By gaining an understanding of the target applications and specifications of these frequency bands, the research can proceed.

Next, the chapter introduced the basic concepts and formulas of the parabolic reflector antenna. This antenna structure will be used in our antenna design to mimic the parabolic reflector shape and achieve a high gain. Subsequently, the chapter goes through the patch and monopole antennas, which will be utilized in our final antenna design for each band. The chapter then presents a broad review of the state of the art of dual-band antennas, with a focus on those with a large FR. This study helped us to understand the different techniques used to design a dual-band antenna, and enabled us to choose the most appropriate one for our model.

Chapter 3 focuses on the theory behind the proposed antenna. It begins by presenting the first model of our dual-band antenna with an integrated reflector, and then goes through a series of steps to improve its performance and structure towards the application goal. Each improvement step is supported by calculations and basic electromagnetic theory, until the proposed antenna structure with an integrated reflector is designed for any desired frequency.

Chapter 4 is centered on implementing our model, where a lower-band and upper-band antenna are designed for specific frequency bands. They are then placed in the model presented in Chapter 3 to create the final dual-band antennas. The performance of the last designed antenna is optimized for frequencies under 20 GHz in preparation for fabrication.

Chapter 5 discusses the fabrication and measurement of two prototypes in the antenna labs. A comparison is presented between the simulation and measurement results, and the performance of our antennas is also compared with those of existing antennas in the literature.

Chapter 6 discusses potential future extensions to the present work. It argues that the thesis contributes to the development of new dual-band wireless systems that require a large FR.

Chapter 2 – Background and Literature Review

In this chapter, we present the basic background concepts and calculations that are essential for understanding the proposed dual-band system model. It begins by introducing the basics of 5G wireless technology and its practical applications. From there, the discussion delves into the topic of reflector antennas, exploring their structures and the effects of some parameters on their performance.

Next, the chapter covers the operation of patch antennas and they use in wireless communication systems. This is followed by an in-depth exploration of microstrip antennas, another key area of study in wireless communication technology. Finally, dual-band antennas are introduced, with a focus on large frequency ratio (FR).

Then, a literature review on dual-band antennas was conducted while comparing our proposed antenna with state-of-the-art antennas. This allowed comprehending the techniques utilized in designing dual-band antennas and how to address the current drawbacks to increase their FR.

2.1 Fifth-generation mobile network (5G)

The fifth generation of mobile network technology, 5G, is anticipated to deliver faster and more dependable wireless connectivity, lower latency, and greater network capacity in comparison to earlier generations. Its potential to revolutionize a variety of industries, including healthcare, transportation, and entertainment, has been widely acknowledged [39].

Two major bands, MMW (millimeter wave) and Sub-6 GHz (low-band and mid-band frequencies), form the basis of 5G technology. The MMW frequency band, with its high speed, high capacity, and low latency, is accompanied by a shorter range and susceptibility to obstacles. On the other hand, the Sub-6 GHz frequency band has a longer range, greater coverage, and better obstacle penetration. However, it offers lower speed and capacity [40].

5G technology offers numerous advantages over previous wireless technologies. Faster download and upload speeds, greater network capacity, and lower latency enable the creation of new and innovative applications in fields such as enhanced mobile broadband, Internet of Things (IoT) [41], and mission-critical communications [42]. For example, 5G's high bandwidth and low latency make it possible to stream 4K and 8K videos and support virtual and augmented reality applications. Additionally, it allows for real-time communication between connected devices, which is critical for mission-critical applications such as autonomous vehicles and remote surgery.

The implementation of 5G technology is not straightforward. One of the most significant obstacles is a lack of infrastructure. The MMW frequency band necessitates a denser network of small cells and antennas to provide sufficient coverage and capacity, necessitating significant infrastructure and technology investments. Furthermore, the shorter range of the MMW frequency band makes deployment in rural areas challenging [43].

Another challenge is the security and privacy of data transmitted over 5G networks. The increased connectivity and data transfer rate of 5G networks make them more vulnerable to cyberattacks. Therefore, robust security and privacy protocols are required to protect sensitive data [44].

In wireless communications, 5G has significant advantages over 4G [45]: it is a new global wireless standard supposed to be up to 100 times faster than 4G and not limited to cellular phones and laptops like 4G. As Ericsson claimed, 5G will transfer industries and significantly improve day-to-day activities [46], as schematically shown in Fig 2-1. It will make some wireless communications more practical, e.g. Vehicle-to-Infrastructure (V2I) [47], Vehicle-to-Vehicle (V2V) [48], and Machine-to-Machine (M2M) [49]. Compared to the previous generation, 5G has more advantages in channel access method to cover multiple access. It supports not only Code-Division Multiple Access (CDMA), the same as 3G and 4G, but also Beam-Division Multiple-Access (BDMA), which simultaneously transfers data to various users by multi-separated based station antenna beam. As shown in Fig. 2-2, each user (mobile station) communicates with the base station separately when they are in the Line-of-Sight (LoS).

5G has an advantage over 4G in terms of lower latency, which is the time it takes for data to travel from one point to another. Low latency is crucial for applications like gaming, virtual reality, and remote surgery. While 5G can reduce latency to as low as one millisecond, 4G typically has a latency of around 50 milliseconds. This reduced latency enables real-time communication between devices, which is essential for applications such as autonomous vehicles or industrial control systems [50, 51].

Additionally, 5G can support a significantly larger number of connected devices per square kilometer compared to 4G. With 5G, up to one million devices can be connected, while 4G can only support up to 100,000 devices. This increased capacity is particularly useful in wireless applications where there may be a high density of devices, such as in a shopping mall or factory [52].

Finally, 5G operates at higher frequencies than 4G, enabling it to transmit more data in a shorter amount of time. However, 5G's higher frequency also results in a shorter range than 4G, making it easier to block by obstacles like buildings or trees. Nevertheless, this can be advantageous in wireless communications as it allows for more precise and targeted communication between devices and creates greater security in point-to-point communications [53, 54].

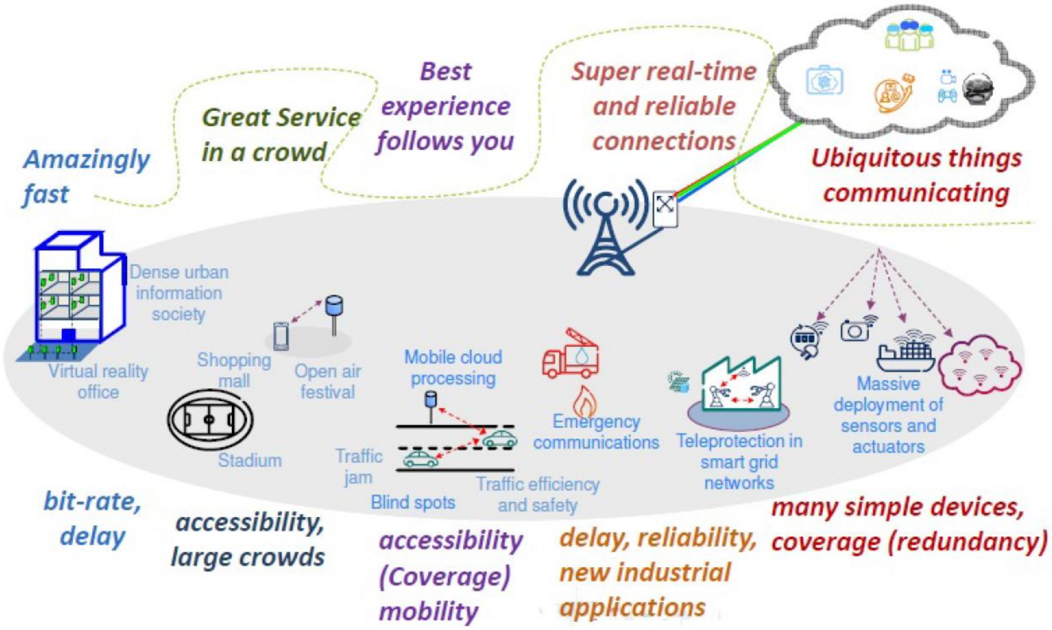

Figure 2-1 Some applications and advantages of 5G wireless systems [55]

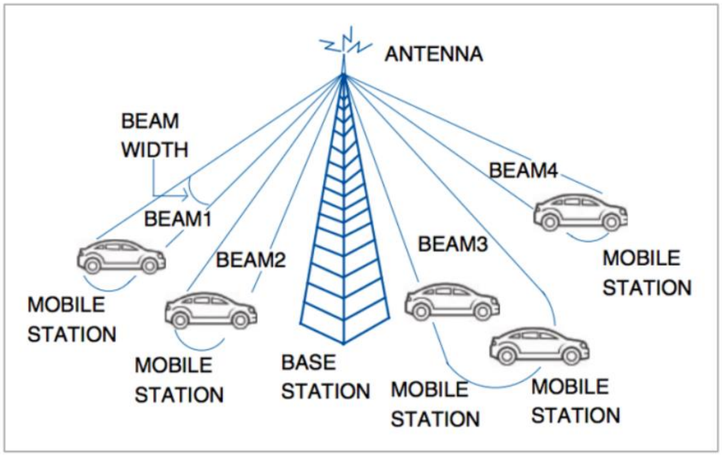

Figure 2-2 5G BDMA multiple access [56]

2.1.1. 5G Frequency Range 1 (FR1)

FR1 is the lower frequency spectrum employed in 5G wireless communication. This frequency range spans frequencies from 410 MHz to 7.125 GHz and is also known as sub-6 GHz spectrum. Despite the fact that the 5G FR1 frequency is not significantly higher than 4G - for example, 4G operates at 2.5 to 2.69 GHz [57] - it still offers faster connection speeds due to its wider bandwidth, which is approximately 6.5 GHz.

As the frequency of wireless connections increases, the coverage area decreases while the connection speed improves. This frequency range provides a favorable balance between coverage and capacity, rendering it appropriate for both urban and rural areas [58].

One of the key advantages of 5G FR1 is its ability to employ advanced technologies like beamforming and Massive MIMO. Beamforming is a technique that focuses radio waves in a specific direction, thereby enhancing signal strength and minimizing interference [59]. This is especially valuable in densely populated urban areas where buildings and other obstacles can obstruct or reflect radio waves.

2.1.2. 5G Frequency Range 2 (FR2)

The 5G FR2 band covers the frequency spectrum from 24.25 GHz to 52.6 GHz. It operates at a higher frequency than the FR1 band, which results in a higher available bandwidth but shorter range [23].

The first sub-band, n257, operates in the frequency range of 26.5 GHz to 29.5 GHz and is particularly useful in densely populated areas, such as urban environments, where it can provide high-bandwidth connections. It is also ideal for supporting high-speed mobile broadband services, such as 4K video streaming and virtual reality applications [23].

The second sub-band, n258, operates in the frequency range of 24.25 GHz to 27.5 GHz and is suitable for providing high-bandwidth, low-latency connections in indoor environments. This sub-band is particularly advantageous in smart homes, where it can facilitate the rapid transfer of large volumes of data between devices [23].

The third sub-band, n260, operates in the frequency range of 37 GHz to 40 GHz and has a wider bandwidth than the other sub-bands in FR2. This makes it well-suited for applications that require ultra-high-speed data transfer like augmented reality and 8K video streaming. However, its shorter range and higher susceptibility to interference make it more suitable for outdoor use [23].

The fourth and final sub-band, n261, operates in the frequency range of 27.5 GHz to 28.35 GHz and is particularly effective in small indoor areas, such as offices or homes. It provides high-bandwidth, low-latency connections and is suitable for supporting applications that require low latency, such as gaming and virtual reality [23].

Collectively, the FR2 sub-bands offer a range of capabilities that are suitable for diverse applications. These sub-bands play a crucial role in the development of 5G technology, supporting high-speed broadband in urban environments and low-latency connections in indoor settings. As the rollout of 5G continues to expand, it is expected that these sub-bands will play an increasingly important role in facilitating a wide range of applications and use cases [60, 61].

2.2 Millimeter-Wave (MMW) Band

As the 5G FR2 operates at the millimeter-wave (MMW) frequency band, it is beneficial to become familiar with this band. [62]. The MMW frequency spectrum, depicted in Fig. 2-3, ranges from 30 to 300 GHz [63]. This type of electromagnetic wave has a wavelength in the millimeter range, specifically between 1 and 10 mm, which is why it is called a millimeter wave [62]. Some studies named slightly lower than 30 GHz as a MMW band such as 24 GHz [64] and 28 GHz [65]. The MMW is located in the Ka, V, W and G radar-frequency bands according to IEEE standard [66].

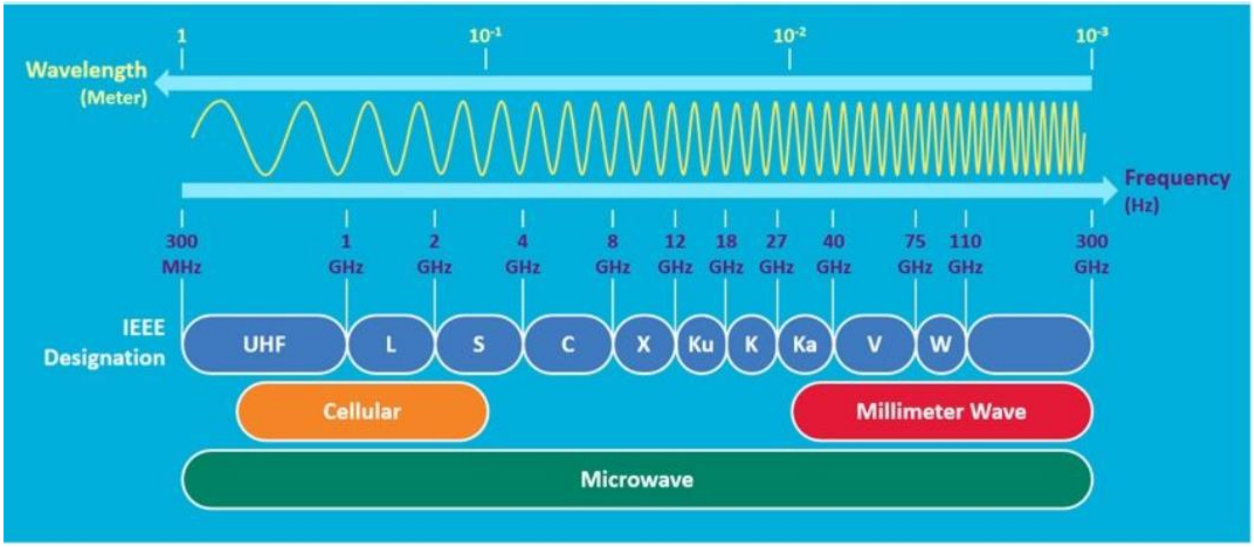

Figure 2-3 MMW in microwave spectrum bands [67]

This significant bandwidth can support interesting services such as High-Definition Television (HDTV), High-Definition Multimedia Interface (HDMI), High-Definition (HD) and Full High-Definition (FHD) streams [68]. MMW high-data-rate Wireless Personal Area Network (WPAN) is not only proposed for having direct communication between notebooks and related devices but also to replace cables via a wireless connection. The IEEE 802.15.3c industrial standard has been introduced to the MMW WPAN [69].

MMW has lots of applications in different areas from medical for cancer treatments [70] to police radar [71]. In security screening and microwave imaging, the MMW scanner has higher accuracy compared to the lower frequency bands. It can pass through clothes and thus, is used in airports to detect weapons and other dangerous objects [72].

The market demand for 5G to support around 100 to 1000 × higher system capacity than 4G, requires increasing the current operating frequency up to the MMW band in other word, using the 5G FR2 frequency band [73], around Shannon limit in point-to-point communications [74]. The MMW is set as an operation band for 6G communications too. However, even if there is no restricted separation between 5G and 6G communications bands, frequencies above 94 GHz are usually considered for 6G (F band).

Up to 7 GHz unlicensed bandwidth with the central frequency of 60 GHz is allocated for industrial, scientific and medical (ISM) band [75]. It is one of the largest unlicensed bandwidths in history. Meanwhile compared to the unlicensed bands in under 20 GHz such as UWB, it has less power limit restrictions and existing users. The 60 GHz high data transfer rates (e.g., 20 Gbit/s, IEEE 802.11ay) is attractive for gigabit wireless applications [76]. Wireless Gigabit Alliance (WiGig) gets benefit from this wide bandwidth to present wireless access with multi Gbit/s speed, as a new generation of WiFi for indoor communications [77].

Considering the reverse relation between operation frequency (f) and wavelength (λ), increasing frequency leads to shrinking wavelength to a smaller size [78]. This paves the way for compact and lightweight wireless devices at higher frequencies. On the other side, such compactness and small size make fabrication and design processes more complex and expensive [62].

Let f_H, f_L, and f_c be, respectively, the highest, the lowest, and the center operating frequency of a given bandwidth (BW). The fraction BW can be defined (in %) as the absolute bandwidth ($\Delta f = f_H - f_L$) divided by the center frequency

$$BW = \frac{f_H - f_L}{((f_H + f_L)/2)} \times 100 \qquad (2\text{-}1)$$

Referring to this equation, one percent of the bandwidth in the MMW band has a much wider frequency band than the frequency band under 20 GHz. Therefore, the interference is lower. Note also, that despite interesting advantages at MMW frequency range, high attenuation is a challenging part [79], Fig. 2-4. Lots of factors that do not have a significant impact below 20 GHz show high attenuations and losses at MMW such as rain and fog [73].

Considering the Friis equation, the path loss goes up with the square of the carrier frequency. Furthermore, the average atmospheric absorption generally increases by increasing the operation frequency [80], Fig. 2-4. This trend is further accelerated by other factors such as the resonance of oxygen molecules at 60 GHz [81]. The presence of oxygen molecules in water makes the water highly absorbent to MMW signals. In rainy weather, the high humidity and small water droplets obstruct the wireless pathway, can disturb the MMW connection [82].

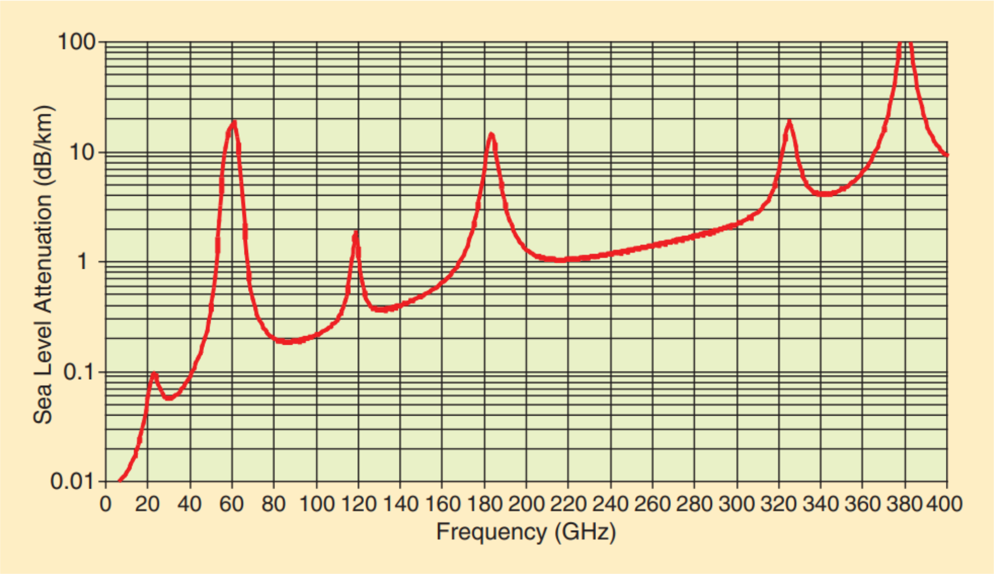

Figure 2-4 Average atmospheric absorption at millimeter-wave [83]

2.3 Parabolic Reflector

In this thesis, one of the two antennas will be used as reflector. Hence, it is desirable to introduce the parabolic reflector antenna, which employs a reflective surface to focus the signal. A reflector antenna is a type of antenna that is utilized in telecommunications and radio communication to focus or direct radio waves in a specific direction by using a reflective surface [78].

The fundamental principle of a reflector antenna involves the use of a curved reflective surface to redirect radio waves in a specific direction, akin to the way a concave mirror focuses light. The reflective surface is usually constructed of metal and can be shaped in different ways to achieve different directional properties, such as a parabolic shape, which is frequently employed in satellite dishes [84].

One of the most useful reflectors is the parabolic reflector antenna, a type of reflector antenna that utilizes a reflective surface with a parabolic shape to direct and concentrate electromagnetic waves. The parabolic shape of the reflector causes the incoming waves to reflect off the surface and converge at a single point, called the focal point. This produces an extremely directional beam of energy that can be employed for long-range communication or other purposes.

The primary element of a parabolic reflector antenna is the dish, which is a concave reflective surface made of conductive materials such as metal. The dish is designed with a parabolic shape, which is achieved by rotating a parabolic curve around its axis. The focal point of the parabolic reflector is positioned at the center of the dish [78]. Fig. 2-5 shows the parabolic antenna sketch in the two transmitting and receiving modes [85].

From Fig. 2-6 [85], the parabolic surface equation is made from the required condition of having a constant distance for the OP + PQ path. Therefore, in polar coordinates, we have [85]:

$$r = \frac{2f}{1+cos\theta} \qquad (2\text{-}2)$$

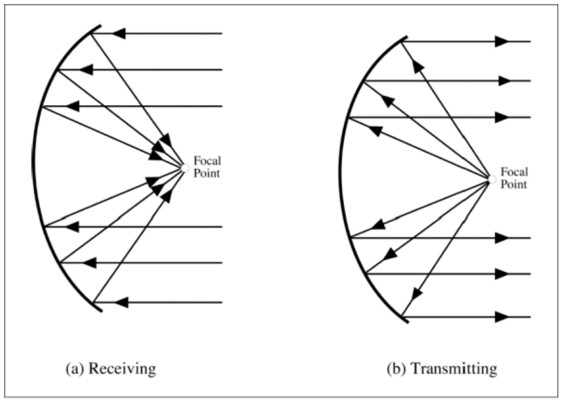

(a) Receiving (b) Transmitting

Figure 2-5 Focusing effect of a parabolic reflector in receiving and transmitting conditions [85]

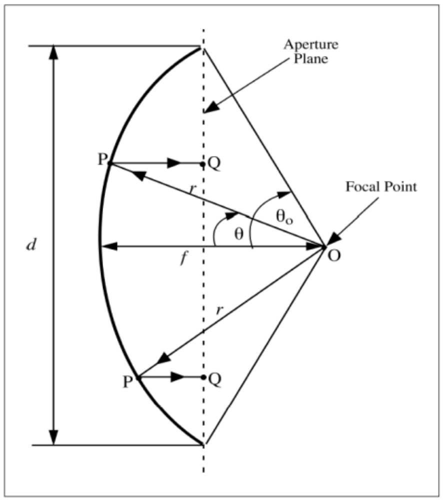

Figure 2-6 Geometric of a parabolic reflector with parameters [85]

For the subtended angle θ0, measured from the centerline to the edge of the parabolic reflector, one can observe that [85]:

$$\theta_0 = tan^{-1}\left[\left|\frac{f/_d}{2\left(\left(f/_d\right)^2-\frac{1}{16}\right)}\right|\right] \qquad (2\text{-}3)$$

In a cartesian coordinate system, the generic parabolic equation is given by:

$$y = ax^2 + bx + c \tag{2-4}$$

Here, the second derivative of y (y''), represents the curviness of the shape:

$$y' = 2ax + b \tag{2-5}$$

$$y'' = 2a \tag{2-6}$$

Therefore, the focal point, defined as the parabolic feed point, is [86]:

$$\text{Focal point} = \frac{1}{4a} \tag{2-7}$$

Note that the second derivative that shows graph curviness only depends on the “a” parameter: it is the only parameter that changes the structure curvature, as well as the focal point distance from the reflector, in reverse relation. Fig. 2-7 illustrates this parameter effect on the physical shape of the reflector: as approaching zero, the reflector shape reaches a flat structure, and the focal point goes to infinity.

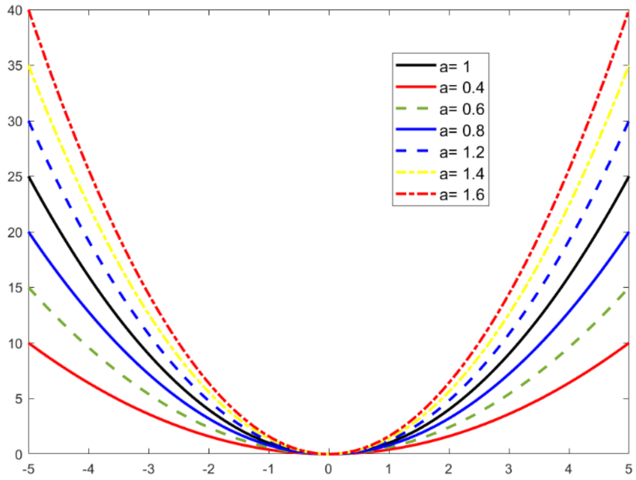

Figure 2-7 Effect of “a” parameter in (2-4) on the parabolic curviness

Using a flexible substrate for the L_{band} antenna (to build a parabolic reflector) will make the design of the antenna more complex [87]. It also adds a constraint [88] since bending a flexible antenna can significantly affect the key antenna parameters like bandwidth [89], gain, and radiation pattern [90]. On the other side, one can get benefit from a parabolic reflector.

2.4 Patch Antennas

Patch antennas are a type of planar antennas that have gained widespread popularity in recent years due to their low profile, low cost, and ease of fabrication [78]. Patch antennas are composed of a flat metal patch that is usually mounted on a grounded dielectric substrate. The metal patch may take on a variety of shapes, such as rectangular [91], circular [92], or elliptical [93], and may be fed by a variety of methods, such as coaxial probes [94], microstrip lines [95], or aperture coupling [96]. Patch antennas are particularly well-suited for applications where low profile and low weight are important, such as in satellite communication systems, wireless communication devices, and RFID systems [97]. Additionally, their simplicity and ease of integration make them a popular choice for applications where large arrays of antennas are required, such as in radar systems and base station antennas [98].

2.4.1. Microstrip Antenna

Microstrip antennas belong to the family of patch antennas. These antennas can be designed to operate at various frequencies and polarizations, and their radiation pattern can be manipulated by altering the shape and size of the patch. A microstrip antenna consists of a thin, flat metal patch that is mounted on a ground plane, separated by a dielectric substrate. The metal patch serves as the radiating element of the antenna. The ground plane underneath the patch provides a conductive surface that reflects the radiated energy and helps to direct the radiation pattern [99]. The dielectric substrate separates the patch from the ground plane and supports the patch, allowing it to maintain its position and shape. The feed line of the antenna is typically connected to the patch through a small aperture or gap in the ground plane [78].

The various operating modes of a microstrip antenna are generated by exciting diverse electromagnetic field patterns within its structure. These modes are identified based on the interplay between the electric and magnetic fields, as well as the antenna geometry’s boundary conditions.

The transverse magnetic (TM) mode is the most prevalent mode of operation for a microstrip antenna. It is triggered by applying voltage to the antenna’s radiating element, which generates an electric field perpendicular to the direction of propagation. Consequently, a magnetic field is induced around the radiating element, which interacts with the ground plane to produce the intended radiation pattern.

Applying voltage to the antenna can also induce the transverse electric (TE) mode but, in this case, the electric field is parallel to the direction of propagation. This generates a magnetic field perpendicular to the direction of propagation, which produces a radiation pattern with a null in the broadside direction [78].

In the realm of rectangular microstrip antennas, the TM_{010} mode is extensively employed, and it emerges when the antenna resonates at its fundamental frequency. In this mode, the electric field aligns mainly with the length of the antenna, while the magnetic field aligns mainly with the width. This yields a broadside radiation pattern, whereby the maximal radiation transpires perpendicular to the antenna’s surface.

The fundamental mode of a microstrip antenna carries substantial importance as it establishes numerous critical performance attributes such as resonant frequency, radiation pattern, and impedance matching. While the other higher-order modes of the antenna are feasible, they usually yield more intricate radiation patterns and can lead to decreased antenna performance. Therefore, designers generally refrain from exciting higher-order modes and instead concentrate on enhancing the antenna's fundamental mode of operation.

2.4.2. Rectangular Microstrip Antenna

In order for the antenna to operate at the fundamental mode, the rectangular patch antenna should have specific dimensions. Therefore, the antenna size should be calculated (Fig. 2-8)

For the radiation patch width W [78]:

$$W = \frac{c}{2f_0}\sqrt{\frac{2}{\varepsilon_r+1}} \qquad (2\text{-}9)$$

where f_0 represents the frequency and ε_r the relative permittivity. The effective dielectric constant, ε_{eff}, for microstrip section with W_l width and thickness of h, can be expressed as [78]:

$$\varepsilon_{eff} = \begin{cases} \frac{\varepsilon_r+1}{2} + \frac{\varepsilon_r-1}{2}\left(1 + 12\frac{h}{W_l}\right)^{-\frac{1}{2}}, & for\ \frac{W_l}{h} > 1 \\ \frac{\varepsilon_r+1}{2} + \frac{\varepsilon_r-1}{2}\left((1 + 12\frac{h}{W_l})^{-1/2} + 0.04(1 - \frac{W_l}{h})^2\right), & for\ \frac{W_l}{h} \le 1 \end{cases} \qquad (2\text{-}10)$$

Because it refers to the radiation path, the ${}^{W}\!/_{h} > 1$ condition is met. The physical length of the antenna, L, is determined by [78]:

$$L = \frac{c}{2f_0\sqrt{\varepsilon_{eff}}} - 2 \times \frac{0.412h(\varepsilon_{eff}+0.3)({}^{W}\!/_{h}+0.264)}{(\varepsilon_{eff}-0.258)({}^{W}\!/_{h}+0.8)} \qquad (2\text{-}11)$$

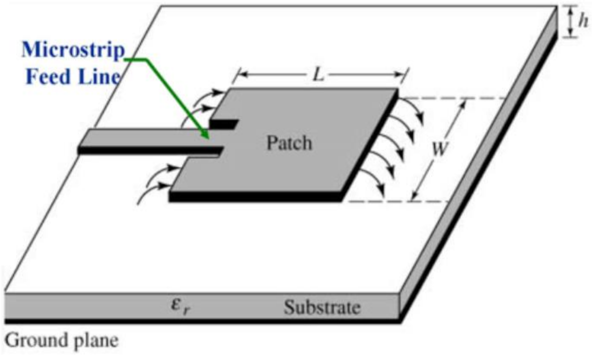

Figure 2-8 Sketch of a single layer rectangular microstrip antenna [67]

2.4.3. Monopole Microstrip Antenna (Half-Ground)

A monopole half-ground microstrip antenna has a partial ground plane beneath the patch. The ground plane is smaller than the patch, leaving one side of the antenna open. The unbalanced configuration of the antenna allows it to radiate energy, resulting in better radiation patterns and efficiency than a full ground microstrip antenna. The half-ground microstrip antenna also has a lower profile and can be more compact, making it suitable for use in smaller devices [100]. A sketch of a monopole patch antenna with half-ground is presented in Fig. 2-9.

On the other hand, a balanced configuration in a full ground antenna provides a symmetric radiation pattern but may suffer from reduced efficiency due to the ground plane's presence.

In terms of bandwidth, a half-ground microstrip antenna can have a wider range compared to a full ground microstrip antenna. This is because the partial ground plane in the half-ground microstrip antenna can introduce additional resonances, thereby increasing the antenna's bandwidth [99].

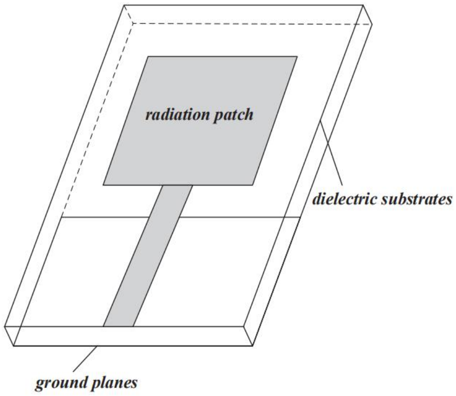

Figure 2-9 Structure chart of a monopole patch antenna (half-ground) [101]

Because of their significantly wider bandwidth, monopole antennas have been used in wideband wireless applications such as UWB [102], GSM [103], cognitive radio [104], and MMW [105].

2.5 Dual-band Antennas

The proposed novel design in this study aims to serve as a model for designing a dual-band antenna. Before proceeding to the actual design phase, conducting a study on dual-band antennas is highly beneficial. The use of dual-band antennas has become increasingly common in telecommunications applications, such as cellular and wireless networks [106]. By enabling simultaneous transmission and reception on two distinct frequency bands, dual-band antennas can help alleviate bandwidth congestion and improve network capacity. Additionally, they can mitigate interference from other wireless devices and enhance signal quality, resulting in better overall network performance.

2.5.1. State-of-the-Art

There are several ways of designing a dual-band antenna. One of the most popular methods is using a hybrid structure. The hybrid structures refer to the utilization of two or more types of patch antennas in a single design to achieve dual-band performance. In practice, it is constructed with two distinct radiating elements that are capable of resonating at different frequencies [107]. The radiating elements can be designed with various shapes and configurations, such as dipole [108], patch, or slot antenna types. For instance, a dual-band patch antenna may comprise two patches of different sizes, shapes, or orientation, each tailored to resonate at a specific frequency band [109].

Another approach to designing dual-band antennas, as discussed in [110], is to utilize a single radiating element that can operate in multiple modes. This involves designing the shape and structure of the radiating element in such a way that it can resonate at multiple frequencies and support various electromagnetic modes. The resonant frequency of an antenna is dependent on its physical dimensions, such as length, width, and thickness. By carefully selecting these dimensions, the radiation patch can resonate at multiple frequencies.

One of the most important applications of the dual-band antenna studied in this thesis is 5G wireless communication. One practical example of this application is the use of 5G technology in modern smartphones, such as the iPhone 13. In fact, referring to the Apple website (Table 2-1 [111]), in order to have a dual-band wireless host to cover the LTE and 5G frequency bands in iPhone 13, A central frequency radio of around 12 is required. The ratio was calculated by estimating the lower band between 0.6 – 4.7 GHz and the higher band in 26 – 39 GHz. This is a practical example to show the importance of having a dual-band wireless system with a large central FR.

Table 2-1 iPhone 13 5G and LTE frequency bands [111]. Here DD and TD stand respectively for Frequency Division Duplexing and Time Division Duplexing, AWS for advanced wireless services APT for Asia-Pacific Telecommunity, and PS for Public Safety.

5G Bands	**Frequency**	**5G Bands**	**Frequency**	**LTE Bands**	**Frequency**
n1	2100 MHz	n79	TD 4700	20	800 DD
n2	1900 MHz	n258	26 GHz	21	1500 MHz
n3	1800 MHz	n260	39 GHz	25	1900 MHz
n5	850 MHz	n261	28 GHz	26	800 MHz
n7	2600 MHz			28	700 APT
n8	900 MHz	**LTE Bands**	**Frequency**	29	700 MHz
n12	700 MHz	1	2100 MHz	30	2300 MHz
n20	800 DD	2	1900 MHz	32	1500 L-band
n25	1900 MHz	3	1800 MHz	34	TD 2000
n28	700 APT	4	AWS	38	TD 2600
n29	700d MHz	5	850 MHz	39	TD 1900
n30	2300 MHz	7	2600 MHz	40	TD 2300
n38	TD 2600	8	900 MHz	41	TD 2500
n40	TD 2300	11	1500 MHz	42	TD 3500
n41	TD 2500	12	700 MHz	46	TD Unlicensed
n48	TD 3600	13	700 MHz	48	TD 3600
n66	AWS-3	14	700 PS	66	AWS-3
n71	600 MHz	17	700 MHz	71	600 MHz
n77	TD 3700	18	800 MHz		
n78	TD 3500	19	800 MHz		

Due to the fascinating applications of dual-band antennas, they have attracted a lot of recent research attention. In [112], the antenna was optimized for consistent radiation pattern and efficiency at GSM, Long Range (LoRa), and Bluetooth Low Energy (BLE) bands. The design was based on a modified split ring that provides two radiating modes with a FR of 2.7.

In [27], a dual-band co-aperture planar array antenna design is presented. It reuses radiating elements operating at a higher frequency band for the lower frequency band using segmented patches. The design utilizes 4×4 H-shaped patches, used as 4×4 for the upper band and 2×2 for the lower band as illustrated in Fig. 2-10. The antenna has a working bandwidth of 8.8% from 5.4 to 5.9 GHz and another bandwidth of 7.3% from 13.2 to 14.2 GHz.

In [24], by metasurface-based decoupling method, two rectangular dual-band antennas operating close to each other (with ~1.4 FR) are described. In [28], a compact dual-band antenna system for 5G smartphones with 8 loop antenna elements operating at 3.5 GHz and 5 GHz bands is shown.

Each antenna has a small size of 6.9 × 6.6 mm^2 and consists of two folded stubs embedded on the phone frame. The antennas were excited by coupling with an inverted L-shape microstrip probe.

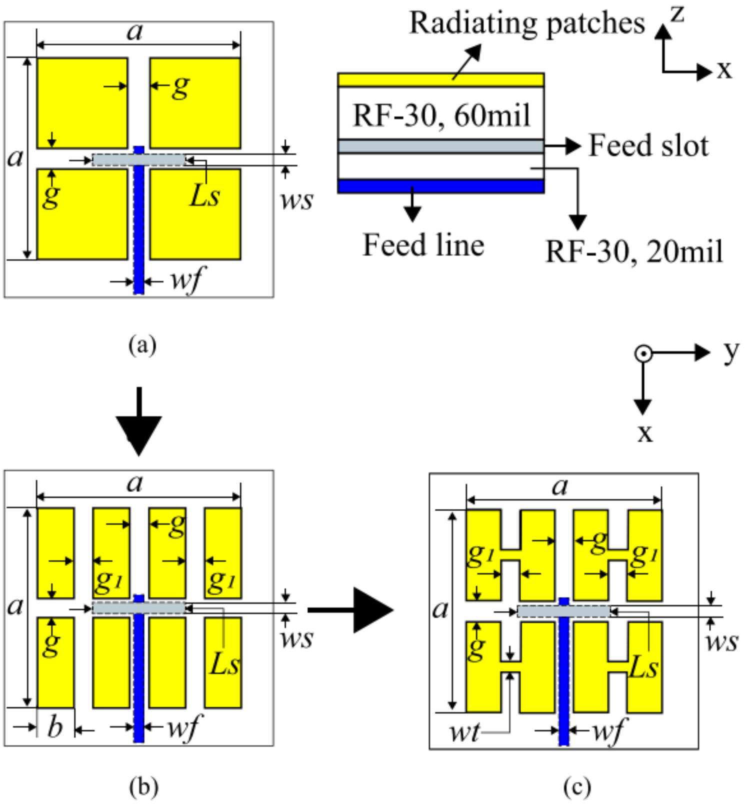

Figure 2-10 Designing steps of the co-aperture planar array antenna, (a) antenna made out of four square patches (b), the antenna is improved to eight rectangular patches, and (c) antenna design features four “H”-shaped patches.

In [113], the design and analysis of a dual-band and broadband slow-wave substrate integrated waveguide (SW-SIW) structure antenna is presented. The proposed antenna geometry consists of a SIW cavity structure and fractional slots, including one ring slot and three rectangular slots etched on the radiation patch. The simulated results showed that the antenna has a -10 dB impedance bandwidth of (12.04 GHz-13.88 GHz) and (14.15 GHz-14.58 GHz) with FR = 1.1.

2.6 Dual-band Antenna with Large Frequency Ratio (FR)

A dual-band antenna with a large FR is a specialized antenna that can operate over two frequency bands with a significant difference in frequency. These antennas are commonly used in various telecommunications and wireless systems, where high FRs can provide increased flexibility and versatility in operation.

In practice, a dual-band antenna with a large FR is designed with two distinct resonant frequencies, one of which being typically much higher than the other [114]. This design allows the antenna to operate over a wide frequency range while maintaining a compact form factor. The large FR between the two resonant frequencies enables the antenna to function over a broader frequency range, providing increased spectral efficiency and enhanced system performance. For increasing the dual-band antenna gain, one of the practical methods used is the array structure. There are two main design approaches for dual-band array antennas [115]: assigning a single frequency array set for each band or using dual frequency elements.

2.6.1. Dual-band Antenna with Large FR State-of-the-Art

[116] used a large size printed dipole for a lower band. The dipole bandwidth was enhanced by parasitic elements. Two pairs of small folded dipoles radiate in upper band. To shrink the structure’s total size, the smaller dipoles are nested inside the lower band, as shown in Fig. 2-11.

A single-layer gap waveguide (GW) with an embedded diplexer was designed to operate at k and ka bands [117]. The dual-band GW antenna is fed by a wideband corporate network. However, such dual-band shared-aperture GW antenna has a complicated structure and is challenging to fabricate.

A dual C/X band shared-aperture array antenna has been demonstrated in [118], Fig. 4-12. Four larger size C-band patches were set at the top of the substrate while 4 × 4 circular elements X-band patches were placed behind the substrate. These radiation patches are fed by a feeding network on the other side of the foam . The antenna lower band center frequency is at 5.3 GHz and the upper one at 8.2 GHz.

In [119], a nested dual-band array has 4 × 4 parallel-fed patches for WLAN 2.4 GHz and 8 × 8 hybrid-fed printed dipoles for WLAN 5.8 GHz applications. The side lobe level (SLL) was suppressed by a quarter-wavelength transformer and an adjustment in the antenna shape.

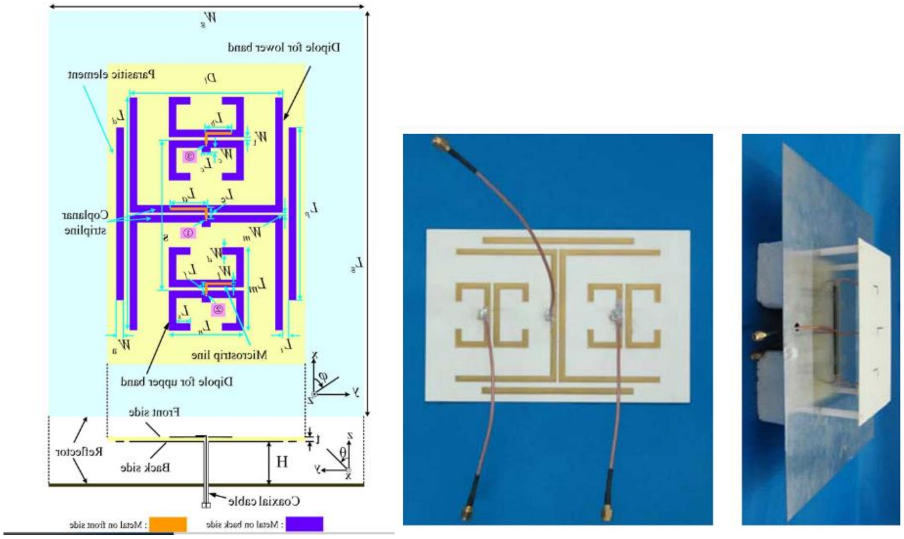

(a) (b) (c)

Figure 2-11 Dual-broadband planar antenna unit (a) geometry, (b) prototype front view, and (c) prototype perspective view [116]

The same method is observed in [17] to design a dual-band antenna. Two sets of 16 elements single frequency antennas are placed for the lower and upper bands. In Fig. 2-13, patch 1 works at X-band, and patch 2 at Ku-band.

Using an array antenna instead of a reflector one has some disadvantageous [120]. There are more parameters to control in the array. Also, the signal-to-noise ratio (SNR) drops in the array antenna due to loss of coherence in signal combination. Furthermore, the array antenna suffers from low bandwidth compared to the large bandwidth of a parabolic antenna.

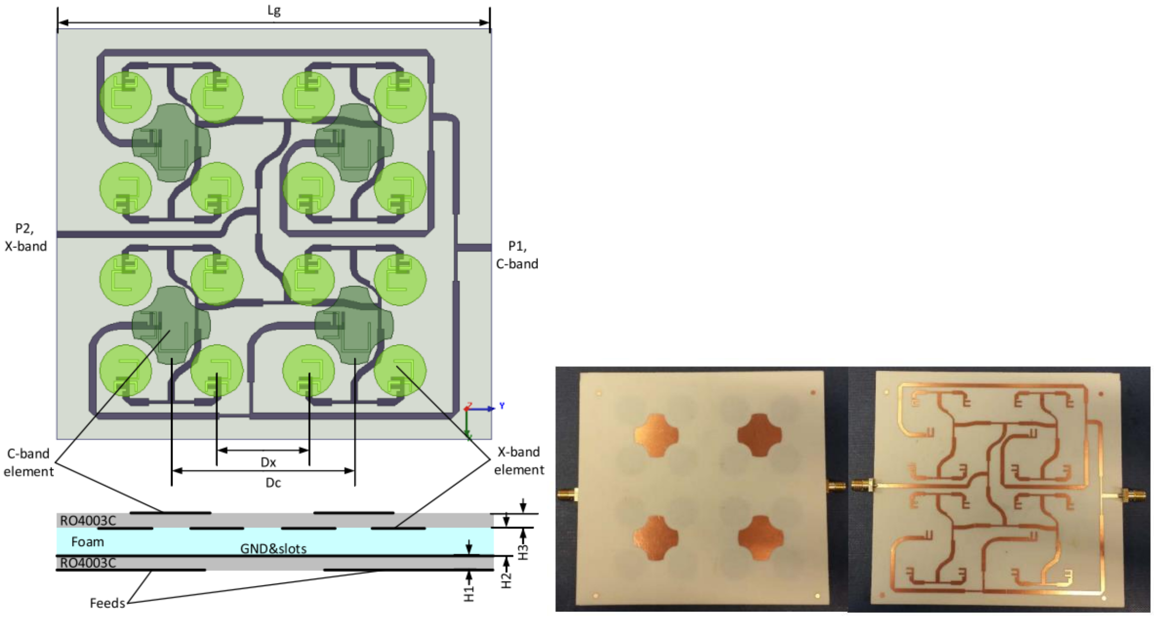

(a) (b)

Figure 2-12 Dual C/X band shared-aperture array antenna (a) configuration, and (b) prototype [118]

[16] discusses the trend towards the coexistence of different technologies in future wireless communication systems. However, since most existing dual-band antenna configurations have difficulty achieving a FR larger than 3, [16] proposes a novel topology that uses a signal routing approach to guide microwave/MMW signals to specific elements. The classical aperture coupling mechanism is utilized to block the MMW signal from feeding to the microwave antenna element and route it into the MMW antenna element. The substrate integrated waveguide (SIW) based MMW antenna element has a high-pass nature to reject the microwave signal, allowing for separate design of antenna elements for microwave and MMW bands with high flexibility. A dual-band antenna was implemented to support 5.8 and 30 GHz simultaneously thus, to achieve a FR of 5.2.

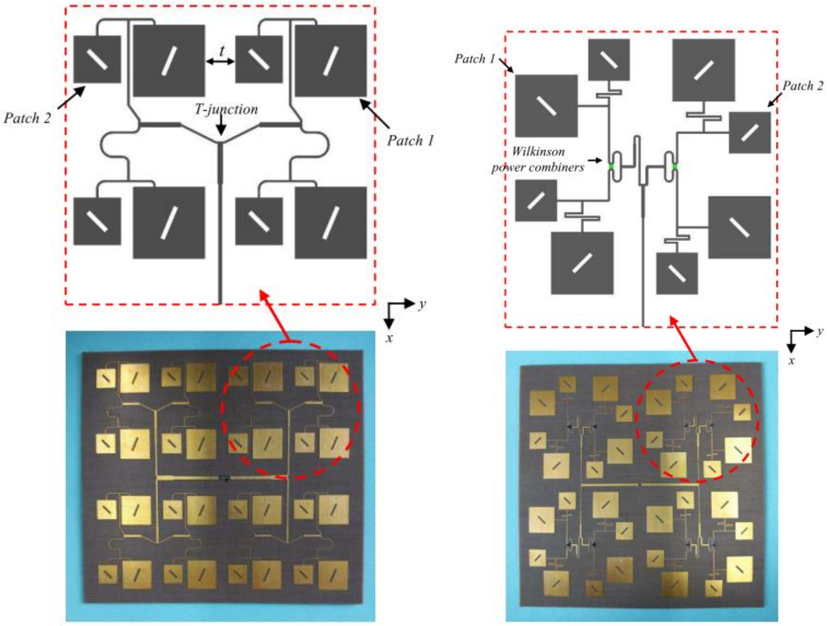

(a) (b)

Figure 2-13 Dual-band dual-CP shared-aperture array antenna (a) with conventional feed network and (b) with sequential rotation feed network [17]

In [121], a two-port dual-frequency substrate-integrated antenna with a large frequency difference is discussed. The antenna includes a slot antenna and a dielectric resonator antenna for low- and upper-frequency radiation, respectively. Slot-coupled sources for the two antennas were printed on a second substrate below the antenna. The antenna was designed for the 5.2-GHz WLAN band and 24-GHz ISM band.

A dual-band array antenna for 5G base station use was introduced in [122]. The array consists of a 4×4 MIMO array operating in the upper band (3.3-5.0 GHz) and a single antenna element working in the lower band (0.69-0.96 GHz).

The structure in [123] includes a two-elements array antenna for sub-6 GHz 4G bands and a MIMO antenna system for 5G mm-wave frequency band. The design has overall dimensions of $135\times77\times1.575$ mm^3, with the 4G antenna module at the top and the four 5G MIMO antennas on the longer edges. The 4G band covers 2.2-4.9 GHz, and the 5G antennas cover 26-28.8 GHz. The peak gain is 7.31 dB for the 4G antenna module and 9.21 dB for the 5G antennas. It has a FR of around 8.

An antenna solution was investigated in [18] for LTE and 5G MMW wireless communication services. The solution comprises a two-element LTE MIMO antenna and a four-element 5G MIMO configuration, Fig. 2-15. The proposed structure is capable of operating at 5.29–6.12 GHz and 26–29.5 GHz frequency bands.

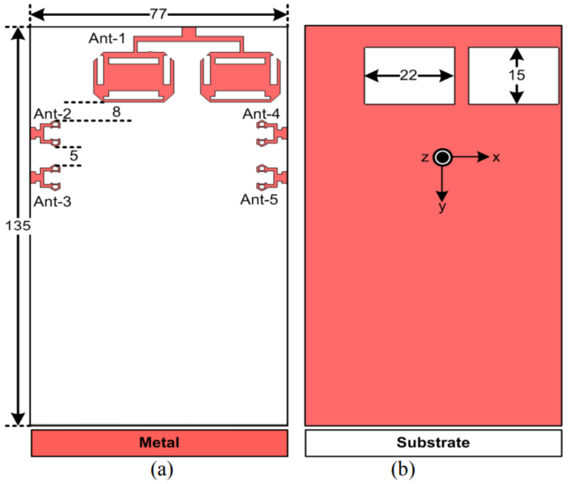

Figure 2-14 Dual-band 5G/4G antenna sketch [123]

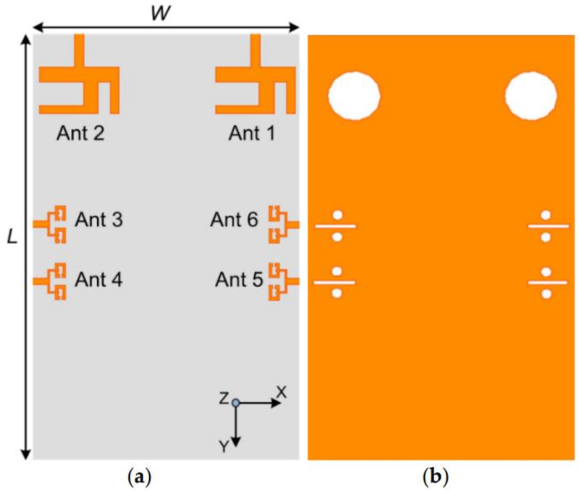

Figure 2-15 [18] The Sketch of the dual-band LTE and 5G MIMO antenna system (a) top view (b) bottom view

In [114], an integrated antenna system with defected ground structure (DGS) for 4G and 5G wireless applications on handheld devices is described. The prototype exhibits a peak gain of 5.41 dBi and 10.29 dBi for 4G and 5G, respectively while the FR reached 7.

[124] reported on a new dual-mode composite microstrip line (DMC-MSL) for designing dual-band antennas and devices with a large FR. The DMC-MSL structure combines the advantages of the microstrip line and the SIW, and by adjusting the permittivity of the dielectric laminate, the FR of the two operating modes can be varied. a novel dual-band leaky-wave antenna based on the DMC-MSL structure having a 5.4 FR.

2.6.2. Discussion

As discussed earlier, achieving a large FR can be challenging, particularly when aiming for a value greater than 3. Some researchers have attempted to design antennas with an FR higher than 3 to make them suitable for microwave/MMW and 5G applications. The highest FR reported in the literature reviewed in the above section was approximately 8. The hybrid model, which uses separate patches for each band, yielded the best results in terms of achieving a large FR.

2.7 Conclusion

In this chapter, the 5G technology was introduced, including its advantages and limitations. We went through two classifications of 5G: FR1 and FR2. Next, due to the parabolic reflector structure of our antenna, the parabolic antenna was introduced and some practical formulas presented.

Next, the patch antenna was introduced, followed by the dual band antenna. A literature review over previously designed dual-band antennas was presented while focusing on those with large FR. This will help establishing the theory behind designing our proposed dual band antenna.

Chapter 3 – Methodology and Theory

This chapter introduces the methodology used to design the final dual-band antenna structure. First, the fundamentals of an infinitesimal dipole antenna and planar reflector are introduced to study the effect of a planar reflector on the dipole gain and radiation pattern. Next, the fundamental of a parabolic reflector is introduced and compared with the planar one to choose the efficient shape of the reflector; in our structure, the reflector is the lower band antenna. The theory of radar cross section areas is also presented to help understanding the interaction between the lower/upper band antennas and the power received in each antenna from the other one.

These fundamental sections will set the stage for the implementation of the proposed dual antenna system. To do so, four models are introduced sequentially to help demonstrating this novel concept while continuously improving its performance. The first model (Model I) is inspired by the dipole planar reflector antenna and the new idea of replacing the reflector with a microstrip antenna of same size. Both antennas are very popular, but they have never been used in such structure. However, despite some improvement, the planar reflector in Model I only reflects the radiated wave on one side of the antenna. Therefore, Model II is introduced to collimate the reflected wave, leading to a theoretical gain improvement of about 15 dBi, compared to Model I. Now, because of the omnidirectional radiation pattern of the dipole, this type of antenna is not appropriate to use as feed. Thus, the dipole feed is replaced by a microstrip antenna (Model III). Finally, in Model IV, the full-ground microstrip antennas are replaced by a similar shape antenna having a wider bandwidth (half-ground antenna). With that, Model IV is demonstrated to have a higher gain of parabolic antenna and wider bandwidth than Model III.

3.1 Infinitesimal Dipole Antenna

Wire antennas are the simplest configurations of antennas. Their three popular shapes are shown in Fig. 3-1. The dipole one is made out of two straight wires; applying a time-varying current to each rod leads to the radiation of these antennas.

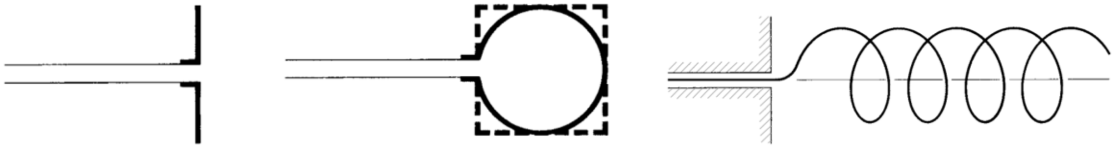

(a) Dipole (b) Circular/Square loop (c) Helix

Figure 3-1 Most common wire antenna configuration [78]

An infinitesimal antenna is a dipole antenna, with a very short length l compared to the wavelength, and made out of a thin wire of diameter a, i.e., $l \ll \lambda$ and $a \ll \lambda$. An infinitesimal antenna located symmetrically at the center of coordination is shown in Fig. 3-2 (a).

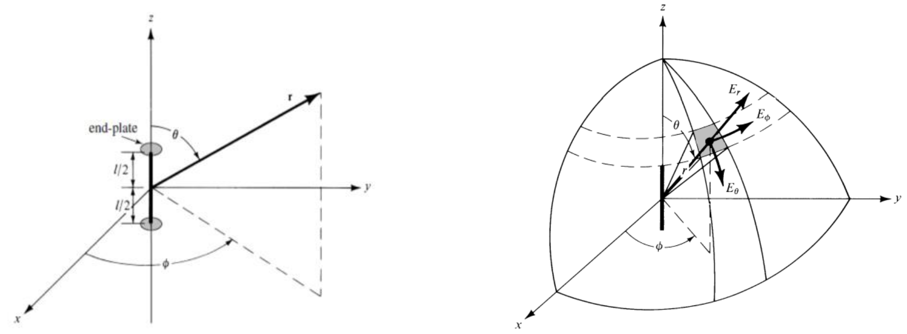

(a) (b)

Figure 3-2 infinitesimal dipole (a) dipole orientation (b) electric field orientation [78]

Such infinitesimal antennas are very popular in theory because they can be utilized as a building block of more complex structures [78]. Because the antenna length is very small compared to the operational wavelength, the electric current (I) is constant and exists solely in the antenna orientation, z-direction in Fig. 3-2 (a). For spatial variation of current, we can set [78]:

$$I(z') = \widehat{a_z} I_0 \qquad (3\text{-}1)$$

where I_0 is a constant electric current and $\widehat{a_z}$ the unit vector in the z-direction. The antenna electrical component on a spherical surface is represented in Fig. 3-2 (b). In region where $kr \gg 1$, with $k = {}^{2\pi}/_{\lambda}$ and r the distance, the electric (E) and magnetic (H) fields of the small dipole in far-field area can be approximated as [78]:

$$E_\theta = j\eta \frac{kI_0 l e^{-jkr}}{4\pi r} sin\theta \qquad (3\text{-}2)$$

$$E_r = E_\theta = H_r = H_\theta = 0 \qquad (3\text{-}3)$$

$$H_\phi = j \frac{kI_0 l e^{-jkr}}{4\pi r} sin\theta \qquad (3\text{-}4)$$

Here the antenna radiation intensity (U) is equal to [78]:

$$U = \frac{r^2}{2\eta} |E_\theta(r,\theta,\phi)|^2 = \frac{\eta}{2} (\frac{kI_0 l}{4\pi})^2 sin^2\theta \qquad (3\text{-}5)$$

the short dipole antenna gain (G_{dipole}) is calculated by:

$$G_{dipole}(\theta, \phi) = \frac{3}{2}\sin^2(\theta) \tag{3-6}$$

while the antenna normalized radiation pattern can be set as [125]:

$$p(\theta, \phi) = \sin^2(\theta) \tag{3-7}$$

3.2 Planar Reflector

The schematic view of a short dipole antenna with a planar conductive reflector is shown in Fig. 3-3 (a) ($\sigma_{conductivity} \gg \omega\epsilon$, where ϵ is the permittivity of the medium and $\omega = 2\pi f_{planar}$, with f_{planar} the operating frequency). Fig. 3-3 (b) shows the image model of it. The planar reflector makes an image of the dipole on the other side of y-axis. As a result, the dipole and its image create a two-element array antenna. The total radiation pattern and gain are defined by vector addition of the fields radiated by each element. The total field of the array is calculated by the field of a single element (here a dipole) multiply by a factor, called the array factor (AF). The array factor of two dipole antennas ($AF_{Two\ dips}$) is equal to [125]:

$$|AF_{Two\ dips}(\theta, \phi)| = \begin{cases} 4sin^2[ka\sin(\theta)\cos(\phi)] & for \quad -\pi/2 \le \phi \le \pi/2 \\ 0 \quad for & \pi/2 \le \phi \le 3\pi/2 \end{cases} \tag{3-8}$$

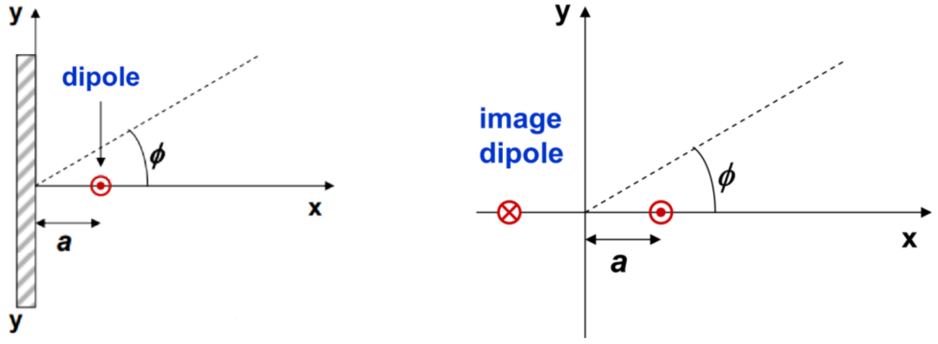

(a) (b)

Figure 3-3 Short dipole antenna with planar reflector (a) sketch, and (b) image model [125]

For the antenna maximum gain (at $\theta = \pi/2, \phi = 0$), $\sin(\theta) = \cos(\phi) = 1$ in equation (3-8), the $AF_{Two\ dips}$ has its maximum value when $sin^2[ka\sin(\theta)\cos(\phi)] = 1$. Thus, ka is:

$$ka = n\frac{\pi}{2} \qquad for\ n = 1, 3, 5, \ldots \tag{3-9}$$

Similarly, the antenna gain is [125]:

$$G_{planar}(\theta,\phi) = \frac{3}{2} sin^2(\theta) \left|AF_{Two\ dips}(\theta,\phi)\right|^2 \tag{3-10}$$

and the antenna radiation pattern is:

$$p_{planar}(\theta,\phi) = \frac{1}{4} sin^2(\theta) \left|AF_{Two\ dips}(\theta,\phi)\right|^2 \tag{3-11}$$

The plan reflector has increased the maximum dipole gain by a factor of 4 (equation (3-6) vs. (3-10)); Fig. 3-4 (a) shows the gain of the dipole with and without the planar reflector. Meanwhile, the reflector makes the dipole antenna radiation pattern more directive with a main beam at 0^o, calculated from equations (3-7) and (3-11), Fig. 3-4 (b).

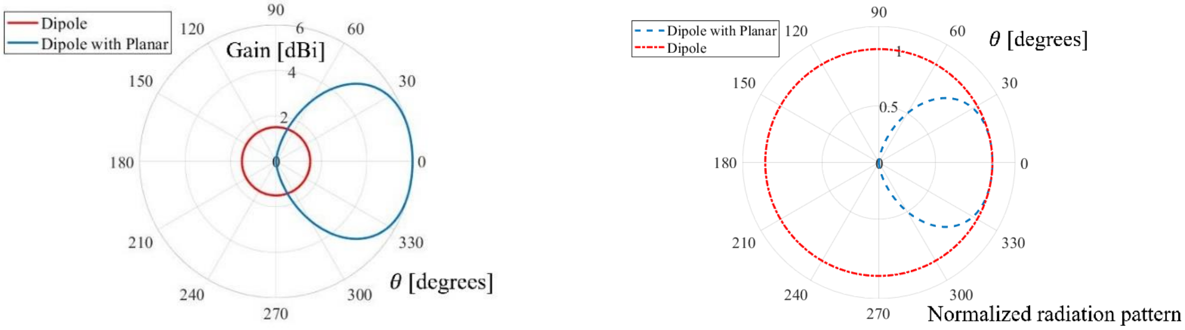

(a)

(b)

Figure 3-4 Dipole with/without planar reflector (a) Gain, and (b) Normalized radiation pattern

The maximum dipole antenna gain (equation (3-6)) is 1.5 when $\sin^2(\theta) = 1$, while the maximum planar reflector antenna gain (equation (3-10)) is equal to 6 [125]. Therefore, using a planar reflector increases the dipole antenna gain by a factor of 4 [125]. Let us name this first enhanced configuration (by replacing the planar reflector by a planar antenna) as Model I, Fig. 3-5.

Therefore, if we chose the lower-band antenna as a patch antenna with a solid full-ground plane equal to the total size of the antenna, and the upper band one is a dipole antenna, the lower-band antenna in Fig. 3-5 can increase the upper band gain by a factor of 4.

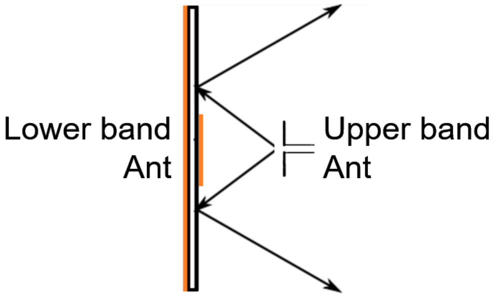

Figure 3-5 Antenna integrated reflector having planar lower-band antenna and dipole upper band one, Model I

3.3 Parabolic Reflector

The next step is to see how to further increase the performance of the system of the two antennas. A planar reflector reflects the radiated wave toward its plane, i.e., the x-direction in Fig. 3-3 (a). If the reflector surface is big enough, there is no radiation behind the reflector. But this type of reflector does not collimate the radiated wave. To achieve a higher gain, a parabolic reflector can be considered, because this well-known structure collimates the feed antenna radiations [126] thus, improving the upper band gain.

A shaped reflector such as parabolic or cylindrical increases the total gain more than a planar one; e.g., a corner reflector increases the maximum gain by a factor of 16 [125]. However, gain increase in parabolic reflector depends on the device's size. In our system, this size depends on the center frequency of the lower band. The parabolic antenna maximum gain $G_{parabolic}(\theta,\phi)$ occurs in its axis of symmetry of a parabola [127], the z-axis in Fig. 3-6. The parabolic antenna gain is then equal to [125]:

$$G_{parabolic} = \frac{4\pi A}{\lambda^2} e_A = (\frac{\pi D}{\lambda})^2 e_A \qquad \text{(3-12)}$$

where A is the area of the antenna aperture, D the reflector diameter and λ the wavelength.

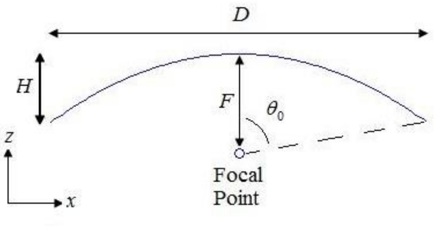

Figure 3-6 Parabolic antenna with focal point [128]

The quantity e_a is a dimensionless parameter, called aperture efficiency, which depends on variety of factors such as resistive or ohmic losses, surface deviations, spilled energy over the edge of the reflector surface, etc. This parameter is between 0 and 1 [129, 130]. The practical average value of e_a is in the range of 0.5-0.7 [130]. So, for the rest of the calculations, this parameter will be set to $e_a = 0.6$. Referring to equation (3-12), the parabolic antenna gain depends on the $D/_{\lambda}$ ratio.

Let us take a practical example to illustrate the dependence of the gain over D and λ. The wavelength λ in equation (3-12) refers to the upper band frequency. With a targeted frequency of 25 GHz, this value is equal to 0.012 m. As for D, it refers to the lower-band antenna size. From equations (2-9) and (2-11), for a frequency of 2.4 GHz, we have D = 0.07 m. This leads to a gain of 201 or 23 dBi. The substrate is considered as a PF-4, thickness of 1.6 mm, dielectric constant = 1.06, and loss tangent = 0.0001.

Therefore, if the planar antenna is shaped as a parabolic one (Fig. 3-6), the antenna gain at upper band is expected to significantly increase. Let us call this new configuration as Model II (Fig. 3-7), in which the lower-band planar antenna is now replaced by a parabolic-shaped antenna.

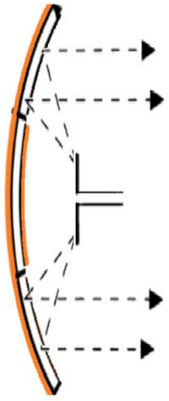

Figure 3-7 Antenna integrated reflector having parabolic lower-band antenna and dipole upper band one, Model II

3.4 Radar Cross Section (RCS)

Radar cross-section (RCS) is a good indicator to investigate the interferences and interactions between two antennas [5]. In our work, the RCS parameter will be used to evaluate the ability of the lower-band antenna as reflector.

In each band, when one of the antennas works, the other antenna acts as an obstacle. The RCS at the upper band indicates the amount of power density that the reflector reflects, i.e., the same concept in radar for detecting an object [131].

Electromagnetic (EM) waves, regardless of their polarization, are diffracted or scattered in all directions when incident an object in their pathway. The scattered waves are classified into two kinds: the first is when the wave has the same polarization as the receiving antenna. The second is when the wave and the receiving antenna have different polarization. These two polarizations are named respectively Principal Polarization (PP) and Orthogonal Polarization (OP). The intensity of the backscattered energy with the same polarization as the antenna is used to determine the Radar Cross Section (RCS). RCS is the measure of an object's ability to reflect the radiated wave toward the radar direction [132]. The higher the RCS, the more signal is reflected from the object. In our dual-band antenna system, the lower-band antenna is expected to reflect most of the radiated EM wave from the upper band one. Therefore, the higher the lower-band antenna RCS, the higher the reflected wave toward the upper band antenna; also, the more the reflected wave from a parabolic dish, the greater the parabolic antenna gain. So, the RCS is a helpful parameter for finding an adequate lower-band antenna structure in order to have high gain.

When the object is exposed to EM radiation, it acts like an antenna. Same as the antenna, it has near and far scattered fields. The near-field wave is spherical, and the far-field is mostly linear [131]. Assuming the target is located at a distance R from the radar antenna, Fig. 3-8, let us call the power density of the EM wave incident on an object as P_{Di}.

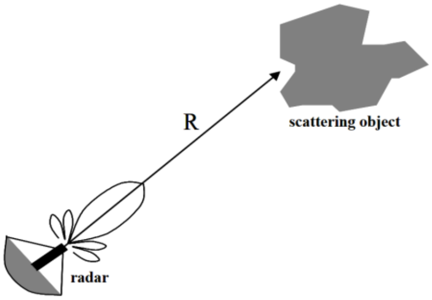

Figure 3-8 Object located at range R from radar [131]

For the received power [131]:

$$P_r = \sigma P_{Di} \qquad (3\text{-}13)$$

where σ is the object RCS and P_r the received power. Then, the power density of the scattered EM wave at the receiving radar, P_{Dr}, is

$$P_{Dr} = {}^{P_r}\!/_{(4\pi R^2)} \qquad (3\text{-}14)$$

The RCS is thus given as

$$\sigma = 4\pi R^2 (\frac{P_{Dr}}{P_{Di}}) \qquad (3\text{-}15)$$

A target with high RCS is very visible by a radar because it reflects most of the radiated signal from the source antenna [133]. Similarly, high RCS means high reflected signal in the direction of the source [134], So, higher the RCS when the source antenna is placed at the parabolic focal point, higher will be the total antenna gain [129].

3.4.1 Rectangular RCS

The RCS of an object depends on the object’s shape and the incident angle of the radiated wave to it. Let us consider a perfectly conductive rectangular plate in the x-y plane, Fig. 3-9. The plate has a total size of 2a × 2b with a very thin thickness.

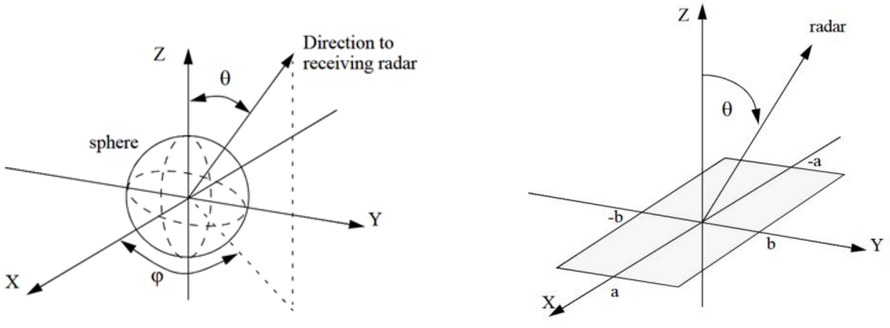

(a) (b)

Figure 3-9 (a) Receiving radar (b) Rectangular flat plate [131]

For an incident (θ, ϕ) EM wave, the RCS of the rectangular plate can be expressed as [131]:

$$\sigma = \frac{4\pi a^2 b^2}{\lambda^2}\left(\frac{\sin\left(ak\ sin\theta cos\phi\right)}{ak\ sin\theta\ cos\phi}\frac{\sin\left(bk\ sin\theta\ sin\phi\right)}{bk\ sin\theta\ sin\phi}\right)^2 (cos\theta)^2 \qquad (3\text{-}16)$$

$$k = {}^{2\pi}/_{\lambda}$$

If

$$h = \left(\frac{\sin\left(ak\ sin\theta cos\phi\right)}{ak\ sin\theta\ cos\phi}\frac{\sin\left(bk\ sin\theta\ sin\phi\right)}{bk\ sin\theta\ sin\phi}\right)(cos\theta) \qquad (3\text{-}17)$$

then,

$$\sigma = \frac{4\pi a^2 b^2 h^2}{\lambda^2} \qquad (3\text{-}18)$$

From this equation, the RCS of a rectangular shape increases with the object's surface and decreases by increasing the wavelength. In our design, at lower frequency band, the upper band antenna is considered as a scattering object. Further, when it operates at the upper band, the lower band one is the scattering object. So, at the lower band, lower the RCS, lower the signal reflected by the upper band antenna. Equivalently, less reflected wave from the upper band antenna, less radiation pattern variations. In this case, the lower-band antenna is considered as the radar and the upper band antenna is a rectangular object on its radiation path.

On the other hand, having a high RCS at the upper band frequency is suitable. A high RCS at this frequency represents more power density scattered from the reflector, i.e., the lower-band antenna thus, higher gain [135, 136]. As discussed in section 3.3, a parabolic reflector collimates the radiated EM wave from its focal point.

After improving the lower-band antenna structure, we could replace the upper band dipole antenna by a microstrip patch antenna. In fact, a microstrip antenna has a higher gain and more directive radiation pattern than an omnidirectional dipole antenna; thus, a better choice for the feed in parabolic structure [137, 138]. Also, microstrip antennas are well known for their small size, simple design, and ease to manufacture [139]. This would be our Model III (Fig. 3-10).

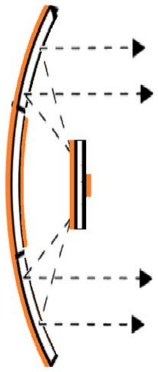

Figure 3-10 Antenna integrated reflector having parabolic lower-band antenna and patch upper band one, Model III

However, full-ground microstrip antennas have some well-known limitations such as low bandwidth, typically in the range of 1-2% [140] thus, not suitable for the targeted 5G applications. Therefore, in Model IV, Fig. 3-11, the microstrip antenna should be replaced by a half-ground monopole antenna, which has a wider bandwidth [141]. In fact, Model IV should exhibit desirable specifications for the dual-band 5G applications [142]. Thanks to the monopole structure, the antenna has the potential to be wideband in both frequency bands. The upper band antenna has a parabolic reflector. Therefore, it has a high gain and stable radiation pattern at the upper band.

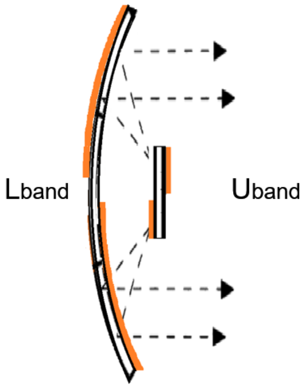

Figure 3-11 Antenna integrated reflector having monopole wideband upper/lower-band antennas, Model IV

Furthermore, the monopole antenna usually exhibits a low RCS because of its smaller surface area (represented by $a^2 b^2$ in equation (3-18)). However, a low RCS decreases the upper band gain. To address this issue, a monopole antenna with high RCS is therefore required, which will be discussed in chapter 4.

3.5 Conclusion

In this chapter, the design methodology behind the dual-band antenna design was investigated. It started from a first model (Model I) having a structure inspired by planar reflector antennas. The lower band antenna is a microstrip one having a same size of the planar reflector; a dipole feed being operating at upper band. The conductive ground of the microstrip antenna acts as the previous planar reflector for the dipole antenna and increases the gain by a factor of 4.

The planar reflector reflects wave at the same angle that it hits the surface. To collimate the reflected wave for higher gain, the planar reflector was bent in a parabolic shape, and the dipole was placed in the focal point. Therefore, the full ground can be seen as a parabolic reflector (Model II), leading to a higher gain.

Further, because a parabolic antenna needs a feed with a directive radiation pattern toward the reflector to give a high gain, the dipole antenna was replaced by a microstrip one, which has a higher gain compared to the dipole (Model III). However, replacing a thin dipole antenna by a microstrip one has some disadvantages. In fact, because instead of thin wire, there will be a rectangular antenna having a noticeable length and width near the antenna, the upper band antenna could reflect the radiated signal from the lower-band one. It thus required to investigate the power reflected from the upper band antenna in terms of RCS.

Our target application (5G) requires also high bandwidth. To satisfy this requirement, the full-ground microstrip antennas in upper and lower-bands should be replaced by a monopole half-ground antenna. In fact, the half-ground antenna has significantly lower RCS compared to the full-ground one.

The next chapter focuses on designing such monopole antenna with high RCS, with the objective to further improve the antenna gain and bandwidth. Also, the effect possible interactions between the two antennas will be also investigated.

Chapter 4 – Implementation of the Design Method

In the previous chapter, the design methodology behind the dual-band antenna design was investigated. Different configurations were considered, leading to the choice of Model IV, to be used for dual-band applications that require high frequency ratio (FR). The model could specify certain requirements for the 5G applications under consideration, such as a wide bandwidth and high gain.

In this chapter, the structure and performance of this last configuration will be discussed. To do so, and since it is a 3D configuration, the L_{band} half-ground antenna will be designed by selecting a suitable substrate and a bending position that allow having a parabolic reflector. In designing the antenna, all of the determined specifications in the previous chapter will be applied to the antenna. Such L_{band} antenna will be named "LB antenna-I". As such, various flexible substrates and conductive materials are being studied to identify the optimal candidates for the antenna. In fact, when a flat flexible antenna is bent, it can negatively impact its performance. Consequently, different bending types and radii will be investigated to determine a suitable configuration for the targeted application.

To better fit Model IV, the structure of antenna mentioned in the previous chapter will be improved by focusing on increasing its RCS and reflectivity. This improved version of the antenna will be called "LB antenna-II". Thus, the bend position of LB antenna-II will be determined based on the study of LB antenna-I. In fact, LB antenna-II will be designed to be bent using the same substrate that identified in the study. However, it is important to note that the substrate datasheet is only valid for a flat application, and any bending during fabrication may alter the material's parameters and affect its performance. Therefore, the impact of this on the antenna's performance will be studied for different substrate parameters.

Then, the LB antenna-II will be inserted in the dual-band structure introduced in the previous chapter (referred to as Model IV) to evaluate the reflector performance in the upper band. A reference horn antenna will be used as feed and reflectarray elements placed behind the antenna patch (used as ground). Several reflectarray shapes will be studied to select the suitable one. Finally, two proposed dual-band antenna integrated reflectors will be presented.

4.1 L_{band} Flexible Antenna Design

In the previous chapter, the study was focused on determining what type of antenna characteristics are suitable for building our model (Model IV).

Here, the lower band antenna will be designed to operate within the defined frequency range of 410 MHz to 7.125 GHz for our 5G FR1 application.

Before adopting it, we have to evaluate its performance vs. different parameters. Note that, due to limitations in the manufacturing and measuring facilities, the parabolic bent antenna will be approximated by a cylindrical one.

First, a suitable substrate and curvature radius should be determined to reach a wide bandwidth: this will be the focus of the prototype "LB antenna-I". Next, a second prototype called "LB antenna-II" will be designed while improving its RCS and reflectivity.

4.1.1. Half-Ground L_{band} Antenna (LB Antenna-I)

LB antenna-I is shown in Fig. 4-1. It has a half-ground structure and was designed on a flexible substrate. Two square resonator elements are placed close to the main microstrip feed line similar to [143]. Preliminary simulations helped determining the following physical parameter values: W_s = 8.7 cm, L_s = 13 cm. W_f = 3 mm, L_f = 51 mm, W_g = 73 mm, L_g = 44 mm, W_p = 78 mm, L_p = 77 mm, a = 20 mm, b = 10 mm, c = 16 mm, d = 23 mm, and e = 8 mm.

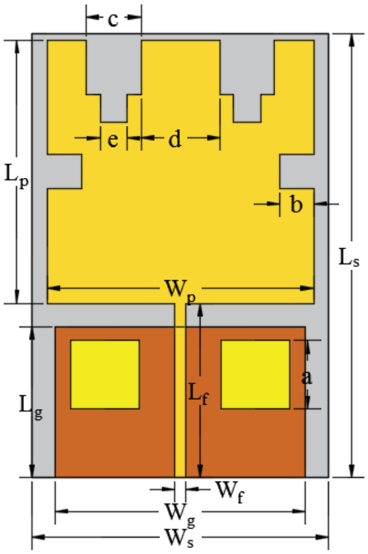

Figure 4-1 L_{band} half-ground antenna with square resonators, "LB antenna-I"

4.1.1.1. Selection of Substrate and Conductive Material

Organic flexible substrates and conductive materials have different effects on the performance of flexible antennas with respect to the operational frequency, antenna structure, and bendability [144, 145]. Before incorporating the antenna into our model as the lower band one, it is crucial to ensure that the antenna exhibits stable and reliable performance, and a suitable substrate has been selected for it.

Two substrates were considered (Table 4-1). As shown in Fig. 4-2, The low dielectric constant of substrate PF-4 led to a thick microstrip feed line having a 50 ohm impedance [78]. In fact, the width of the microstrip line, W_f, is close to the SMA connector width. Therefore, if the SMA pin is soldered, the ground of the connector will be electrically connected to the line too.

Table 4-1 L_{band} antenna substrates specifications

Substrate	Dielectric constant	Loss tangent	Thickness
PF-4	1.06	0.0001	1.6 mm
PET	3.2	0.08	1.5

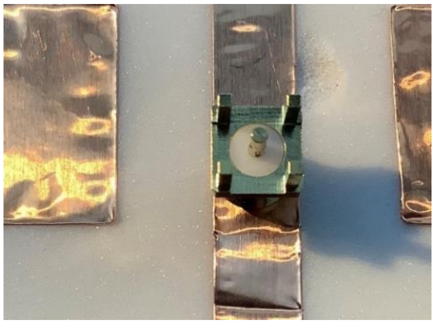

Figure 4-2 SMA connector and LB antenna-I feed line, diameter comparison

Therefore, a small gap was added between the SMA connector and the antenna substrate during the soldering process to overcome such an issue, as shown in Fig. 4-3. The antenna bandwidth is not degraded by this gap due to the fact that the substrate's dielectric constant is very similar to that of air. The gap was not added to the PET antenna because of its dielectric constant of 3.2.

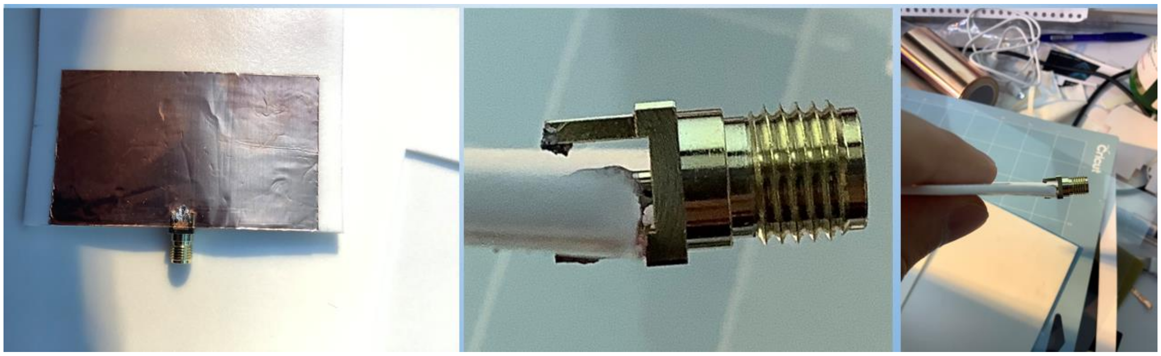

Figure 4-3 Soldered SMA connector to PF-4 LB antenna-I

However, it should be noted that if the PET substrate is preferred to the PF-4 in terms of feed line size and transparency, it is less flexible, an issue in curved structures (Fig. 4-4 and 4-5). So, a comparison of their respective performance as antenna substrate should be performed.

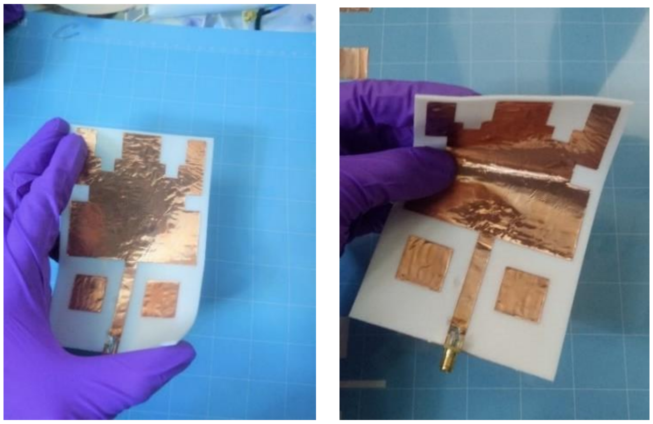

Figure 4-4 Fabricated PF-4 based LB antenna-I

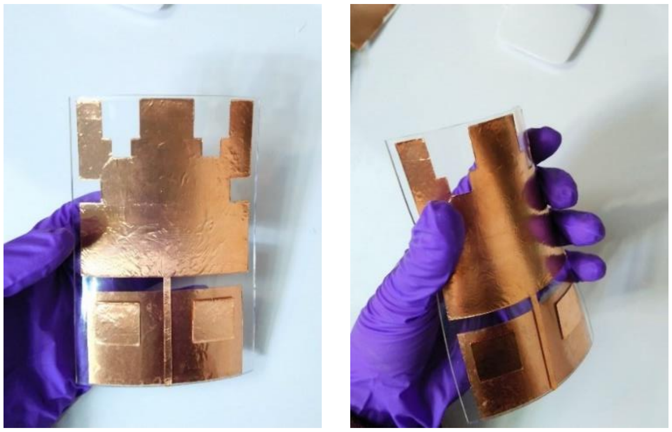

Figure 4-5 Fabricated LB antenna-I on PET substrate

The bandwidths of two fabricated LB antenna-I, one on a PF-4 substrate and one on a PET, was measured using a NanoVNA [146].

PF-4 LB antenna-I demonstrated a bandwidth ranging from 760 MHz to 1735 MHz, as shown in Fig. 4-6. Meanwhile, PET LB antenna-I covered a bandwidth of 760 MHz to 1654 MHz, for $S_{11} \leq -10$ dB (Fig. 4-7). Both antennas showed a wide bandwidth exceeding 70%. Next, it should be compared how apt they are to curvature.

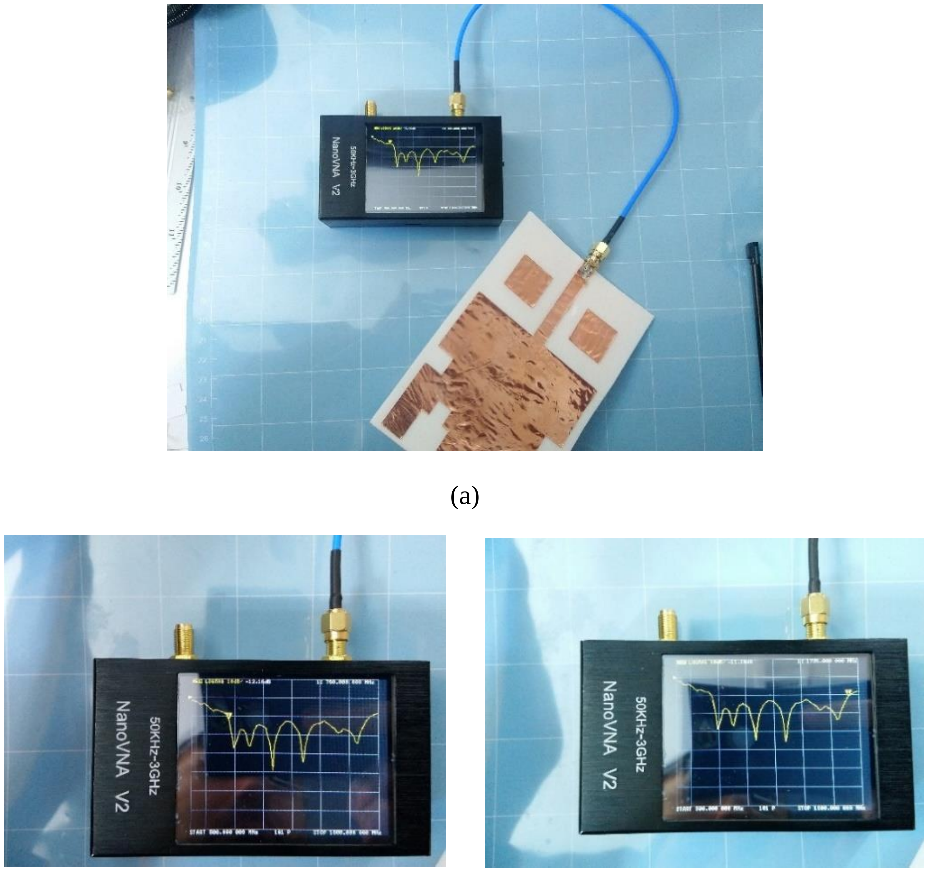

(a)

(b)

(c)

Figure 4-6 PF-4 LB antenna-I, bandwidth measurement, (a) overall view, (b) lowest frequency point, (c) higher point

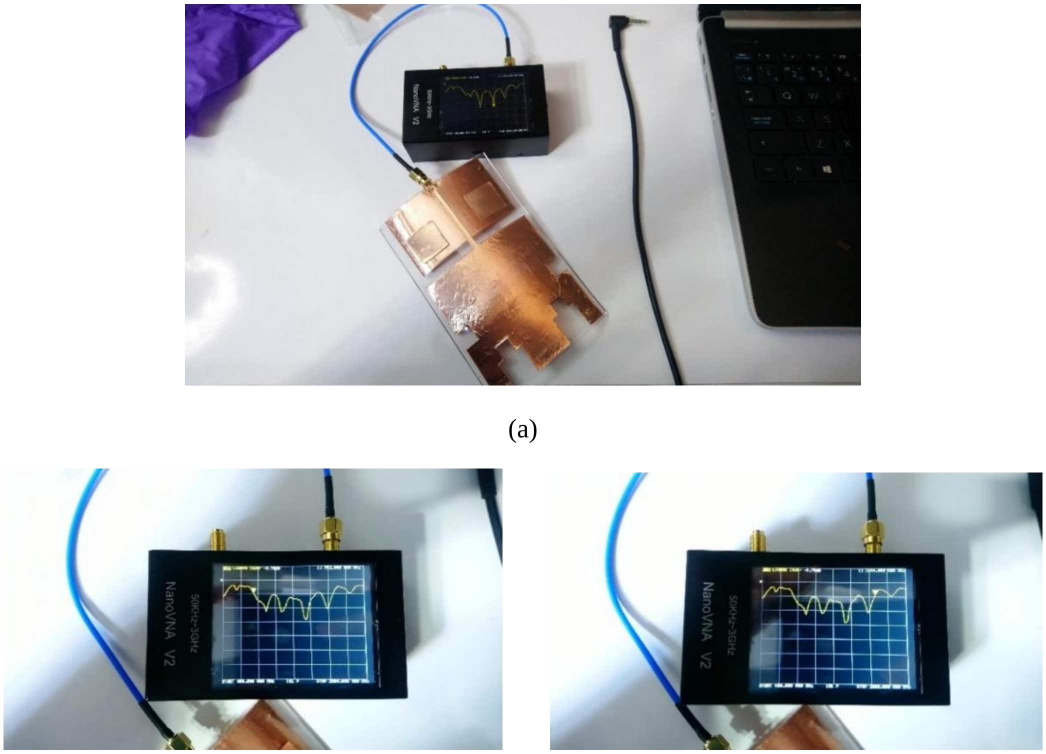

(a)

(b) (c)

Figure 4-7 PET LB antenna-I, bandwidth measurement, (a) overall view, (b) lowest frequency point, (c) highest point.

4.1.1.2. Curvature Effects

Because the parameters of flexible antennas are very sensitive to bending and folding [147, 148], the LB antenna-I performance was evaluated under different bending situations. Note that a positive bending is when the object, in our case the antenna, is bent concave upward. In contrast, a negative bending happens when the antenna concaves downward (or towards the negative direction) [149], Fig. 4-8. So, the two LB antenna-I antennas (PF-4 and PET) were studied when the whole antenna is bent (full-bent), as displayed in Fig. 4-8 (a) and (c), and when only the radiation patch is curved (semi-bent), Fig. 4-8 (b) and (d).

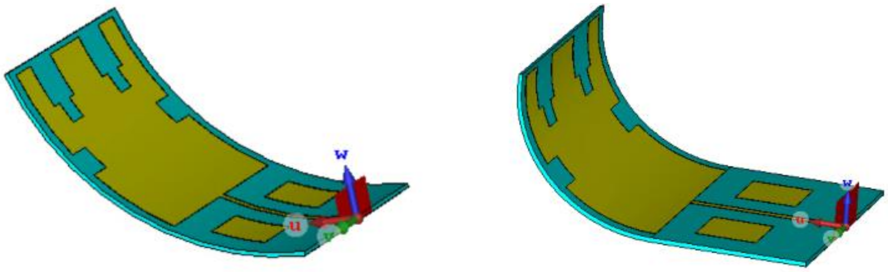

(a) (b)

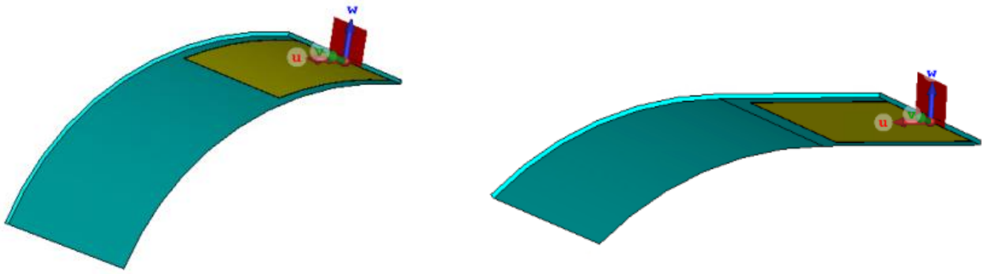

(c) (d)

Figure 4-8 LB antenna-I view at four different positions, (a) positive full bending, (b) radiation patch positive bending, semi-bent (c) negative full bending, and (d) radiation patch negative bending, semi-bent.

For positive full bent with a bend radius from 200 mm downward to 80 mm over an imaginary cylinder, as in Fig. 4-8 (a), the S_{11} variation is shown in Fig. 4-9. The PET antenna keeps the integrated bandwidth for the harshest bending.

The PF-4 antenna is more sensitive to positive full bending, and for around the central frequency of 1250 MHz, the antenna S_{11} parameter goes slightly higher than -10 dB. However, the lower and upper frequencies are not really affected by the bending, Fig. 4-9 (b).

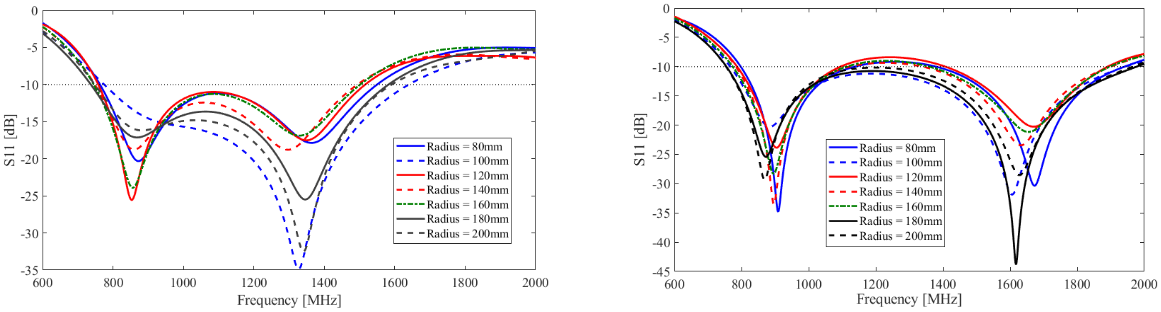

(a) (b)

Figure 4-9 LB antenna-I positive full bending effect on S-Parameters, (a) PET and (b) PF-4.

Compared to a positive full bent, the negative curvature diminishes the PET antenna bandwidth by impacting the lower frequency. Despite one bending case (bend radius = 120 mm), the antenna generally keeps its integrated bandwidth secure for negative full bent, Fig. 4-10 (a).

For the PF-4 antenna, unlike full positive bending, the antenna keeps its wideband bandwidth in full negative curvature except for the lowest bend radius = 80 mm, Fig. 4-10 (b). The lowest curvature, 200 mm, has the minimum S_{11} (around -50 dB at 1.6 GHz) with one extra resonant frequency at 1.75 GHz. Generally, the resonant frequency value rises by increasing curvature at both antenna's resonant frequencies.

Referring to Fig. 4-11 (a) for semi-bent, a distinguishable trend is observed for the PET antenna; by increasing the curvature of the antenna, the bandwidth shifts toward higher frequency and the main resonant frequency. The S_{11} value at the resonant frequency increases from -32 dB at 1324 MHz to -21 dB at 1466.5 MHz.

The PF-4 S_{11} parameter is almost immune toward semi-bent effects. Even the harshest 80 mm bend radius does not affect the operational frequency, Fig. 4-11 (b). Studies with similar findings suggested that utilizing PF-4 substrate is a viable option for creating flexible antennas [150, 151] and achieving high efficiency in the non-planar situation at 5.8 GHz [152].

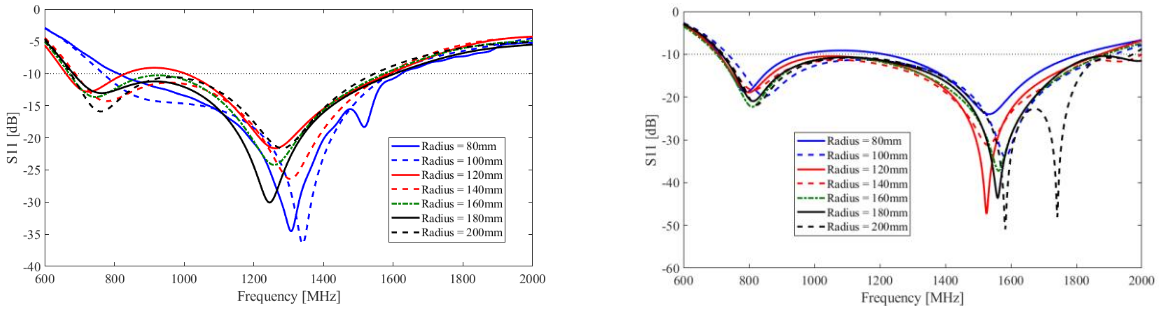

(a) (b)

Figure 4-10 LB antenna-I negative full bending effect on S-Parameters, (a) PET and (b) PF-4.

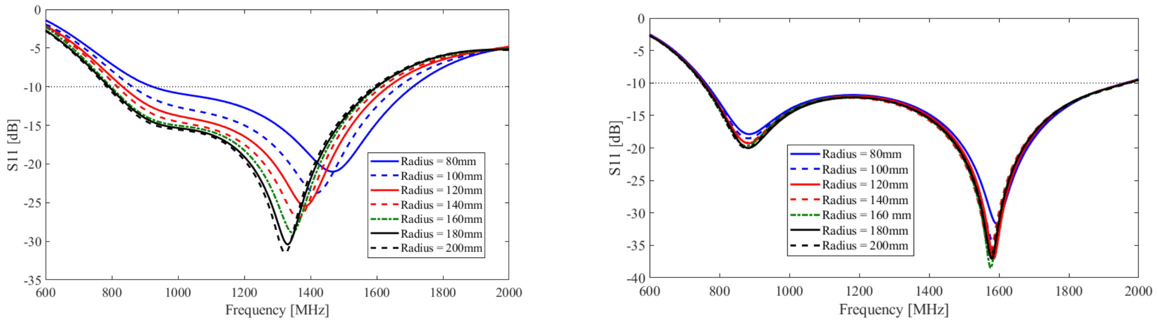

(a) (b)

Figure 4-11 S_{11} variation semi-positive bending; (a) PET and (b) PF-4.

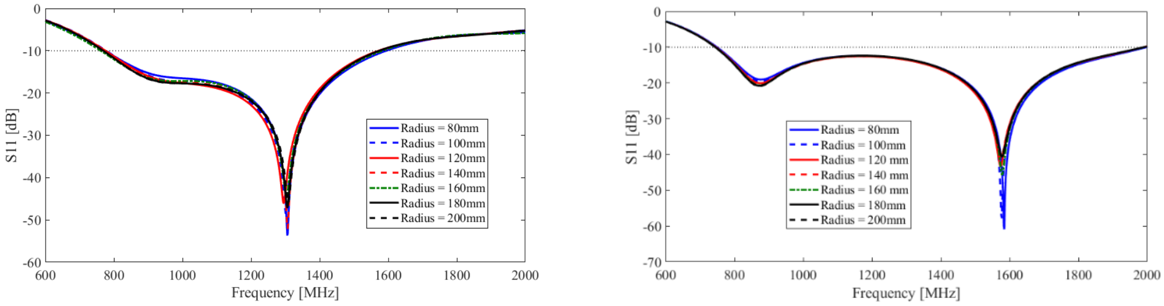

(a) (b)

Figure 4-12 S_{11} variation for antenna semi-negative bending; (a) PET and (b) PF-4.

The PET antenna has a stable bandwidth for semi-negative bending in contrast to its bandwidth shifting trend in positive bending, Fig. 4-11 (a) vs. Fig 4-12 (a). The main resonant frequency firmly locates at 1.3 GHz with a S_{11} lower than -45 dB in all positions.

The same behaviour is observed for PF-4 bandwidth in semi-negative bending. The antenna bandwidth is secure to bend without degradation, Fig. 4-12 (b). The 80 mm bend radius has the lowest S_{11} (-60 dB). Compared to other bending scenarios, the antennas have the lowest bandwidth variation for semi-negative curvatures.

Because the 100 mm curvature has the least destructive effect on the antennas' bandwidth for all positions, this specific value was retained for future fabrication.

After reviewing the curvature effects on different substrates, and to further investigate the design of the two LB antenna-I (one on PET another on PF-4), two conductive materials were considered in fabrication process: copper and aluminum. These two conductive materials have been chosen due to their many applications in textile and flexible electronics [153]. The aluminum sheet is significantly more flexible than copper [154], and this specification is very interesting in flexible circuits [155]. On the flip side, aluminum requires a very specific type of flux and soldering techniques [156], which can damage the organic substrate due to high temperatures. Also, using copper or aluminum sheets in flexible circuits have unneglectable resistivity [157].

Some researchers have studied the behaviour of such conductive material at high frequencies [158]. However, to the best of our knowledge, there is no specific comparison between aluminum and copper performance in monopole antennas with the substrates used in this thesis. It is then worth to conduct some tests to highlight their respective advantages and disadvantages. Yet, since it is not the focus of this thesis, only S-parameters comparisons will be presented and the most suitable conductive material retained for the next prototype, i.e., LB antenna-II.

To measure the antenna S_{11} parameter in a curved status, a quarter cylinder made out of cardboard and with a radius of 100 mm, was fabricated. To reduce the effect of the cylinder on the measurement results, a circular slot mesh pattern was cut out from the cylinder (Fig. 4-13).

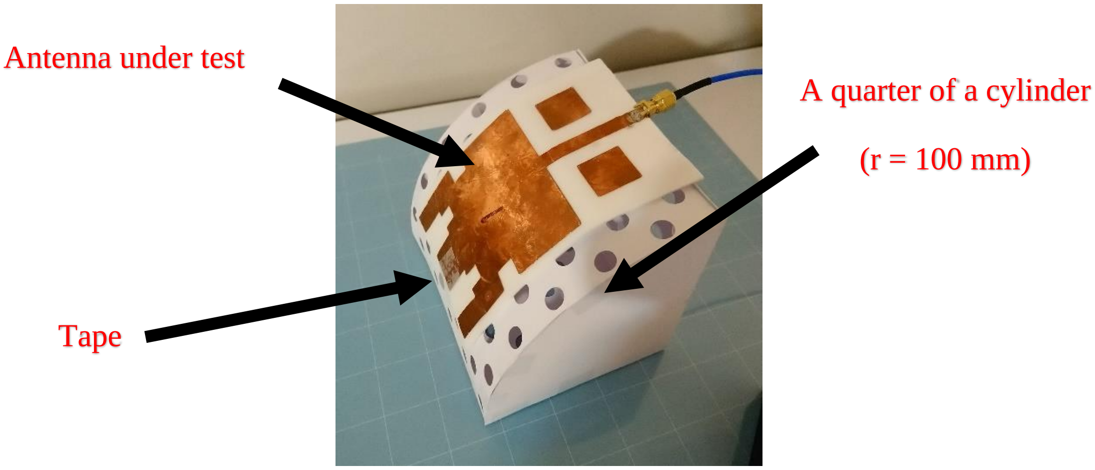

Figure 4-13 Measurement setup at 100 mm bend radius position

S_{11} parameter of the flexible antennas was measured in 100 mm bend radius, Fig. 4-14 to Fig. 4-17. The measured data exhibit a good agreement with the simulated ones. Compared to the copper antennas, the aluminum ones are more flexible. However, on the flip side, soldering a SMA connector to the aluminum requires much higher temperature (compared to copper) [159]. This high temperature melts and burns the antenna substrate. To avoid this, the aluminum was soldered at a lower temperature and a small holder was used to support this joint, as shown in Fig. 4-15 and 4-17.

As a result of soldering at an insufficient temperature, the SMA connection in the aluminum antenna deteriorated, affecting the antenna's performance, as some measured S_{11} of the aluminum antennas are above - 10 dB reference dashed line (Fig. 4-17) for the semi-negative bending case. The copper-based antennas have a more stable measured wide bandwidth for all bending positions, Fig. 4-14 and Fig. 4-16.

The minimum $S_{11} < -50$ dB was measured for the copper – PF-4 antenna. Note that if the antenna's lower and higher frequencies changed vs. the antenna position, the antenna covers some absolute wide bandwidth in all statuses. The copper PET antenna measured bandwidth covers from 840 MHz to 1630 MHz, i.e., a fractional bandwidth percentage of 64%. The copper PF-4 antenna covers the band 830 MHz – 1930 MHz (fractional bandwidth of 80 %).

The copper-based antenna exhibits a more stable single bandwidth, whereas some measurements of the aluminum antennas have shown that the bandwidth is divided into two parts. The measured bandwidth of the PF-4 antenna was wider compared to that of the PET antenna. Additionally, the PF-4 substrate is physically more flexible than the PET substrate.

Therefore, based on these investigations, the PF-4 substrate was chosen, and copper sheet was selected as the conductive material.

At 0.97 GHz, the measured bandwidth during semi-negative bending is almost equal to the S_{11} margin of -10 dB . On the other hand, during semi-positive bending, the bandwidth is maintained, but the antenna takes on a semi-bent shape that is not well-suited to our Model IV. As a result, opting for the full-bent configuration would be a better choice.

Also, the negative full bending exhibited a superior bandwidth performance at various bending radii when compared to positive bending for the copper–PF-4 antenna. Additionally, the measurement data revealed that the full positive bending configuration approached a return loss of -10 dB within the frequency range of 1.5 GHz to 1.8 GHz, as illustrated in Fig. 4-16 by the blue dash dot graph. Therefore, when considering the full bending scenario, the negative bending configuration appears to be the better option.

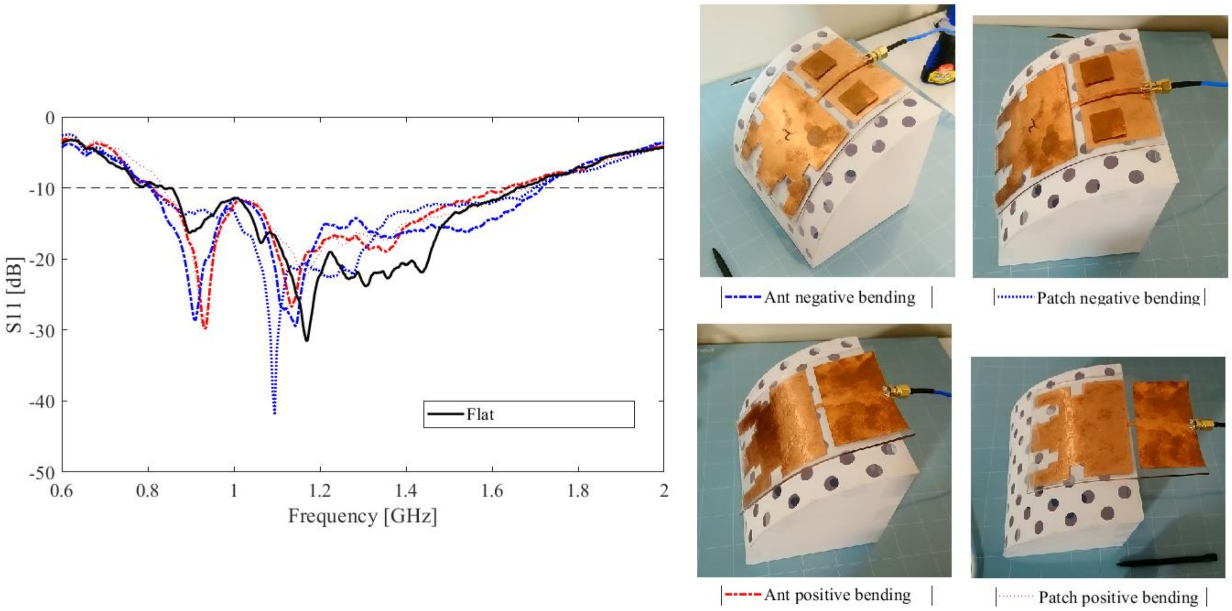

Figure 4-14 Measured S_{11} of PET – copper LB antenna-I

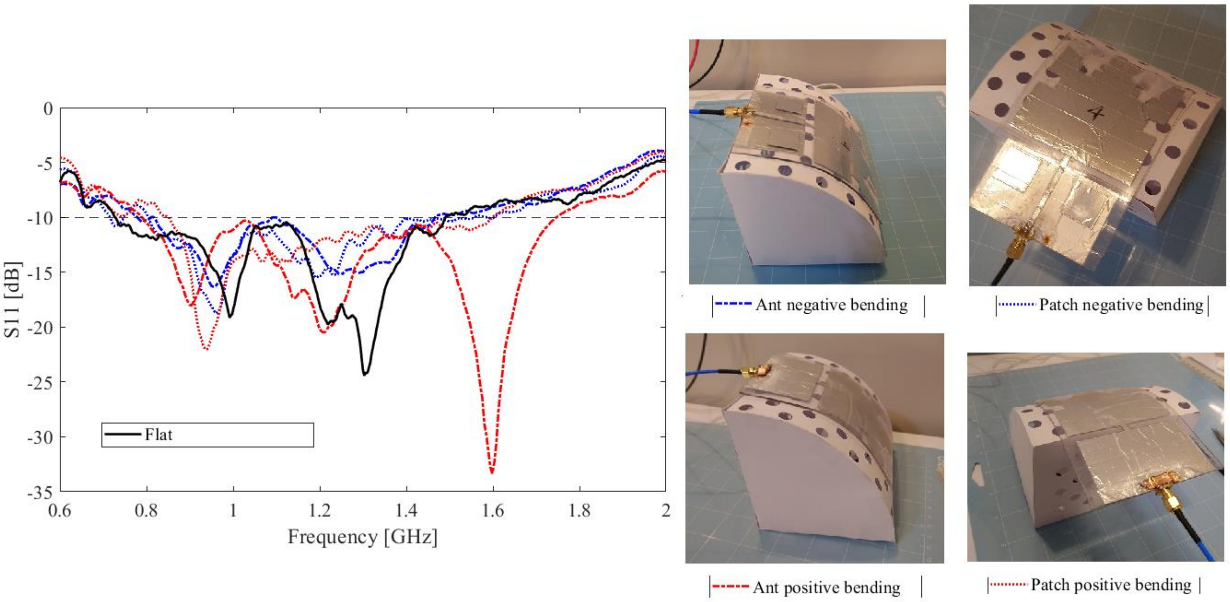

Figure 4-15 Measured S_{11} of PET – aluminum LB antenna-I

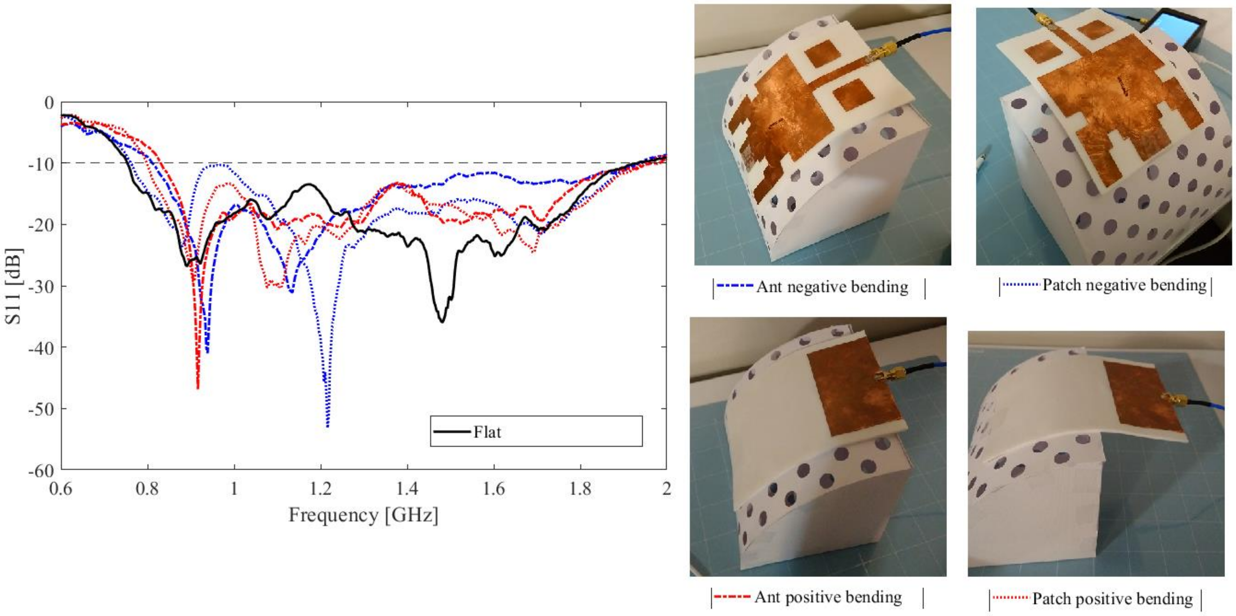

Figure 4-16 Measured S_{11} of PF-4 – copper LB antenna-I

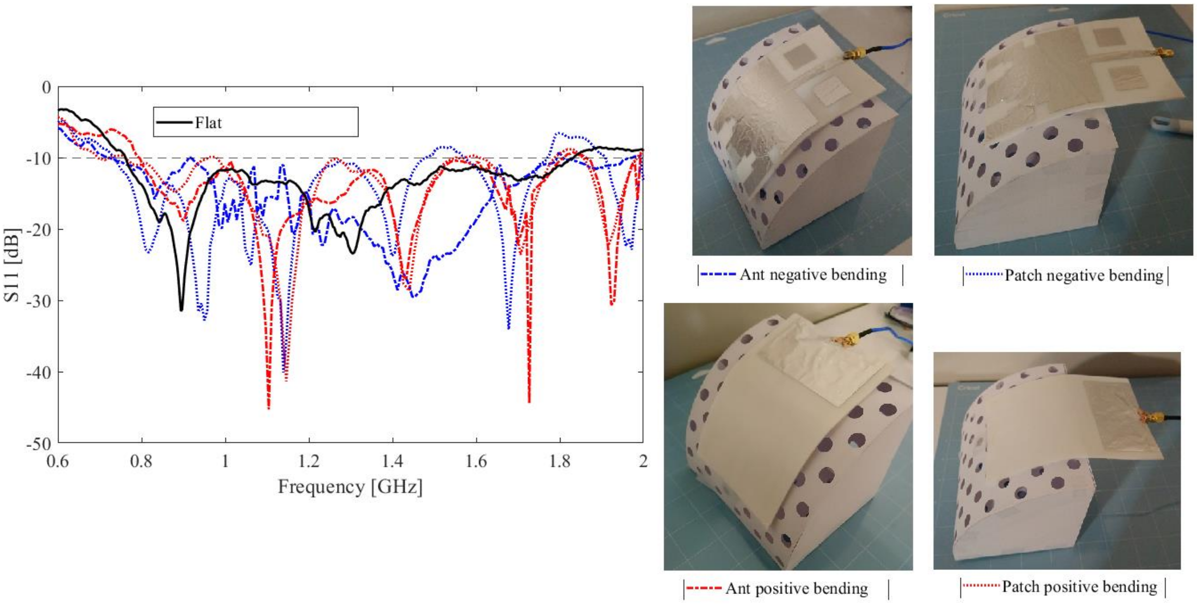

Figure 4-17 Measured S_{11} of PF-4 – aluminum LB antenna-I

4.1.2. High RCS L_{band} Antenna Design (LB Antenna-II)

By evaluating the initial prototypes (LB antenna-I) in the previous section, it was found out that the PF-4-based antenna keeps a wider bandwidth under virtually all studied bending conditions. Meanwhile, the fabrication process and the measurements showed the advantage of using PF-4 substrate instead of the PET one, in terms of flexibility and lightweight. The foam structure of the substrate helps to shape the antenna as close as the required cylindrical reflector. On the other hand, the low loss tangent of this substrate (0.0001) [160] is desirable for designing the upper band dielectric-metal reflectors with low losses. As for the conductive material of the antenna, copper works more reliably than aluminum.

The obtained conclusions from section 4.1.1 are thus used in designing the prototype LB antenna-II: the antenna substrate is PF-4, the conductive part is copper, and the bending position is a full-negative one.

The LB antenna-II (Fig. 4-18) is equipped with metamaterial, backside plate resonators and 9 × 9 rectangular elements. The designing process is sketched in Fig. 4-19.

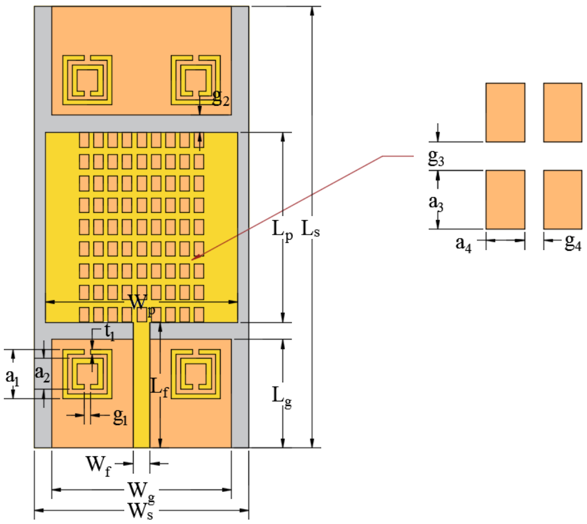

Figure 4-18 PF-4-based LB antenna-II

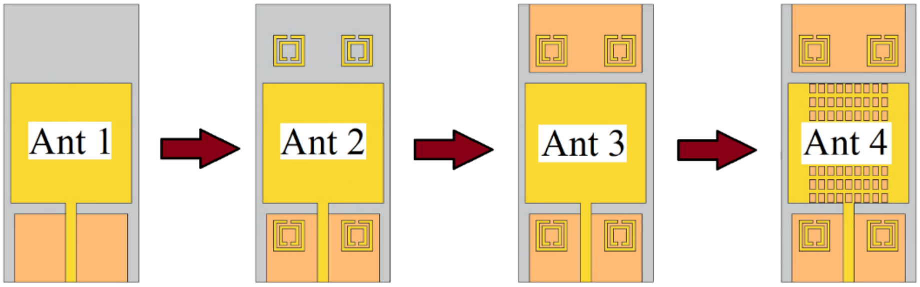

Figure 4-19 LB antenna-II design steps

The first step, illustrated by the sample “ANT-1”, was designed based on the specifications of the L_{band} antenna (Model IV), a half-ground patch antenna on the 1.6 mm PF-4 flexible substrate. Its dimensions are those of LB antenna-I, except for the substrate length: $W_p = 78 \times L_p = 77$ mm^2. Other antenna parameters are $W_s = 87$ mm, $W_f = 7$ mm, $a_2 = 12$ mm, $L_f = 51$ mm, $t_1 = 2.25$ mm, $L_s = 179$ mm, $g_2 = 7.15$ mm, $g_3 = 2.95$ mm, $a_3 = 5.9$ mm, $a_4 = 3.88$ mm, $g_4 = 1.94$ mm, $a_1 = 20$ mm, and $g_1 = 2.5$ mm.

By adding four rectangular metamaterial elements, “ANT-2” was obtained. These elements were added to slightly enhance the higher frequency and to improve the minimum return loss at the resonant frequency (Fig. 4-20 (a)), a similar approach was carried out in [105]. As can be seen from the figure, the resonators improve the antenna's higher frequency by 135 MHz (increased from 1927 to 2062 MHz) as well as obtaining a $S_{11} < -40$ dB at the antenna's second resonance frequency.

In fact, metamaterials can improve antenna bandwidth by enabling the design of antennas with unique electromagnetic properties that are not found in naturally occurring materials. Metamaterials are engineered materials with a structured composition that can be designed to exhibit specific electromagnetic properties, such as negative permittivity or permeability [161]. These properties allow metamaterials to control the flow of electromagnetic waves in unique ways, enabling the design of antennas with improved bandwidth compared to antennas made from conventional materials.

Overall, the use of metamaterials in antenna design offers the potential for significant improvement in antenna performance, including increased bandwidth [162], improved gain [163], and reduced size [164]. Several studies on metamaterial antennas [165] and resonant metamaterial antennas [166] have been done. However, a thorough analysis of their behaviour is beyond the scope of this thesis. Nevertheless, to exploit the benefits of these studies and enhance the bandwidth of "ANT-1", a similar approach as the one used for the flexible Kapton-based MMW antenna [105] was applied here.

Next, in "ANT-3", a rectangular plate, of same size as the ground, was added to the back of the antenna to establish symmetry in the reflector structure and, subsequently, to enhance the RCS of the reflector by increasing the number of reflective areas. Finally, in the final prototype, "ANT-4", 9 × 9 rectangular reflectarray elements located on the back side of the radiation patch were included, resulting in an improvement in the U_{band} gain (Fig. 4-20 (c)).

In fact, these elements will act as reflectarray elements for the U_{band} antenna. The patches were designed to resonate at 25 GHz as mentioned in Chapter 3 (FR2 5G band). However, it is important to not interact destructively with the L_{band} antenna performance and not reduce the bandwidth. As shown for ANT-4, these elements improved slightly the L_{band} antenna lower frequency (> 10 MHz).

As mentioned above, the RCS of the designs displayed in Fig. 4-19 increases from ANT-1 to ANT-4 (Fig. 4-21). Here, the upper band antenna is placed in the center axis of the lower one. Ant 1 has a 43% lower RCS compared to a full ground-size microstrip antenna while ANT-4 has 55 % higher RCS compared to the full ground microstrip antenna (Model III). The drop in the antenna RCS has a damaging effect on the antenna upper band gain. In fact, the rectangular plate designed on the back of Ant 3, of same size as the antenna ground, has greatly improved RCS of the antenna. Adding this conductor plate to the antenna made the structure symmetric to the horizontal axis.

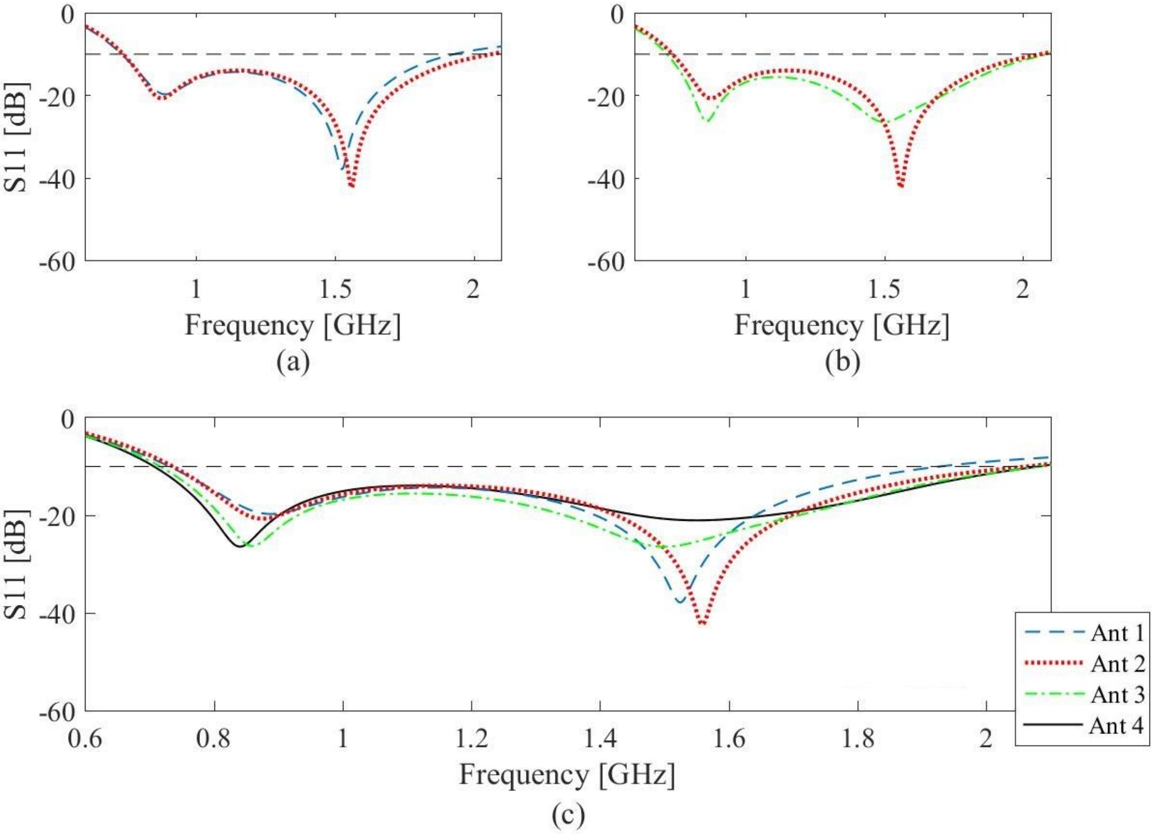

Figure 4-20 S-Parameters of proposed LB antenna-II design stages; (a) ANT 1 and 2, (b) ANT 2 and 3, (c) All ANTs

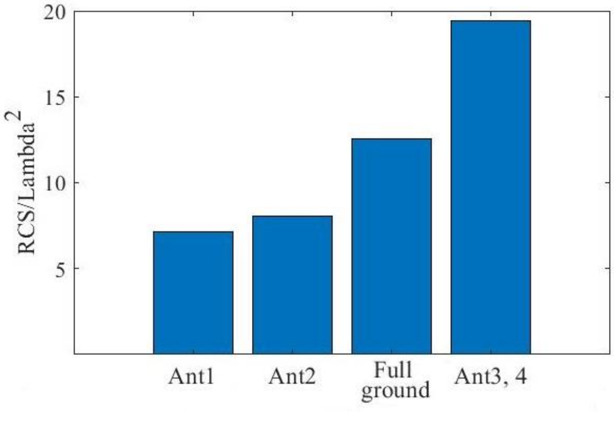

Figure 4-21 RCS of LB antenna-II variants as compared to this of a microstrip antenna with full ground

4.1.2.1. Antenna Blockage

Signal blockage in antenna refers to a situation in which an object or obstruction physically blocks or obstructs the path between the antenna and the source/receiver of the signal, causing a reduction or interruption of the signal strength or quality. This obstruction can be caused by a variety of factors, such as buildings, mountains, trees, vehicles, or any object in the way of the antenna radiation path. The antenna blockage is not solely limited to large objects, as even the presence of small objects near the antenna can cause a blockage [167].

Signal blockage can result in signal attenuation, which refers to the weakening or reduction in the strength of the signal due to the obstruction. This can lead to a degradation in the quality of the signal, which can manifest as dropouts, distortions, or complete loss of radiated signal form antenna.

For instance, an antenna that receives signals from geostationary satellites in orbit, can experience signal blockage due to small objects such as leaves, branches, and bird nests. Unpredictable signal blockages represent an inherent aspect stemming from the interaction of users with handheld [168] and MMW wireless devices [169].

In Model IV, the U_{band} antenna is an obstacle while the L_{band} radiates. The attenuation of radiated waves caused by the obstruction of multiple transmission paths arriving from the direction of an obstacle can be interpreted as a modification in the radiation pattern of the antenna [167].

Therefore, the next step will be to focus on the signal blockage issue when this antenna will be part of the Model IV structure configuration.

An isotropic antenna is a theoretical antenna with an equal radiation pattern and intensity in all directions. The antenna efficiency is theoretically of 100%. In this case, the isotropic antenna directivity is constant to 1 (0 dBi) all around the antenna [124].

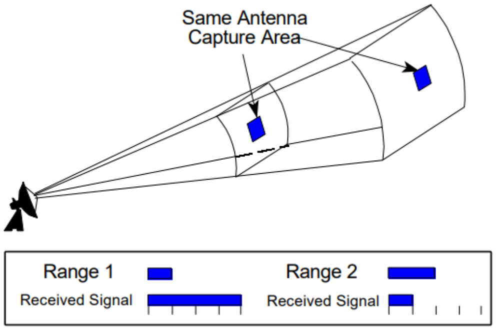

Figure 4-22 Power density of the antenna at different distances [170]

For the isotropic antenna, the power density at distance R from the radiating antenna is [170]:

$$P_D = \frac{P_t}{4\pi R^2} \qquad (4\text{-}1)$$

Where P_t is the transmitted power (Fig. 4-22). In general, for an antenna with gain G_t, the power density from the radar antenna P_D is:

$$P_D = \frac{P_t G_t}{4\pi R^2} \qquad (4\text{-}2)$$

The power density drops by increasing the distance from the antenna ($1/R^2$ in the above equation). In our models, at L_{band} operation, the power density at the U_{band} antenna depends on the gain of the lower-band one (G_t in equation (4-2)), and on the distance (R in equation (4-2)).

As illustration, if the power density at the U_{band} antenna versus the distance from the L_{band} one is plotted in Fig. 4-23, it can be seen that, at a frequency of 2.4 GHz for instance, the received power density at the upper band antenna drops significantly after around a distance of 5 cm between the two antennas. Increasing this power means more radiated signal will be blocked by the upper band antenna. Thus, from here, the minimum distance between the two antennas will be set as > 5 cm.

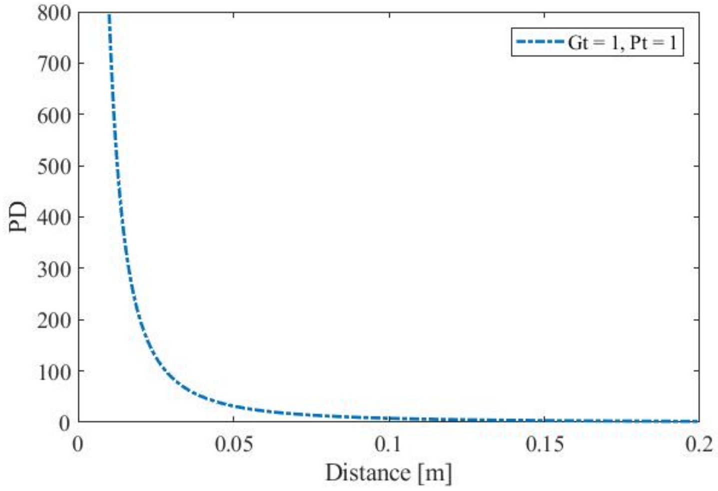

Figure 4-23 Received power at upper band antenna versus distance (according to Equation 4-2)

4.1.2.2. LB antenna-II Parameters

Because of using an organic substrate, flexible antenna dielectric properties may change by bending and applying tension to the antenna [171]. If pressure is applied, it will make the substrate denser and change the substrate thickness, dielectric constant, and loss tangent. Note that the substrate data sheet was setup in a flat situation by the company [160].

Therefore, these changes are studied on the PF-4 substrate to check their impact on the antenna response. If these changes cannot decline the antenna performance, then the proposed LB antenna-II design is a good candidate for the final prototype.

First, the substrate thickness was investigated. The flexible foam-based substrate has a soft structure and air cavities; its thickness being not rigid, it can change under bending.

LB antenna-II return loss and gain were studied for a wide variety of substrate thickness (h), from 1.4 mm up to 1.8 mm by 0.05 mm step size (9 samples). The results are presented in Fig. 4-24 and 2-25, respectively. The antenna has two resonant frequencies. By reducing the thickness of the substrate, the first resonant frequency S_{11} decreases from -20 to -40 dB and the second increases from -30 to -15 dB. The most important values here are the lower and upper frequencies that define the bandwidth. The lower frequency remains fixed at ~ 0.71 GHz. But the upper one slightly shifts to the lower values as the thickness is decreased. This is a negligible variation since the upper frequency is located at > 2 GHz for the thinnest studied substrate.

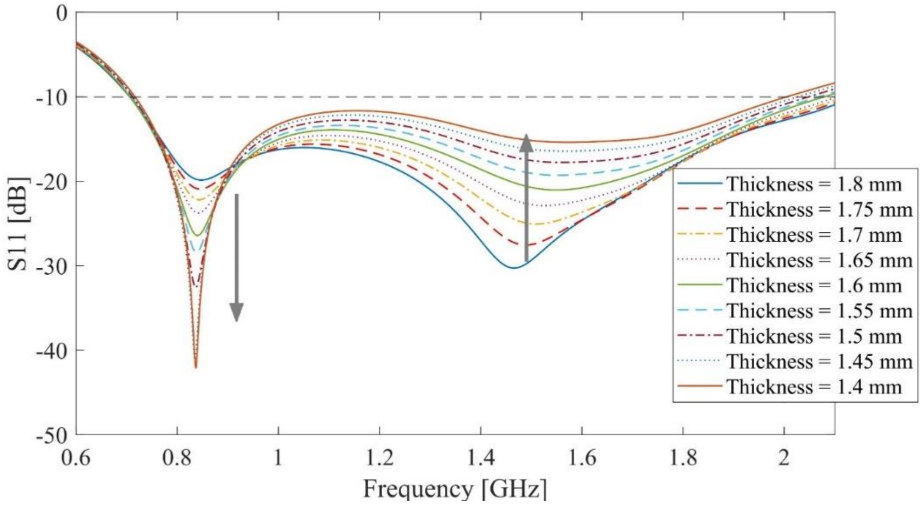

Figure 4-24 S_{11} of the LB antenna-II for different substrate thicknesses

Globally, the antenna maximum gain increases by decreasing the substrate thickness, Fig 4-25. In the second half of the bandwidth, this change is more noticeable. However, this is a very low fluctuation, e.g., at 2 GHz, the deviation observed in the gain is less than 3 % compared to the 1.6 mm thickness substrate.

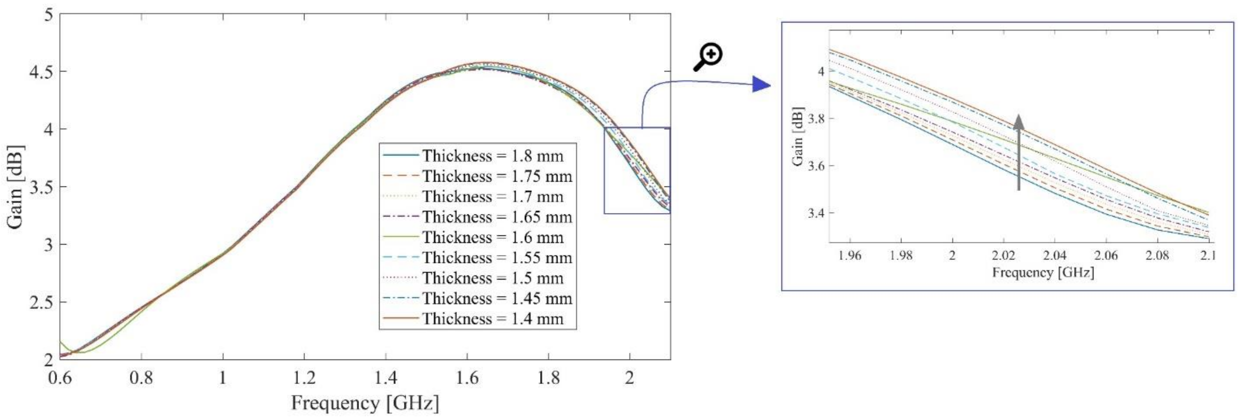

Figure 4-25 LB antenna-II gains for different substrate thicknesses

The dielectric constant value was also varied from 1 to 1.3 to analyze its effect on LB antenna-II performance. As illustrated in Fig. 4-26, for the first resonant frequency, S_{11} goes down while for the second one, it jumps up to a higher value by soaring dielectric constant. However, even if increasing this constant will reduce the higher frequency, this latter reminds > 2 GHz. The aim of this graph was to verify that the antenna bandwidth does not shrinks if the substrate density changes by applying pressure or by bending it during fabrication. In fact, changes in substance density result in changes in the epsilon value [172]. J. Bor investigated the changes in the dielectric constant and tangent loss of a foam substrate by compressing and decompressing it while applying gas pressure. The results showed that changes in the dielectric properties could be observed and measured. By varying the density of the foam substrate, J. Bor was able to explore how changes in its physical structure affected its dielectric properties [172].

For the H-Divinycell foam, a density range of 30 to 250 kg/m3 was tested by applying pressure, resulting in a change in dielectric constant from 1.05 to 1.3. For another foam, i.e., the HCP-Divinycell foam, a density range of 200 to 400 kg/m3 was tested, and a dielectric constant change from around 1.2 to 1.45 was observed [172].

A similar study was performed by V.T. Morgan, who investigated the dielectric dispersion of a flexible substrate in relation to mechanical pressure and presented experimental results [173].

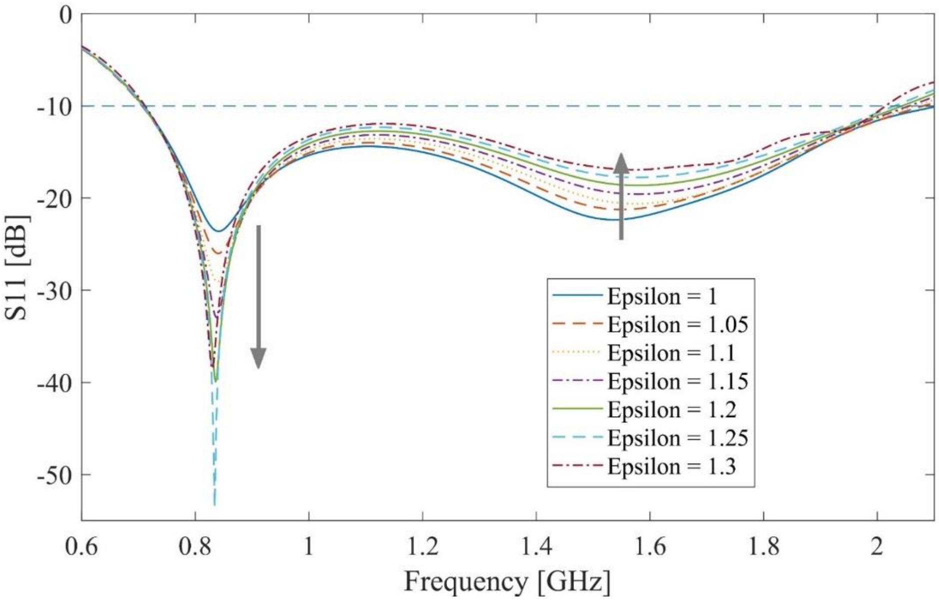

Figure 4-26 LB antenna-II S_{11} for different substrate dielectric constant

The dielectric constant has more effect on the gain than the thickness, especially after 1.6 GHz, Fig. 4-25 vs 4-27. The gain drops by increasing epsilon from 1 to 1.25. After that, starting for 1.3, the gain does not change with this trend. The maximum gain fluctuates less than 1%.

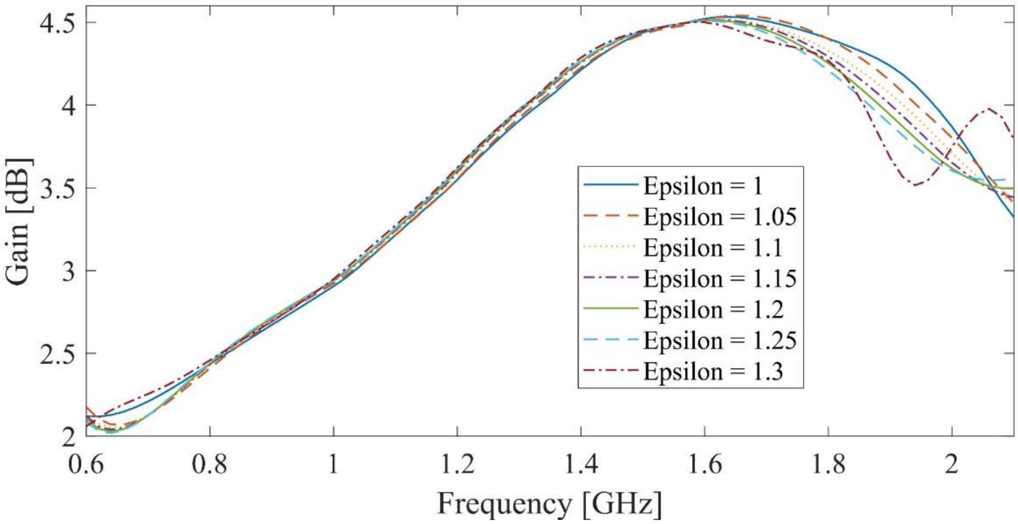

Figure 4-27 LB antenna-II gain for different substrate dielectric constant

The loss tangent was varied from 0 to 0.005, step size of 0.001, and its effect on the return loss and gain is shown in Fig. 4-28 and 4-29, respectively. The loss tangent change has the lowest effect on LB antenna-II performance, compared to the thickness and dielectric constant. The antenna performance is immune to the loss tangent variation. The resonant frequencies remained constant at around 840 MHz and 1550 MHz. The gain changes insignificantly in the higher and lower frequencies.

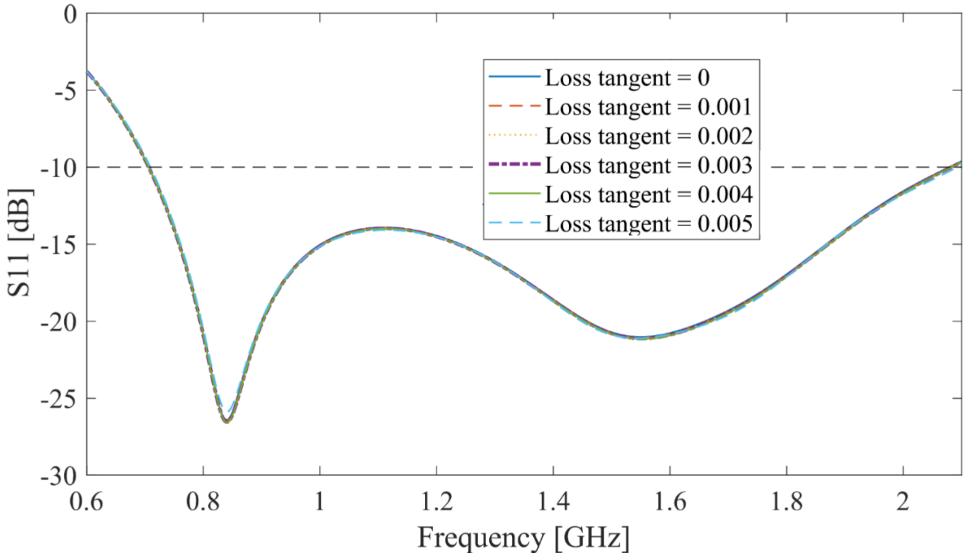

Figure 4-28 LB antenna-II S_{11} versus loss tangent

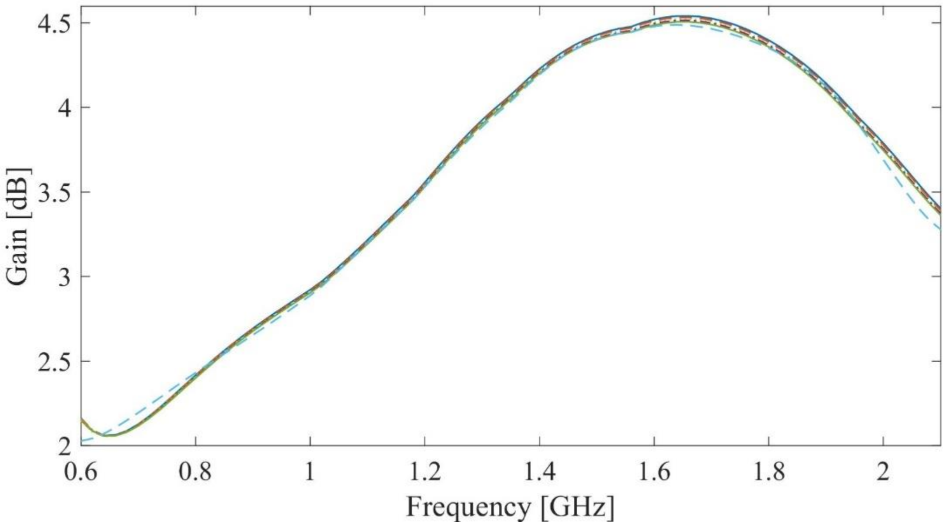

Figure 4-29 Changes in gain over various loss tangent, LB antenna-II

4.1.2.3. Cylindrically Curved LB Antenna-II

For simplifying the design and focusing more on the research goal, LB antenna-II was shaped as a cylindrical reflector, instead of a parabolic. However, the fundamental of this study could be extended to other reflector shapes: parabolic, flat, corner, etc. Based on the studies presented in section 4.1.1.2, the bending condition of the reflector (here the LB antenna-II) was selected as a complete negative bend, i.e., the case c in Fig. 4-8. In this case c, the reflector is symmetric and the LB antenna-II microstrip feed line is protected from the U_{band} antenna interface and noise by its ground, which is, from the U_{band} view, a cylindrical reflector. The 4-element metamaterial resonators are not supposed to work at U_{band} frequency band, so hiding them behind the copper plate is advantageous.

LB antenna-II is shaped as a cylindrical reflector over an imaginary cylinder, Fig. 4-30. The cylinder radius determines the reflector curvature and, as discussed in section 2.2, the focal feed point location. Generally, by increasing the radius, the L_{band} antenna performance is closer to its flat design. The microstrip feed line transfers the input signal with lower distortion.

On the other hand, a larger radius increases the reflector effective area and the D parameter. But on the flip side, it increases the focal point distance and makes the proposed antenna physically large. Moreover, it helps reducing the two antenna interfaces.

Bandwidth over a wide range of bending radii from 100 mm to 200 mm with a step width of 10 mm was studied in Fig. 4-31. There were no changes observed in the studied bandwidth as the bending radius was varied. The presented S_{11} graphs in Fig. 4-31 have a similar shape with a slight change in the amount of the resonant frequency. LB antenna-II lower and upper frequencies are set at ~770 MHz and ~1925 MHz, respectively. Within the range of bending radii examined in this study, the bandwidth of the antenna remains relatively stable and exhibits no significant alterations, Fig. 4-31. This outcome can be attributed to the findings in section 4.1.1, where suitable antenna substrate and bending position were identified as the factors that contribute to bandwidth stability, regardless of the degree of bending radius. In fact, in that section, we studied different possible bending positions and two substrates. We chose the substrate and the bending position that show the lowest effect on the bandwidth. Then we used that bending position and substrate to design the LB antenna-II.

As a matter of fact, a small radius causes a severe bending of the cylindrical antenna, whereas a larger radius results in a bigger overall size of the reflector antenna due to the direct relation between feed location and bending radius [174].

In fabrication and measurement process, when a sheet of flexible material is bent hard, the outside top and bottom surfaces experience elongation and compression, respectively. This is because the material on the outside of the bend must stretch to accommodate the change in shape, while the material on the inside of the bend is compressed [175]. Severe bending of the L_{band} antenna can cause the top and bottom conductive material to detach and shift from their original positions.

Therefore, the four top and bottom values of the bending radius range were excluded during the selection process. Among the left radii values, i.e., 140mm, 150mm, and 160mm, the latter exhibits a slightly lower minimum return loss at the resonant frequencies. Additionally, it has the lowest frequency within the bandwidth. So, the 160 mm was selected.

Table 4-2 summarizes all the antennas presented and studied in Section 4.1 for the L_{band} and the rationale behind their design. Finally, the LB antenna-II having bending radius of 160 mm was selected for the L_{band}, from here this antenna will be used for L_{band}.

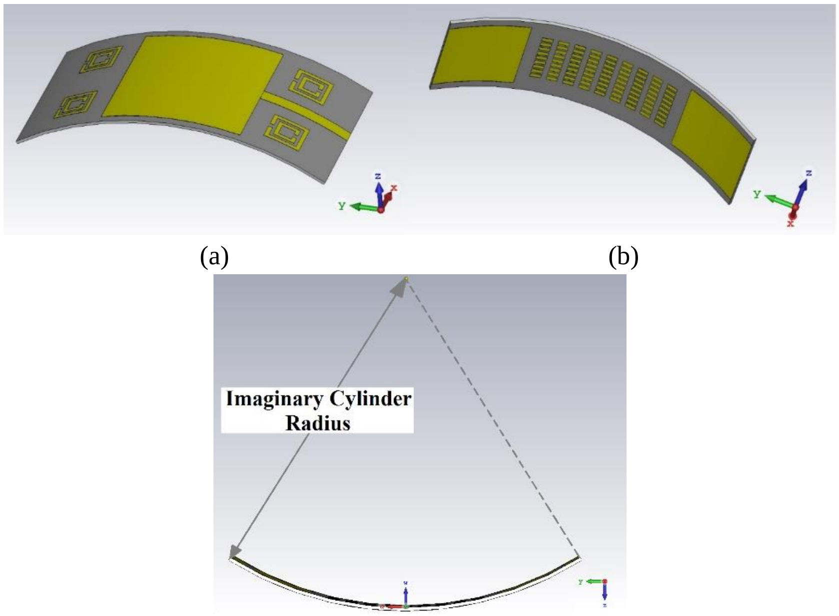

(a) (b)

(c)

Figure 4-30 Curved LB antenna-II, (a) 3D top view, (b) 3D bottom view, and (c) displayed imaginary radius

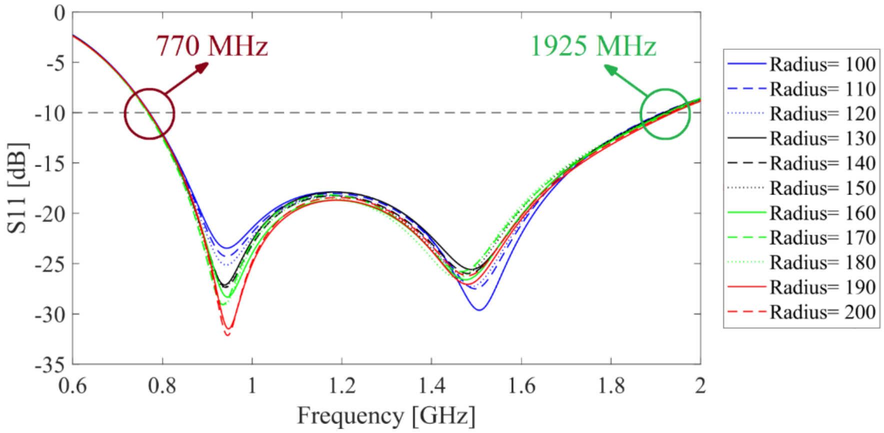

Figure 4-31 Bending LB antenna-II effect on the S_{11} parameter.

Table 4-2 Summary of the presented lower band antennas

Lower Band Antennas	**Bandwidth [MHz]**	**Study's Rationale**	**Study Output**
LB antenna-I, Copper-PET	850 - 1660	Searching for the optimal substrate and conductive materials. Identifying the ideal curvature, e.g., full-positive, …	PF-4 as substrate and copper as conductor were selected. Full-negative bend was chosen.
LB antenna-I, Aluminum-PET	720 - 1490		
LB antenna-I, Copper-PF-4	750 - 1940		
LB antenna-I, Aluminum-PF-4	750 - 1830		
LB antenna-II Flat	711 - 2100	Examine the potential impact of fabrication on the antenna's performance by studying any changes that may occur in the substrates.	The antenna's performance is not affected by fabrication tolerances.
LB antenna-II Curved	770 - 1925	Find the bending radius.	A bending radius of 160 mm was chosen.

4.2 MMW Horn Antenna Design

Once the design of the LB antenna-II was completed and the 160 mm bending radius selected, its reflectivity as a U_{band} reflector should be investigated. To study the reflectivity, having a horn antenna as far field reference is a widely used method [176].

So, it is first necessary to design a standard horn antenna at the U_{band} frequency. CST Microwave Studio software has a standard horn antenna in its library [177]. The horn antenna from CST software library was the used as the reference horn antenna in this section. The horn antenna has the following dimensions (Fig. 4-32): a_{h1} = 23.7 mm, b_{h1} = 19.7 mm, a_{h2} = 9.6 mm, b_{h2} = 5.6 mm, l_{h1} = 15.77 mm, and l_{h2} = 2.19 mm.

The U_{band} horn antenna bandwidth and gain simulated in free space are presented in Fig. 4-33. The antenna bandwidth covers the studied frequency range, from 20 GHz up to 30 GHz with $S_{11} < -15$ dB. It has a 12.4 dB gain at 20 GHz. The gain increases almost linearly, reaching 14.9 dB at 30 GHz.

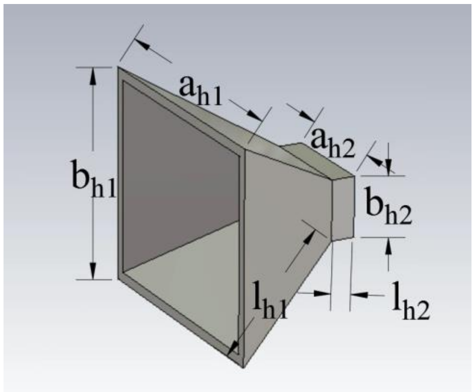

Figure 4-32 3D sketch of the U_{band} feed horn antenna

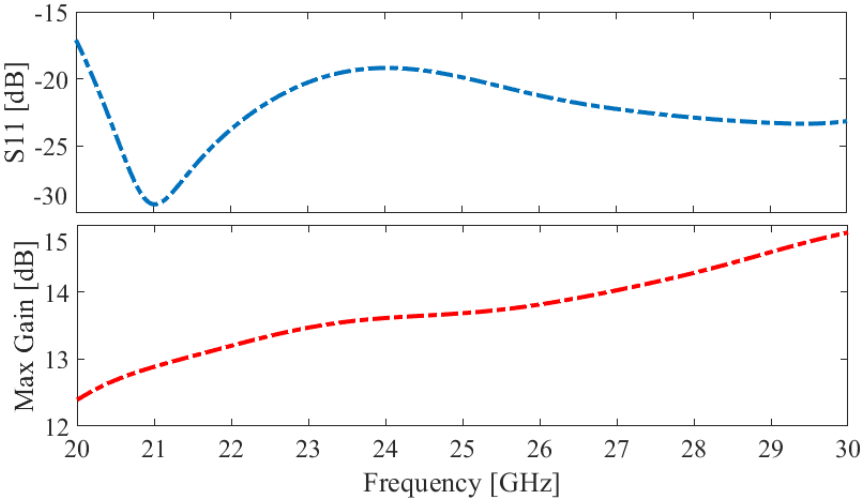

Figure 4-33 The U_{band} feed horn antenna, bandwidth, and maximum gain

4.3 LB Antenna-II Reflectivity

The standard horn antenna bandwidth and gain were shown in free space. Now, by using the antenna as the reflector feed, the effectiveness of the reflector should be studied. The reflector efficiency is determined by the difference between the gain of a standalone antenna and the gain of a reflector antenna. This approach has been used to study metamaterial reflector [178] and reflectarray [179].

The gain improvement of the reflector is determined by studying the changes in gain when the standard horn antenna is placed as reflector feed. In our model, the reflector is the L_{band} antenna, thus the entire model constitutes a dual-band antenna. The aim is to improve the U_{band} gain while maintaining its wide bandwidth and equivalent performance in the L_{band}.

4.3.1. U_{band} Antenna Location

The horn antenna was placed at a distance $F_h = {}^{Radius}/_2 + k$, far away from the curved L_{band} antenna, Fig. 4-34. Here, the term " ${}^{Radius}/_2$ " came from calculating the cylindrical focal point as the focal length of a concave spherical mirror [174]. The cylindrical reflector is obtained by cutting a spherical mirror through its axis. However, in our design, some sections of the reflector are cylindrical, while others are reflectarrays. Therefore, a parametric study is conducted on the ${}^{Radius}/_2$ distance across a range that is at least as large as the distance used in the reflectarray antenna designed by P. Jiang [180]. So the k is studied in a range of $k = \pm 12\ mm = \ \pm\lambda_{25\ GHz}$, to have an optimized location of the feed point.

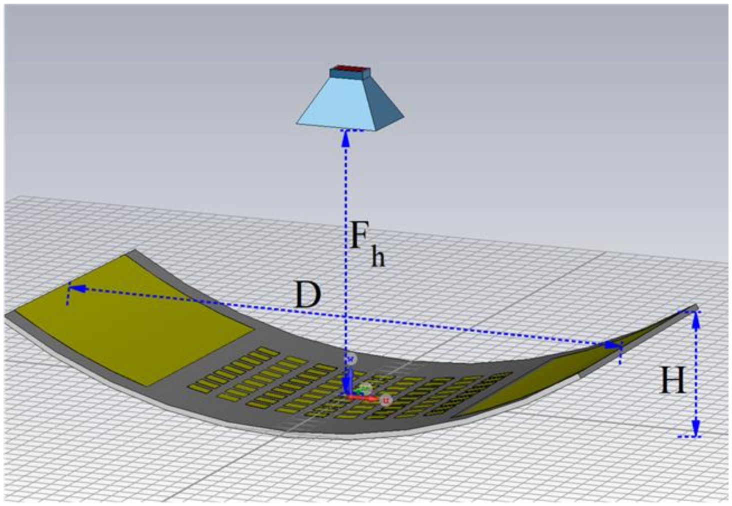

Figure 4-34 Geometry of the LB antenna-II with standard horn antenna feed

First, the bandwidth was studied as depicted in Fig. 4-35. All the studied k values giving a S_{11} lower than -10 dB. Therefore, the suitable value of k was chosen based on the maximum gain.

Referring to Fig. 4-36, decreasing the k value reduces the antenna gain. The lowest k = -12 mm has the lowest gain = 20.2 dB at 30 GHz. However, k = 4 mm has the highest maximum gain (24.7 dB) but the gain drops by more than 15 % (~ 4 dB) at the beginning of the bandwidth.

High gain was achieved with $k = 12$ and $8\ mm$ as shown by the highlighted lines. Despite having a higher maximum gain in $k = 8\ mm$, the value $k = 12\ mm$ shows less fluctuations, so it was retained. Therefore, the U_{band} antenna was placed at a distance of $F_h = 80 + 12 = 92\ mm$ far away from the curved cylindrical reflector.

The antenna integrated reflector (designed from Model IV in chapter 3) increases the U_{band} antenna minimum gain by around 8.5 dB (20.84 dB) and the maximum gain by 9.33 dB compared to the single antenna. The gain jumps from 14.9 dBi up to 24.23 dBi. Also, the proposed structure did not decrease the antenna bandwidth. It should be noted that the antenna gain without the reflectarray elements is presented in Fig. 4-37 with a dashed red line.

The designed U_{band} reflectarray elements on the L_{band} antenna allow a significantly improved gain. Without these elements, the L_{band} antenna is a cylindrical reflector with D = 170 mm and excited by the U_{band} feed. Note the PF-4 1.06 dielectric constant, the substrate does not interact with the incident and reflected waves since it acts more like air. Adding the reflectarray increases the U_{band} antenna maximum gain by 3.4 dB (Maximum gain of simple reflector 20.81 dB vs. 24.23 dB).

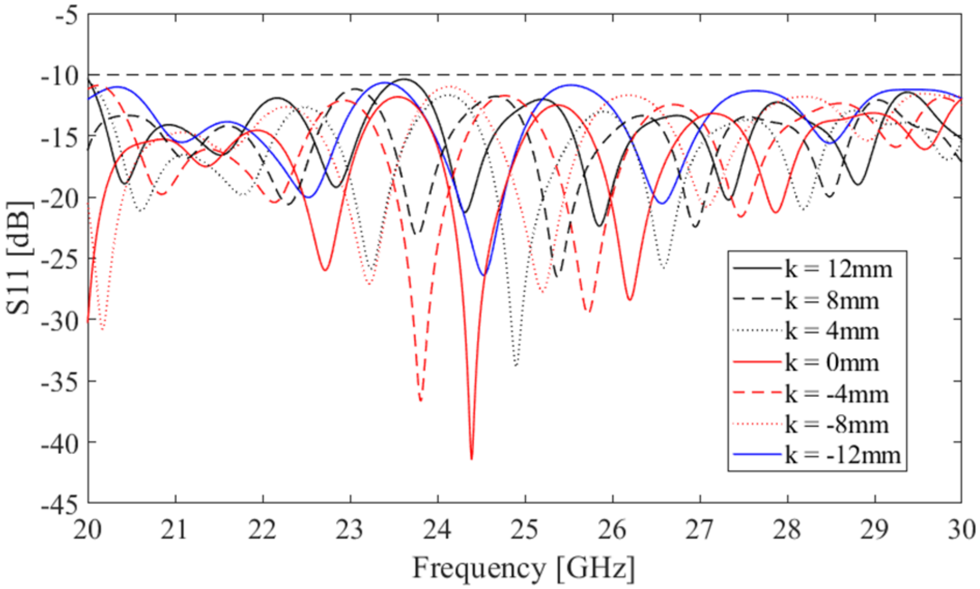

Figure 4-35 k parameter effects on the U_{band} horn antenna S_{11}

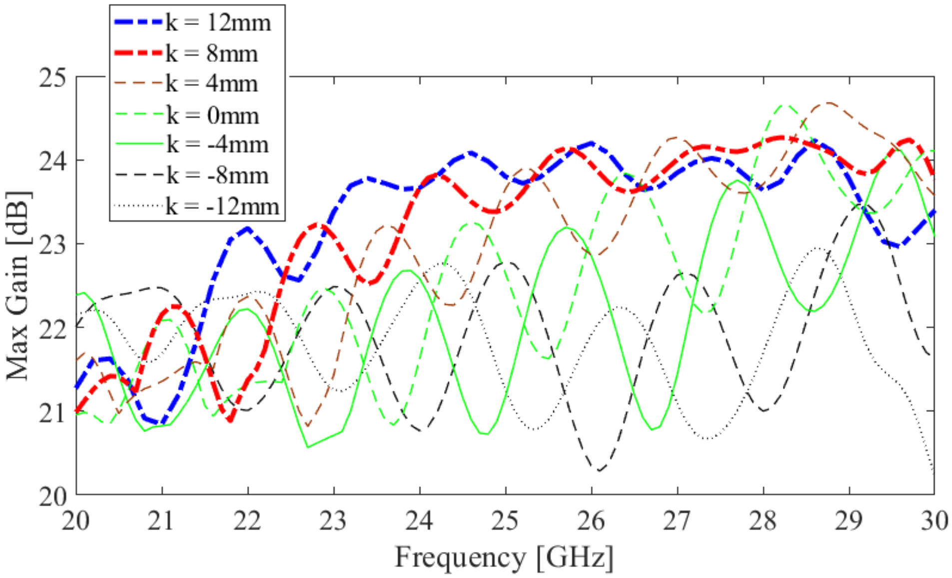

Figure 4-36 k parameter effects on the U_{band} horn gain

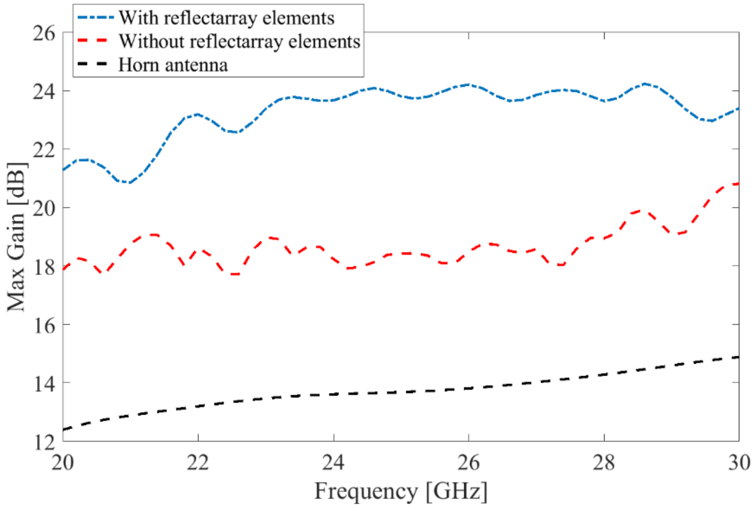

Figure 4-37 U_{band} antenna gain, single antenna, with/without reflectarray elements

4.3.2. Various U_{band} Reflectarray Elements

Four different elements were studied as reflectarray elements. The first one, Fig. 4-38 (a), was calculated by the rectangular microstrip antenna formulas (2-9) and (2-11). Another one, Fig. 4-38 (b), is a circular microstrip patch element.

The elements were designed as a circular microstrip antenna in which the patch radius R_1= 2.52 mm is calculated by [78]:

$$a = \frac{F}{\left\{1+\frac{2h}{\pi\varepsilon_r F}\left[\ln\left(\frac{\pi F}{2h}\right)+1.7726\right]\right\}^{1/2}} \qquad (4\text{-}3)$$

$$F = \frac{8.791\times 10^{9}}{f_r\sqrt{\varepsilon_r}} \qquad (4\text{-}4)$$

where f_r = 25 GHz, ε_r = 1.06, and h is the substrate thickness (in cm). The space between elements has been designed to replicate the technique employed by R. Deng [181] at a particular distance of ~ 0.2 $\lambda_{25\ GHz}$. Therefore, the distance a_1 was set to 7.56 mm.

Fig. 4-38 (c) represents closed ring circuits (CRR) reflectarray elements. The CRR radius R_2 was calculated with the following equation given by [182]:

$$R_2 = \frac{c}{2\pi f_{CRR}\sqrt{\varepsilon_r}} \qquad (4\text{-}5)$$

In this equation, f_{CRR} is the CRR element resonant frequency, and c is the speed of light in free space ~ 300,000,000 m/s. $R_2 = 1.86\ mm$ at 25 GHz and the CRR are placed at distance $a_2 = R_2 \times 3 = 5.58$ mm from each other in order to have a similar gap between elements same as in [181]. The CRR is smaller than the microstrip patch because it is not related to the substrate thickness. In this case, the substrate thickness is relatively thick.

The last studied reflectarray shape is a split ring resonator (SRR) made out of inner and outer rings, Fig. 4-38 (d). With calculated parameters from the equations provided in [183], we get R_4 = 4 mm, R_3 = 2.85 mm, and W_2 = 1.15 mm; the SRR resonates at $f_{SRR} = 25\ GHz$.

$$f_{SRR} = \frac{c}{2\pi^2}\sqrt{\frac{3(R_4-R_3-W_2)}{\varepsilon_r(R_3)^3}} \qquad (4\text{-}6)$$

The other parameters are W_1 = 0.8 mm and $a_3 = 2 \times R_4 + 2$ = 10 mm, following [181].

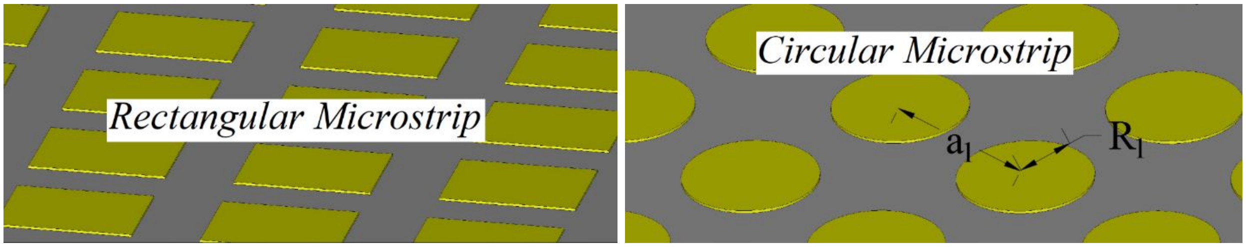

(a) (b)

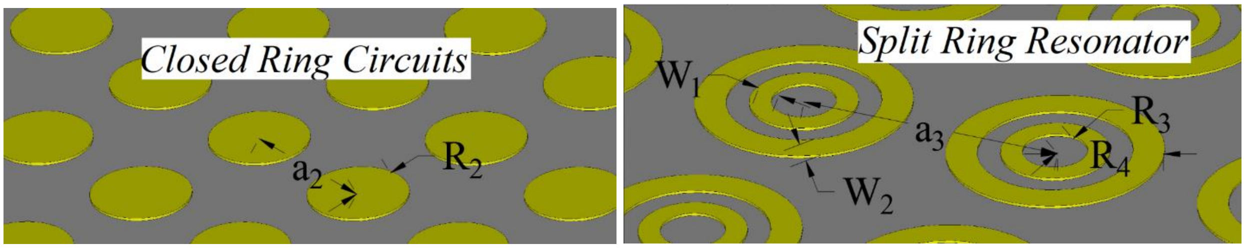

(c)

(d)

Figure 4-38 Reflectarray elements, (a) rectangular patch, (b) circular patch, (c) CRR, and (d) SRR

Choosing the right reflectarray has an important effect on the U_{band} gain; Fig. 4-39 displays this effect. In the first half of the bandwidth, the CRR has a lower gain than the circular microstrip elements. But for the second half, the CRR gain goes notably higher than the other one and reaches 23.5 dB at 29.3 GHz. Nevertheless, the circular microstrip gain slight fluctuates between ~ 19 dB and ~ 22 dB, in contrast to the ~ 20 % CRR gain drop. The lowest gain is for the SRR for the whole bandwidth, compared to the other ones.

The rectangular microstrip elements fit well into our design with a significantly higher gain than the other options. Furthermore, it has the lowest fluctuation between ~ 23 GHz and 29 GHz.

Afterwards, the number of the n×m reflectarray elements was increased as far as possible on the backside of the L_{band} radiation patch. The size of the elements and the distance between them are the same as before. In this case, 9 × 15 rectangular patches, 13 × 11 circular microstrip patches, 15 × 15 CRRs, and 9 × 7 SRRs, with 18 inner ring resonators are placed as reflectarray elements.

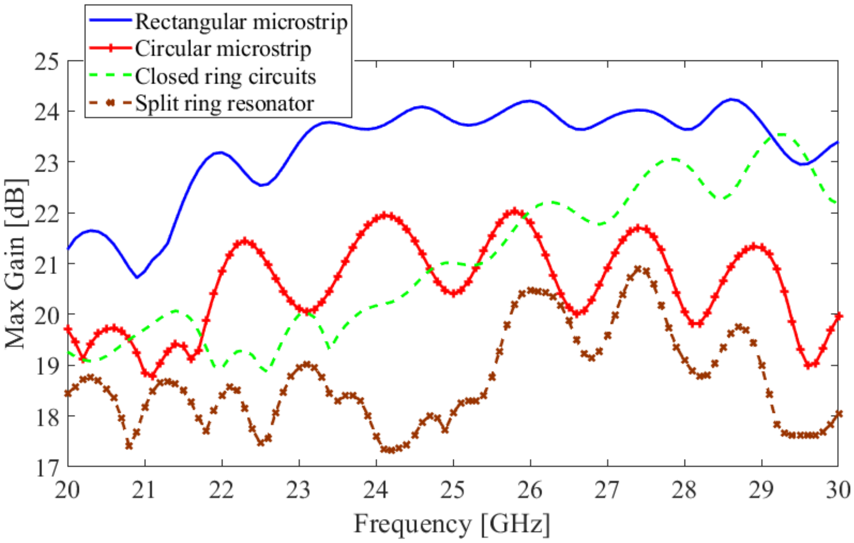

Figure 4-39 Gain variation for the different studied reflectarray elements

By looking at their gain in Fig. 4-40, it can be seen that the rectangular and circular microstrip patches have the same gain chart fluctuations. But unlike before, the circular patch has a higher gain and almost the highest value among all of them. The SRR has the greatest gain at the starting of bandwidth but the gain falls after, placing the SRR graph below the other ones and shows the lowest gain among all others.

Increasing the number of elements can enhance the gain for the circular microstrip patch shape but not so much as the 9 × 9 element rectangular ones. The antenna gain does not have a direct relation with the reflectarray elements and increasing the number of elements does not give out a higher gain. The 9 × 9 rectangular elements were selected.

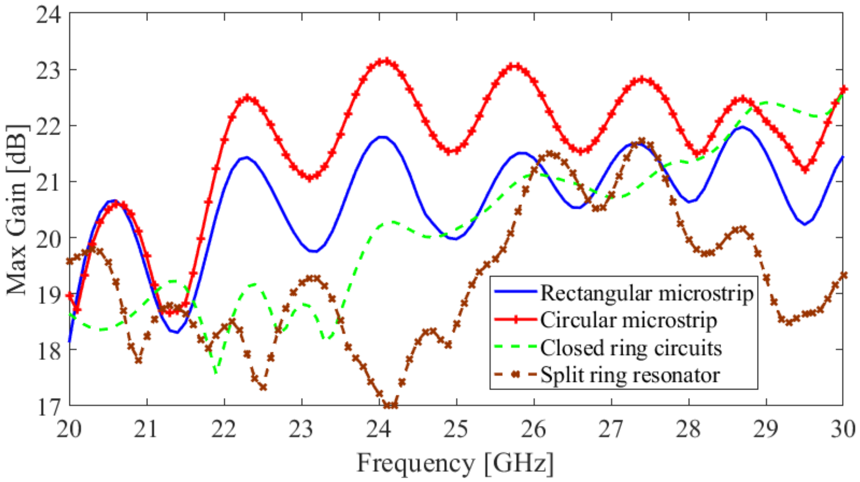

Figure 4-40 Gain variation for the fully filed L_{band} antenna by reflectarray elements

4.4 Proposed U_{band} Patch Antenna Designs

This chapter will present two final dual-band antenna integrated reflectors. Before introducing these final dual-band antennas, two U_{band} antennas will be designed for each of them. These U_{band} antennas are named UB antenna-I and II. Then, each of these UB antennas will be paired with LB antenna-II to create the two final antennas.

4.4.1. UB Antenna-I

According to Chapter 3, a half-ground monopole patch antenna is required for the U_{band} (i.e., the Model IV). The first planar U_{band} antenna, designed as feed, was a monopole antenna with the exact structure as the L_{band} antenna. The L_{band} antenna was rescaled by a factor of $\times 1/10$ to exceed the minimum FR of 8, which is claimed as one of the objectives of this study.

In fact, in antenna, it is usual to design a model of an antenna that is similar in size, shape, and material properties to the original one, in order to accurately predict its performance. The theorem states that the performance of the model should be proportional to the performance of the actual antenna, with the model's dimensions being scaled down by a factor known as the similitude factor [78] or, as designated in this context, the scale factor.

As a result, the antenna is based on a 0.16 mm thickness PF-4 substrate. It has a total size of $1/10$ of the L_{band} one and named as UB antenna-I. LB antenna-I has the same S_{11}, gain and radiation pattern as the L_{band} antenna (LB antenna-II). The only difference is that the operating frequency is multiplied by 10. It operates in the 7.2 GHz – 20.4 GHz frequency band. The reflectarray elements were deleted in the rescaled U_{band} antenna because they were designed to improve the U_{band} reflector performance. Having them in the rescaled U_{band} antenna only increases simulated model details and edges. However, due to the limited number of meshes, it is possible that two geometrical elements close to each other could be part of the same mesh. This might generate inaccurate results [184]. The statement implies that the software used to create meshes may not be able to generate enough meshes to accurately represent all the features of a complex geometry. In fact, when two different elements of the antenna are represented as a single mesh, the software assumes that they are electrically connected and that the fields in the two parts are identical. However, this assumption may not be valid if the parts have different electromagnetic properties or if the mesh does not accurately represent small features. Inaccuracies in the simulation can result in incorrect predictions of the behavior of the electromagnetic fields in the system being modeled.

To minimize such inaccuracies and prevent simulation errors to occur, it is recommended to remove unnecessary details from the model [184].

4.4.2. UB Antenna-II

While microstrip antennas can be a good choice at high frequencies, for MMW [143], 5G [185], or even Terahertz [186] applications, there present some disadvantages; in particular, for MMW frequencies [78], they exhibit low efficiency [187], especially when fed by a microstrip line. This issue is important in the present work, since it disturbs the radiation pattern at the upper band [78]. In a microstrip line, the EM waves travel along the dielectric substrate that is placed between the conductive strip and the ground plane. Ideally, all of the energy should be confined within the dielectric substrate, and no energy should be radiated outside of the microstrip line. However, in reality, some of the energy is inevitably radiated away from the microstrip line, which results in radiation loss (primarily caused by the fringing fields that extend beyond the edges of the microstrip conductors). These fringing fields create an electromagnetic wave that radiates outwards from the microstrip line, which leads to energy loss [78].

Some research has been conducted using different feed techniques in order to excite the patch in microstrip monopole antennas. For instance, to avoid this problem in 5G applications, C.-Z. Han used a CPW to feed the microstrip antenna at 28-39 GHz [188]. Also, in [189], a conductor-backed coplanar waveguide (CBCPW) or coplanar waveguide with ground (CPWG) fed microstrip antenna was reported to get high efficiency at 77 GHz. Therefore, a CPWG structure was selected, to fed the patch of the U_{band} antenna.

The physical structure of CBCPW is analogous to the addition of a CPW ground to a microstrip line, but it has distinct specifications and equations that set it apart from both. This similarity is shown in the U_{band} antenna designing steps in Fig. 4-41.

CBCPW is a type of coplanar waveguide (CPW) where the signal conductor is sandwiched between two ground planes, while microstrip line consists of a signal conductor placed on a dielectric substrate with a ground plane underneath [78]. Therefore, the CBCPW has some advantageous over a microstrip line at MMW frequencies, the most significant being less dispersion and radiation losses [190, 191].

A CBCPW line fed the radiation patch of the U_{band} antenna, UB antenna-II. Its design is shown in 4 steps in Fig. 4-41 (MMW-Ant-1 to MMW-Ant-4). The UB antenna-II is fabricated on a h = 0.5 mm thickness Rogers RO 4003C having relative dielectric constant of 3.38 and loss tangent of 0.0027. The total size of the antenna is $L_s \times W_s = 19 \times 11$ mm^2. MMW-Ant-1 has a microstrip feed line to excite the circular radiation patch with a radius of $R_p = 4.8$ mm. Its S_{11} parameter is shown in Fig. 4-42: it represents three bandwidths. The middle one has the widest bandwidth, around 62 %. MMW-Ant-2 is excited by a CPW feed line having a $W_{g1} \times L_{g1} = 4.45 \times 7.7$ mm^2 ground. The number of bandwidths decreased to two and the largest bandwidth was increased to 98 %. The CPW antenna supports the frequency range that the microstrip antenna cannot operate and vice-versa.

The microstrip and CPW structures were merged into MMW-Ant- 3 in such a way that they make a CBCPW feed line. As a result, MMW-Ant-3 has three grounds. The antenna has dual bandwidth, above and below 20 GHz. The main one is 111 %. It has the lowest minimum $S_{11} < -50$ dB at 23.3 GHz. At 11.3 GHz, the main bandwidth S_{11} is very close to the -10 dB reference line. Although it is not a problem in the simulation model but for the measurements, it can be problematic. A tiny fabrication error can separate the main bandwidth into two.

MMW-Ant-4 has two $g_1 \times g_2 = 1.7 \times 0.5$ mm^2 slots in the top grounds. As shown in Fig. 4-42, the S_{11} near 11 GHz goes lower than -11 dB. MMW-Ant-3 and -4 have the same bandwidth. The proposed CBCPW UB antenna-II has a main bandwidth from 5.67 GHz to 19.94 GHz. The calculated fractional bandwidth is 111.44 %. The UB antenna-II operates at another band above 20 GHz in the range of 22.19-26.14 GHz (FBW = 16.35 %).

Fig. 4-43 represents the surface current density at 11.3 GHz for MMW-Ant-3 and MMW-Ant-4 with the lower S_{11}. MMW-Ant-3 has an eddy surface current on the top side grounds. The gap slots on the group are placed in the center of this vortex. Two eddy currents are formed with opposite rotation directions near the gap. These results highlight a better S_{11} in MMW-Ant-4.

The other antenna parameters are: L_{g2} = 7.9 mm, L_f = 8.21 mm, and W_f = 0.7 mm. The proposed CBCPW antenna design by itself has superior performance over literature antennas. The bow tie antenna [192] boasts a maximum gain of 4 dB and an impressive bandwidth of 96%. The antipodal Vivaldi antenna [193] is also noteworthy, with a bandwidth of 90% and a maximum gain of 5.2 dB. Additionally, the leaf-shaped monopole antenna [194] offers a respectable gain of 3.05 dB and a bandwidth of 53%. The proposed CBCPW antenna here has the maximum gain of 6.1 dB at 26.1 GHz and maximum bandwidth of 111.44%.

Two of the designed U_{band} antennas were summarized in Table 4-3 with regards to bandwidth, structure, and gain.

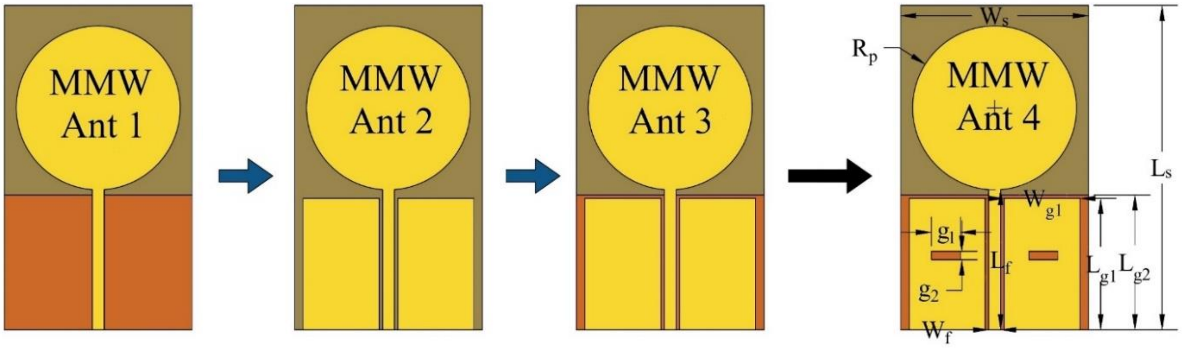

Figure 4-41 The CBCPW UB antenna-II design steps

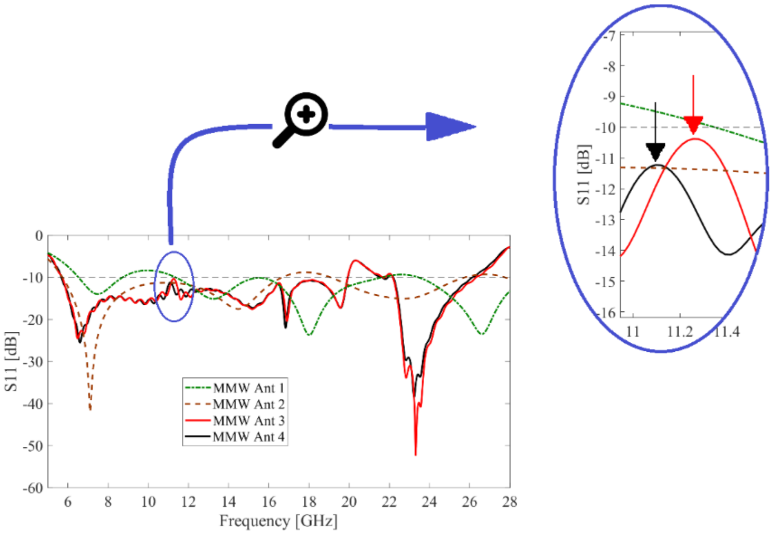

Figure 4-42 S-Parameter variation in the UB antenna-II designs

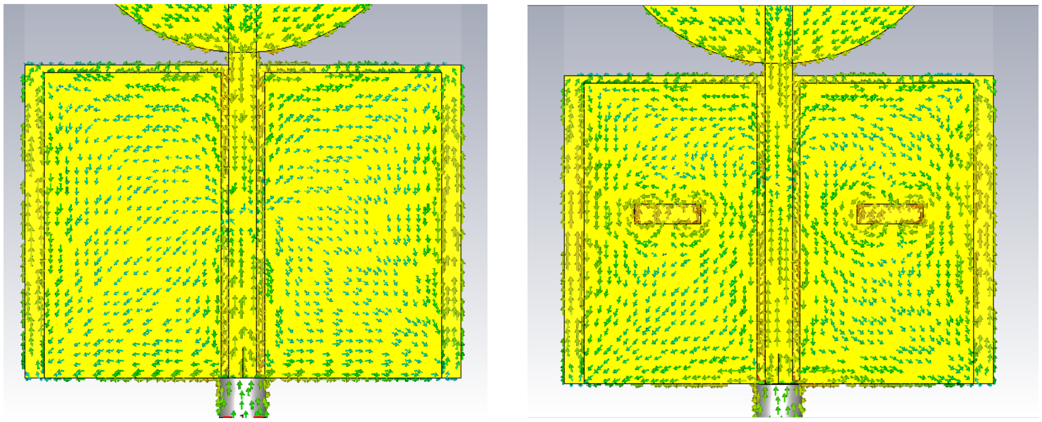

(a) (b)

Figure 4-43 Surface current of the CBCPW UB antenna-II at 11.3 GHz (a) MMW-Ant-3, and (b) MMW-Ant-4

Table 4-3 Summery of the upper band antennas

U$_{band}$ antenna name	**Structure**	**Bandwidth**	**Maximum Gain [dB]**
UB antenna-I	Rescaled LB antenna-II	7.2 – 20.4 GHz	4.54
UB antenna-II	CBCPW Monopole	5.67 – 19.94 GHz & 22.19 – 26.14 GHz	6.1

4.5 Proposed Dual-Band Antenna Integrated Reflector-I (AIR-I)

In the section 4.3, the U$_{band}$ gain was investigated in our model. The L$_{band}$ antenna is LB antenna-II with the 160 mm bent radius. The effectiveness of using this antenna as a reflector with a horn feed was also discussed. In this section, the proposed dual-band antenna integrated reflector is presented; it will be called “AIR-I” (same structure as Model IV, chapter 3). The aim is to demonstrate the approach proposed.

AIR-I is fed at the U$_{band}$ by UB antenna-I. Note that our final design will be later slightly adjusted, based on available equipment and facilities at the uOttawa microwave lab (it will be referred to as antenna integrated reflector-II, “AIR-II").

UB antenna-I was placed at the optimal feed location, determined by studying the reflector using a reference horn antenna. The sketch of the dual-band AIR-I is presented in Fig. 4-44.

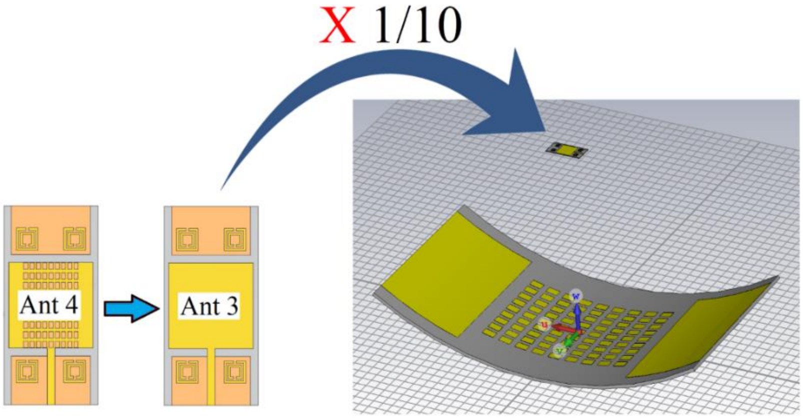

Figure 4-44 Dual-band antenna integrated reflector-I (AIR-I)

The U_{band} antenna in the proposed model has 7.2 GHz – 20 GHz bandwidth. No difference from the standalone antenna bandwidth in free space, Fig. 4-45. This is a very favorable outcome. Because the reflector reflects the radiated signal back to the feed antenna, causing a change and thus, reducing of the antenna's bandwidth [143].

The U_{band} antenna performance in free space (UB antenna-I) is shown in Fig. 4-45 and Fig. 4-46. The antenna has an omnidirectional pattern with a maximum gain of 4.6 dB at 16.6 GHz. After implanting our model, the U_{band} gain jumps up significantly. The maximum gain was enhanced by more than 10 dB and goes to 15.15 dB at 19.6 GHz.

The L_{band} antenna exhibited favorable results and has the same S_{11} and gain in free space as the proposed design, Fig. 4-47.

The AIR-I has $FR = {}^{13.6}\!/_{1.35} = 10.1$, maximum U_{band} gain of ~15.2 dB and L_{band} gain of 5.6 dB. It has a 86% bandwidth in L_{band} and 94% in U_{band}.

It fulfilled all the objectives stated in chapter one, including gain improvement, a FR of at least 8 is targeted while keeping wideband capabilities. Some existing designs focused on gain improvements [195] by utilizing an I-shaped resonator (ISR), reporting a maximum gain improvement of 3.3 dB. Similarly, in [196], H-shaped resonator elements were used along with metamaterials to improve a vertical planar antenna, resulting in a gain improvement of 3.4 dB. In [197], a partially grounded printed monopole antenna loaded with a split ring resonator was able to achieve a gain improvement of 4.3 dB through the use of a metallic reflector. Additionally, a frequency selective surface (FSS) reflector in [198] improved the slotted ground antenna by 4 dB.

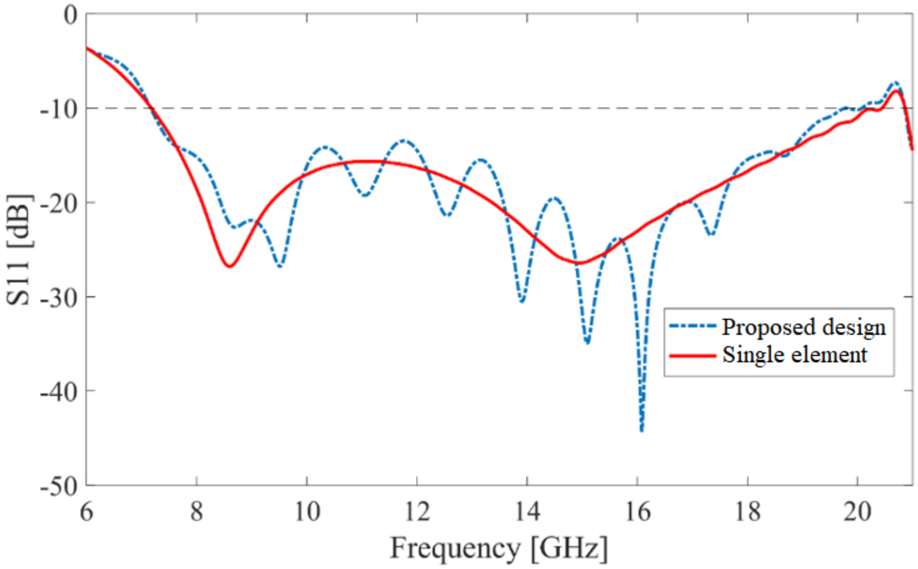

Figure 4-45 U_{band} antenna bandwidth, single element and the proposed design

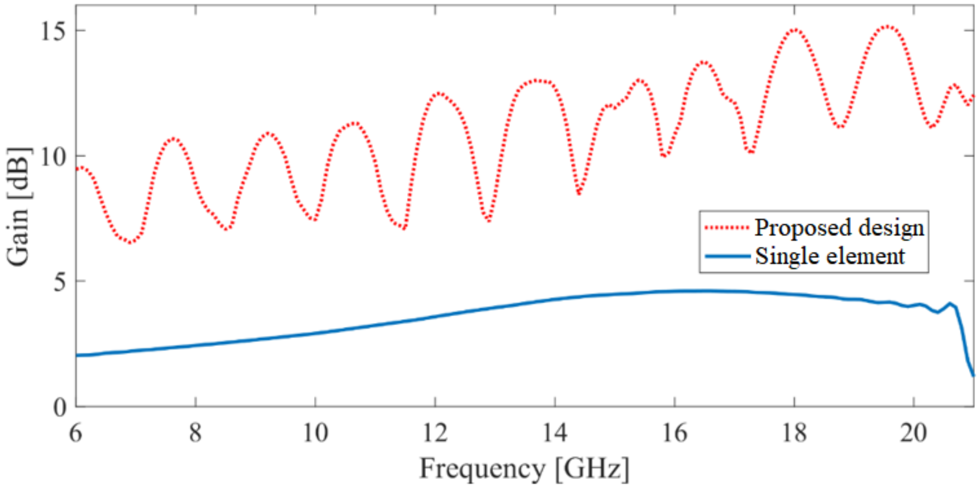

Figure 4-46 U_{band} antenna gain, standalone antenna and proposed design.

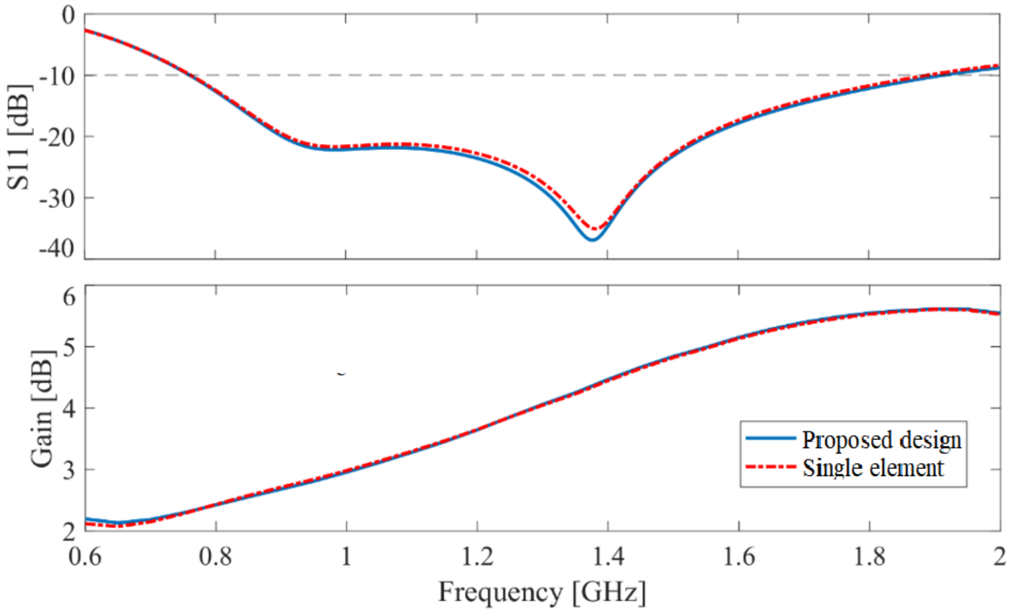

Figure 4-47 L_{band} antenna bandwidth and gain, single element and the proposed design

4.6 Proposed Dual-Band Antenna Integrated Reflector-II (AIR-II)

The AIR-I showed that our proposed method works correctly. The U_{band} antenna gain was improved significantly. It made the final U_{band} antenna more directive, without having any adverse impact on the antenna bandwidth. At the same time, the L_{band} antenna has its own performance like before.

The AIR-I antenna, Fig. 4-44, has a central frequency of approximately 13.5 GHz for its U_{band}. However, our antenna lab is capable of measuring up to 20 GHz. To demonstrate the model's ability in the 5G band and to measure the antenna as a proof of concept, AIR-II was designed with a special design compared to the first one. This antenna features a dual-band upper antenna, UB antenna-II, with one bandwidth below 20 GHz and another band above 20 GHz. AIR-II has the same bandwidth as AIR-I in the L_{band}, which ranges from approximately 0.75 to 1.9 GHz.

So, AIR-II, Fig. 4-50, was studied as a dual-band antenna with a large FR for 5G applications, utilizing its L_{band} at 1.3 GHz and the U_{band} operating above 20 GHz at 24.5 GHz. On the other side, as a proof of concept, AIR-II was fabricated and measured as a dual-band antenna with its L_{band} at 1.3 GHz and the U_{band} operating below 20 GHz, specifically at 12.8 GHz, in order to use our facilities.

Subsequently, the antenna was positioned in the proposed design with the same orientation as the rescaled U_{band} antenna depicted in Fig. 4-44. Both L_{band} and U_{band} antennas are excited from the $-u$ direction.

The gain at the U_{band} is dependent on the U_{band} antenna main lobe direction. In the ideal situation, it should be situated precisely at the center of the reflector [35], as demonstrated in Fig. 4-34. However, because of operating in a very wide range of frequencies, > 20 GHz, different modes are excited inside the patch antenna [78]. As a result, the radiation pattern changes at each mode. The antenna has a monopole structure and an omnidirectional radiation pattern at most frequencies. Rotating the feed antenna enables the identification of an optimized one with the highest average gain.

U_{band} CBCPW antenna was rotated in the $w-u$ plane counter clockwise. The effect of this orientation on the antenna bandwidth is shown on the S_{11} parameter in Fig. 4-48. At 11.1 GHz, two orientations at 0° and 45° have a S_{11} slightly higher than -10 dB, close to -9 dB. The U_{band} antenna has the same bandwidth. Rotating the antenna in $w-u$ plane, Fig. 4-50 (a), does not change operational frequencies. Unlike bandwidth, this rotation has a significant impact on the antenna gain, Fig. 4-49.

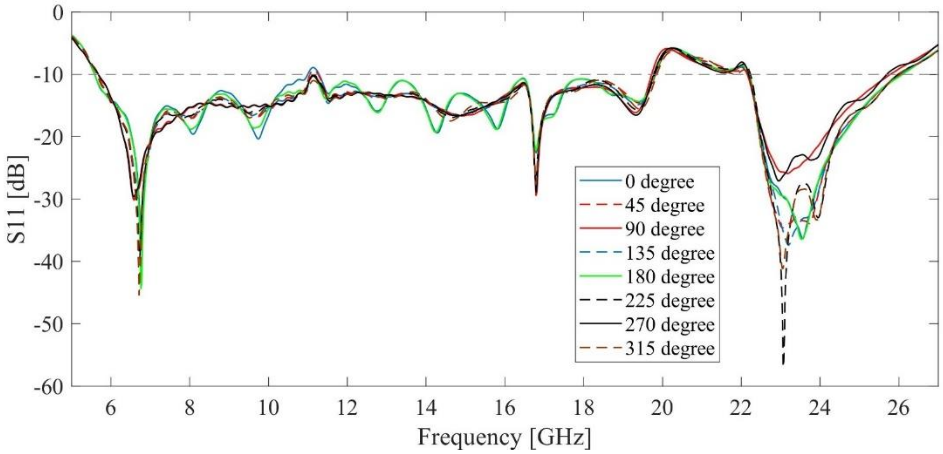

Figure 4-48 S-Parameter for U_{band} antenna at different orientations in $w-u$ plane

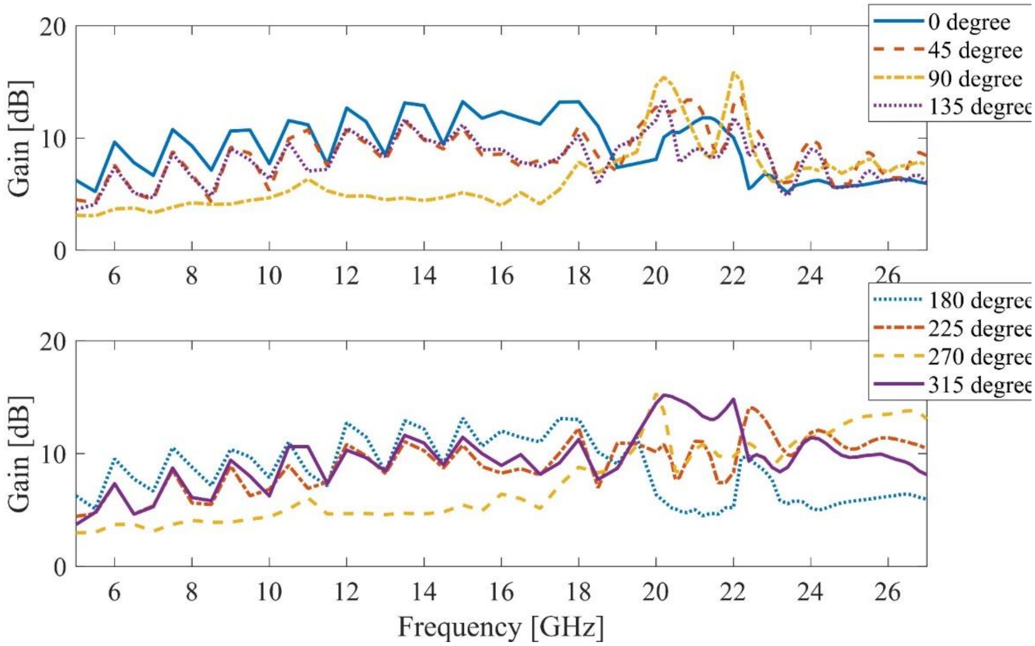

Figure 4-49 Maximum gain of U$_{\text{band}}$ antenna at different orientations in $w - u$ plane

At 270 degrees, on the upper side of the operating frequency range, the antenna has the highest gain in the operational bandwidth (15.3 dB), but on the other side, it has the lowest gain around 3 dB. The focus is to obtain a relatively high average gain with low fluctuation. In this case, at 0 and 180 degrees, the antenna has desired gain with a maximum amount of ~ 13 dB and a minimum of > 5 dB in the first bandwidth. But on the second U$_{\text{band}}$ bandwidth, > 20 GHz, these two orientations have a low gain at 25 GHz, < 5 dB, compared to others.

The low gain of the antenna above 20 GHz is not desired. For finding out a better orientation, let us look at the antenna structure. The U$_{\text{band}}$ CBCPW antenna has a monopole structure [199]. When considering the radiation pattern, a comparison can be made with a monopole wire antenna [200] for the purpose of simplifying the problem. The three antenna grounds are similar to the monopole ground and the circular radiation patch is like a monopole antenna. Therefore, it is expected to have an omnidirectional radiation pattern at most frequencies [201]. The doughnut-shaped radiation pattern has an axis along the length of the antenna. So, the U$_{\text{band}}$ antenna should be rotated 90˚in $u - v$ plane. With that, the cylindrical reflector can receive most of the radiated power along its length and reflects them in a more directive pattern. The proposed U$_{\text{band}}$ feed antenna was rotated by 90 ˚ as shown in Fig. 4-50 (b). To find an optimized orientation, the U$_{\text{band}}$ antenna was rotated in $w - v$ plane counter clockwise as displayed in Fig. 4-50 (c).

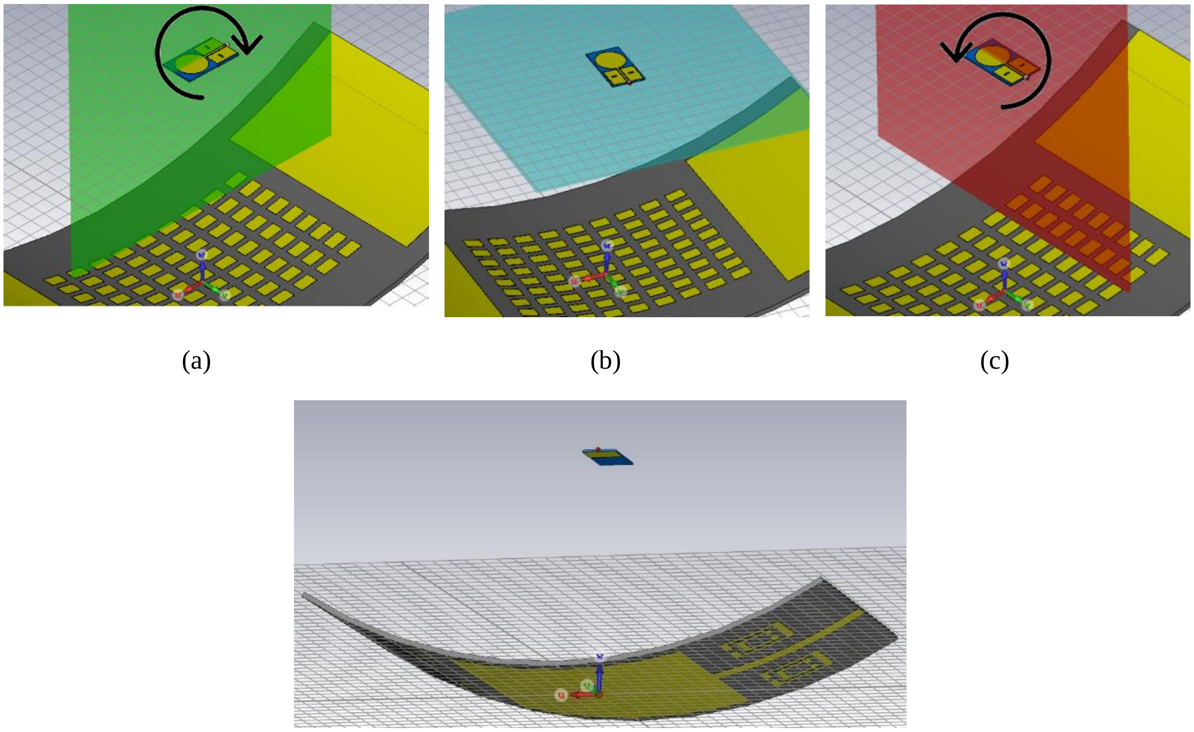

(a) (b) (c)

(d)

Figure 4-50 3D sketch of the proposed Dual-Band AIR-II, (a) top view rotating in $w-u$ plane, (b) rotated 90 degrees in $u-v$ plane, (c) rotating in $w-v$ plane, and (d) bottom view.

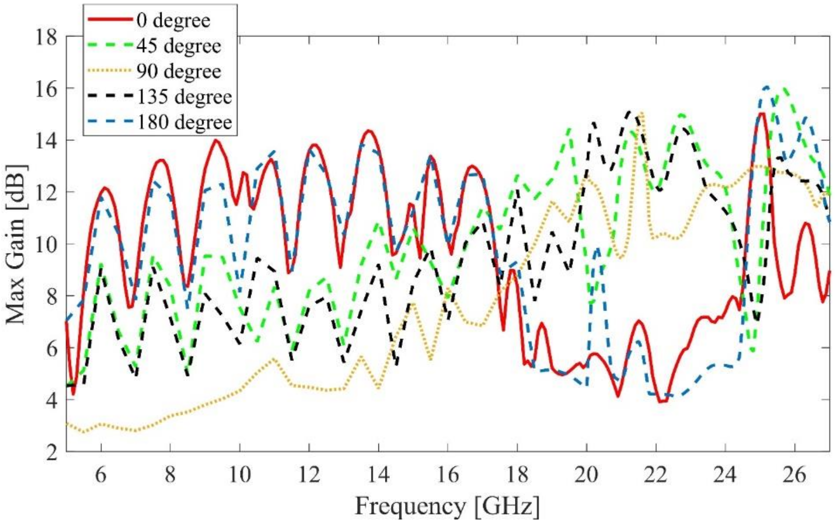

Figure 4-51 Maximum gain of U_{band} antenna at different orientations in $w-v$ plane

Alongside this plane, the U_{band} antenna gain is higher than the previous, Fig 4-49 vs Fig. 4-51. Significant gain improvement is observed at 25 GHz, which is a result of the reflectarray element resonances. The maximum gain is located at this frequency with a value of 16.1 dB for the 180°

rotated one. The gain increases significantly from 5.6 dB for the single antenna to 16.1 dB at 25 GHz when it is mounted on the proposed model.

The gain of a patch antenna operating at the same frequency was calculated using numerical methods in MATLAB, and the results show an increase from 10.1 dB to 18.4 dB. In Chapter 3, the calculated gain using a dipole antenna for the U_{band} and a parabolic shaped for the Lband, was increased to 23 dBi.

The calculated gain has the highest value because it assumes a perfect antenna without any losses, such as dielectric loss, conductor loss, or mismatch. In numerical methods, the mismatch is taken into account, but the conductor and dielectric losses are not considered, which gives a gain lower than the calculated one but closer to the simulated one. Finally, in the simulations, all of the mentioned losses are taken into account, and as a result, the gain is expected to be lower than the numerical methods.

Table 4-4 presents a summary of the proposed dual-band antenna with a large FR in this thesis. The AIR-II has the maximum FR of 18, which is higher than all of the dual band antennas studied here in the literature. The antenna has a wide bandwidth of 86% in the 5G FR1 frequency bands in its L_{band}. In the U_{band}, there are two bandwidths, one of which has a 16.4% bandwidth in the 5G FR2 frequency band. The AIR-II's bandwidth is well-suited for 5G wireless applications, with one bandwidth in FR1 and another in FR2.

The next chapter will present a comparison between these simulations and measurements.

Table 4-4 Summery of the proposed antenna integrated reflectors

Proposed Dual-Band Antenna Integrated Reflector	Lower Bandwidth [GHz]	Upper Bandwidth [GHz]	Lower Band Antenna	Upper Band Antenna	FR
AIR-I	0.77 – 1.925	7.2 – 20	LB Antenna-II	Rescaled LB Antenna-II	10.1
AIR-II	0.77 – 1.925	5.67 – 19.94 & 22.19 – 26.14	LB Antenna-II	CBCPW	9.5 & 18

The study of performance is limited to 20 GHz as the University of Ottawa antenna microwave lab, equipped with an Anritsu 37347A vector network analyzer capable of measuring only up to 20 GHz [202].

The 0-degree rotated antenna has the second highest gain at 25 GHz (15 dB). In the first bandwidth, < 20 GHz, the 0-degree has a higher gain than 180˚ with fewer fluctuations. At 10 GHz the gain at 0˚ is more than 3.5 dB higher than the 180˚. At 13.7 GHz the antenna gain reaches 14.4 dB (red graph). Therefore, despite having the highest maximum gain at 180˚, the 0˚ rotated one is chosen. Also because of some measurement limitations in our antenna lab.

The CBCPW antenna was placed as an U_{band} feed, same as the one shown in Fig. 4-50. Changing bandwidth and using an antenna without a stable main lobe can change this optimal point, so in Fig. 4-52, the F_h parameter was studied again with a 5 mm step width. Approaching the antenna to the reflector would increase the gain, because of the omnidirectional radiation pattern. The value F_h = 77 mm (F_h = 6.4 λ) gives the highest gain, The achieved distance in this study is very close to the distance of approximately 6 λ in spoof surface plasmon polariton (SSPP) reflectarray antenna by P. Jiang [180]. It is recommended to maintain a minimum F_h of 77 mm to preserve antenna bandwidth, as reducing the F_h below this threshold will result in a decrease in bandwidth.

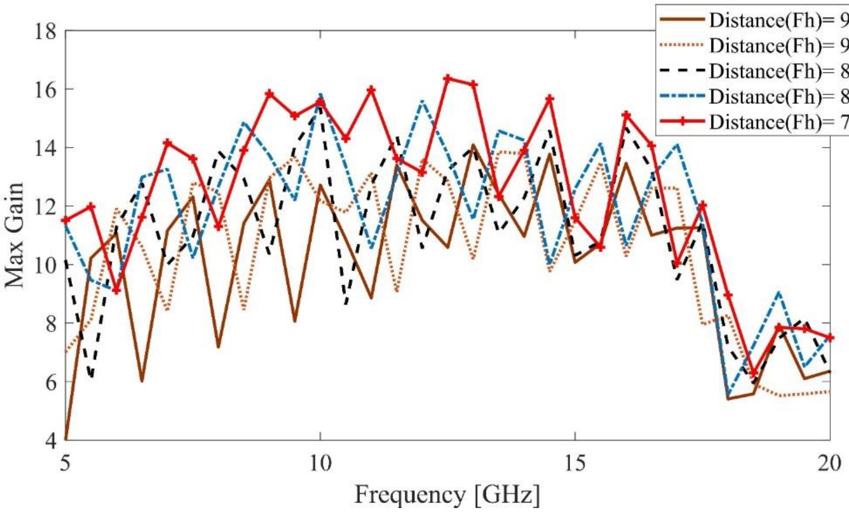

Figure 4-52 Parametrical study of F_h up to 20 GHz frequency

Before the fabrication step, the final model was simulated with a maximum number of meshes that our system is capable of handling (to assure a good accuracy). The whole model created ~ 60 million mesh cells in CST microwave studio 2022. An AMD Ryzen Threadripper 2990WX 64-core logical processor with 128 GB RAM computer was used. The results are highly consistent with previous findings, indicating the absence of simulation errors resulting from inadequate mesh quantities.

The accuracy of simulation results in the CST Microwave Studio software relies on the mesh size of the cells used to discretize the simulated structure's geometry. The mesh size refers to the size of the individual cells or elements that comprise the mesh [177].

In general, using a finer mesh with smaller cell sizes can produce more accurate results. This is because it allows for a more detailed representation of the geometry and a more precise modeling of the electromagnetic fields, especially for structures with fine details or high-frequency structures.

In simulating electromagnetic structures, it is crucial to ensure that the mesh size is small enough to capture the wavelength of the electromagnetic waves accurately. This is because the mesh's ability to represent the electromagnetic field behavior affects the simulation results' accuracy.

Hence, using high mesh cells for a similar model in CST Microwave Studio software can lead to more accurate results due to the more detailed geometry representation and precise modeling of the electromagnetic fields. However, it is essential to balance the results' accuracy with the required computational resources, as a finer mesh can increase the simulation time and computational requirements. The subsequent chapter will feature a comparison between these simulated results and measurement data.

4.7 Conclusion

This chapter details the implementation of the design method in order to fabricate the final dual-band antenna. To attain the stated objective, the design process commenced by creating a L_{band} antenna with a half-ground configuration. The specifications of this antenna were established in Chapter 3. To create the L_{band} antenna with the necessary bending, a study was conducted on the performance of the antenna in various bending positions. The negative full bending position, LB antenna-I, was selected. The reflectivity of LB antenna-I was then improved to enhance antenna gain when functioning as a reflector in the U_{band}, resulting in LB antenna-II. A bending radius of 160 mm was identified as having the least impact on the performance of LB antenna-II, and thus was selected.

The subsequent experimental procedure involved utilizing a reference horn antenna at the U_{band} to examine the reflector's efficacy and determine the suitable feeding distance. Upon determining the adequate parameter values for the LB antenna-II, such as curvature radius and feed location, the next step was to start the design of the final antenna.

The novel dual-band AIR-I was introduced, which exhibits a distinct structural composition, wherein the U_{band} antenna is proportionally resized to that of the L_{band} one. Notably, the implementation of the theorem of similitude has enabled the proposed AIR-I to attain a FB of 10.

The final model was presented and named dual-band antenna integrated reflector-II (AIR-II). The antenna was designed utilizing the available substrate and laboratory resources. Notably, due to the presence of higher order mode excitation in the U_{band} antenna, the main beam direction of the feed antenna was found to be unstable while being directed towards the reflector. To determine the most adequate orientation of the U_{band} antenna, a study was conducted wherein the antenna was rotated in its feed location.

In conclusion, AIR-II was successfully improved for operation below 20 GHz, and underwent subsequent fabrication and measurement, as discussed in the forthcoming chapter.

Chapter 5 – Fabrication and Measurement

This chapter deals with fabricating the prototype, measuring its performance, and validating the proposed approach.

To ensure a robust proof of concept, two prototypes were manufactured. They have a similar structure, albeit with some minor differences, and were designated as Prototype-I and Prototype-II.

Prototype-I, referred to as AIR-II, was optimized in Chapter 4 for frequencies under 20 GHz. Prototype-II is similar to Prototype-I, but it features a different U_{band} antenna to further validate the proposed concept. Note that its U_{band} antenna still meets the claimed requirements and has a monopole structure. Due to the potential disadvantages of microstrip antennas in high frequency mentioned in the previous chapter, the radiation patch is fed by a CPW feed line.

The U_{band} for prototype-II was designed on a flexible substrate to enable printing with screen printing technology. This thesis work was supported by The National Research Council Canada (NRC) for their organic material project, so it is worth mentioning that the flexibility of the antenna was a requirement for the NRC project.

Finally, the two prototypes were measured in an antenna chamber, and both of them satisfied the requirements for large FR dual-band antennas. A comparison between simulations and measurements was done and showed a good agreement with each other.

5.1 Prototype-I

5.1.1 LB Antenna-II

The fabrication and measurements of LB antenna-I demonstrated the reliability of the Cricut accuracy in producing L_{band} antennas. The 3D printed PLA structure was utilized to create an antenna holder and shape the reflector with the appropriate curvature.

We therefore used the Cricut Maker machine via fine-point blade to fabricate the LB antenna-II on a PF-4 1.6 mm thickness substrate having a dielectric constant of 1.06 and loss tangent of 0.001, Fig 5-1. The copper foil was stuck on its top side to the Maker pad. The copper parts were cut out of this foil. Next, the extra parts were removed. After removing the white cover from the copper cut sections, we stuck the copper to the PF-4 substrate, Fig. 5-2.

A 40 MHz - 20 GHz Anritsu 37347A vector network analyzer was used to measure the antenna return loss [203]. The antenna was suspended from its input port during testing to maintain a flat position and to prevent the influence of body tissues on the test results, as illustrated in Fig. 5-3. The measured LB antenna-II, in a flat configuration, exhibits a bandwidth of 0.74 GHz to 2.1 GHz with a minimum return loss of -40 dB, Fig. 5-4.

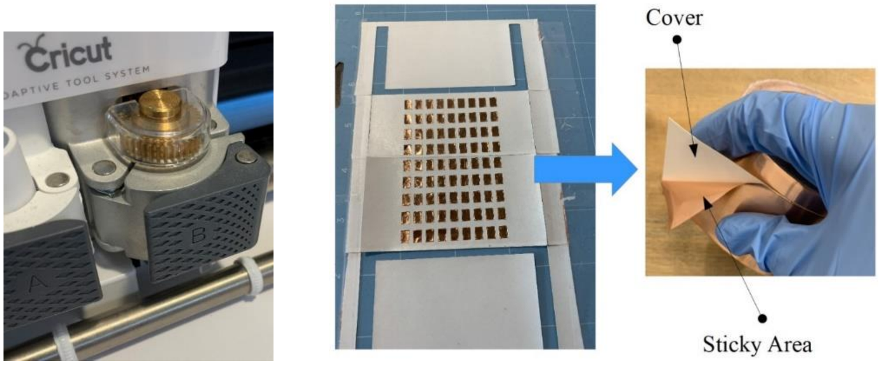

(a) (b)

Figure 5-1 LB antenna-II fabrication process via Cricut, (a) Cricut machine, and (b) cut copper section

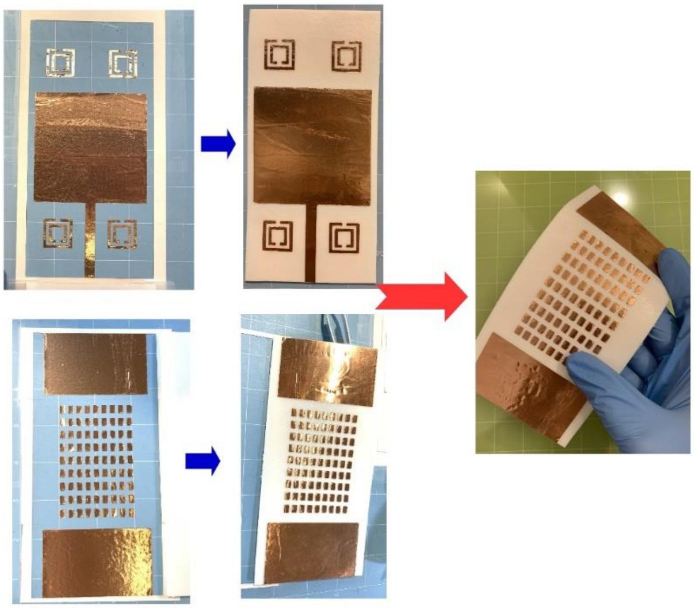

Figure 5-2 Flexible LB antenna-II fabrication process and the prototype

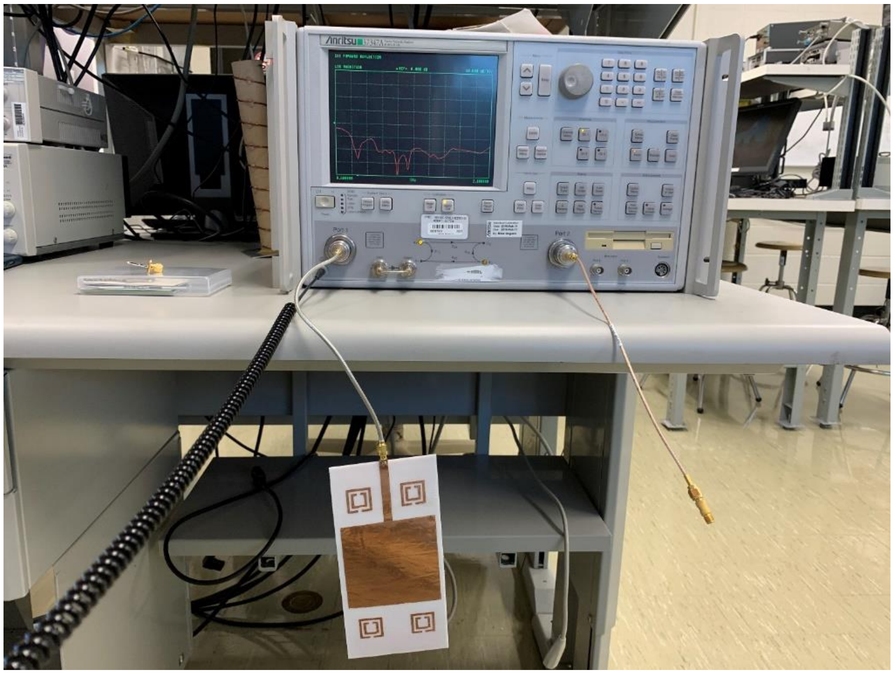

Figure 5-3 LB antenna-II measurement setup in a flat situation

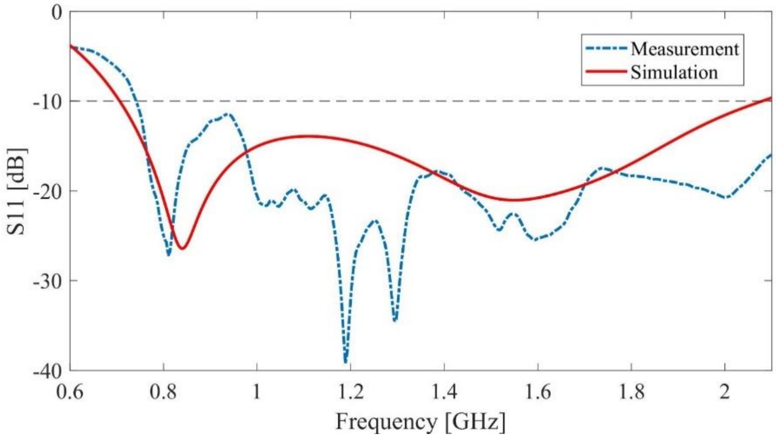

Figure 5-4 Measured LB antenna-II bandwidth in a flat situation

LB antenna-II was formed into a cylindrical shape with the desired radius of 160 mm. The 3D-printed PLA holder kept the antenna in an accurate curvature during the tests. The next step was to design the UB antenna and build the prototype-I.

5.1.2 CBCPW Antenna Prototype

The prototype of the MMW CBCPW antenna, which was introduced in chapter 4, Fig. 4-41, has been printed on 0.5 mm Rogers RO 4003C with $\varepsilon_r = 3.38$ and loss tangent = 0.0027. This antenna is the U_{band} antenna in prototype-I. A male SMA connector is attached to the antenna, as depicted in Fig. 5-5.

Figure 5-5 CBCPW MMW antenna prototype for U_{band} (a) top view, and (b) bottom view

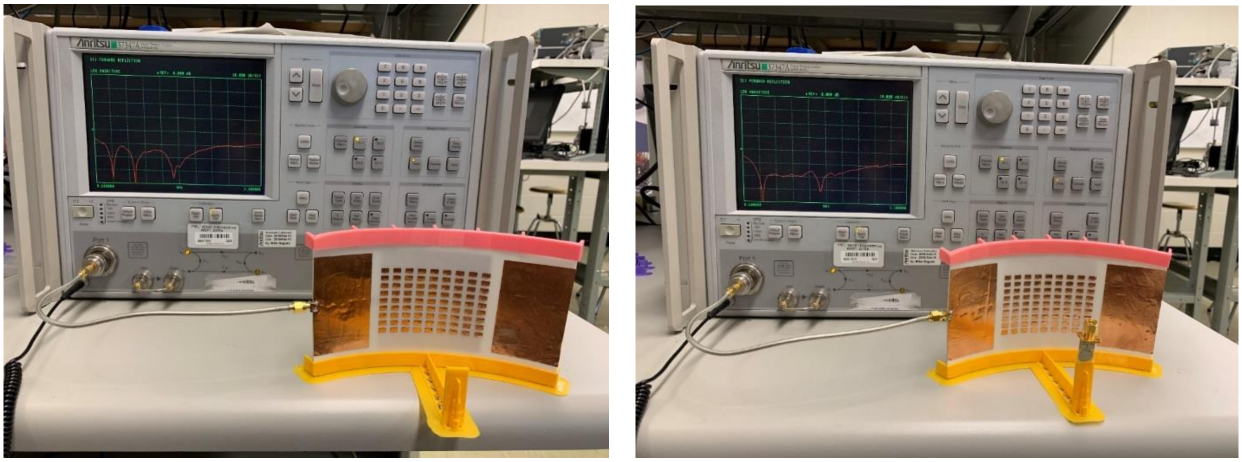

Figure 5-6 160 mm radius curved LB antenna-II bandwidth measurements, (a) without U_{band} antenna (b) with U_{band} antenna

The LB antenna-II, formed into the desired shape and placed in our model, is shown in Fig. 5-6. Referring to Fig. 5-7, it can be observed that the L_{band} S_{11} of prototype-I (i.e., with the LB antenna-II and the UB antenna CBPW) remains unchanged in both the presence and absence of the U_{band}

antenna. In the measurement, one resonant frequency was lost in the presence of the U_{band} antenna. However, the bandwidth remained consistent, which is an important result for our design.

The slight difference observed between the measurements and simulation in the S_{11} graph, along with the appearance of some resonant frequencies, can be attributed to the effect of the PLA holder near the antenna. This effect was not taken into account in the simulations, because its dielectric constant changes at each frequency. PLA has a dielectric structure with a dielectric constant, approximately 2.72, and a loss tangent of 0.008 (at 2.4 GHz) [204]. This dielectric, located near the antenna, can act as a dielectric resonator (DR), similar to a DR antenna. It can alter the S_{11} and add a resonant frequency [205].

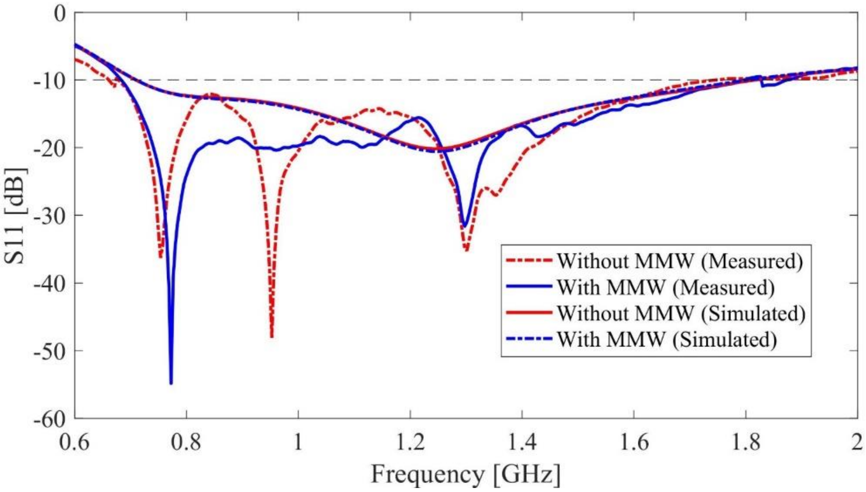

Figure 5-7 Curved LB antenna-II measured S_{11}, With/without U_{band} antenna

5.2 Prototype-II

5.2.1. MMW PET Antenna Prototype

A MMW PET antenna was fabricated for use as a U_{band} antenna in Prototype-II, which is a second proof of concept for the proposed antenna, AIR-II. The antenna patch is fed by a CPW line, similar to the one described in [206].

CPW is a transmission line structure that is relatively easy to fabricate using standard lithography and screen-printing techniques. Given that our screen-printing facility excels in fabricating single-layer circuits, CPW is a more feasible option as compared to CBCPW. Additionally, CPW can offer a higher quality factor, which results in lower signal loss and higher efficiency [78].

The antenna was designed on a 0.125 mm thickness transparent PET substrate of dielectric constant = 3.2 and loss tangent = 0.08. The antenna has a compact size of 20 × 11 mm^2. At NRC

Advanced Electronics and Photonics Research Centre (AEP) in Ottawa, screen printing technology was used for fabrication, providing a good level of accuracy for single layer circuits due to its low misalignment error. In fact, a CPW transmission line has only one-layer conductive part, so it is an appropriate structure in the MMW range. The circular radiation patch of the monopole MMW antenna was fed by a CPW line. The CPW MMW antenna structure and prototype are shown in Fig. 5-8.

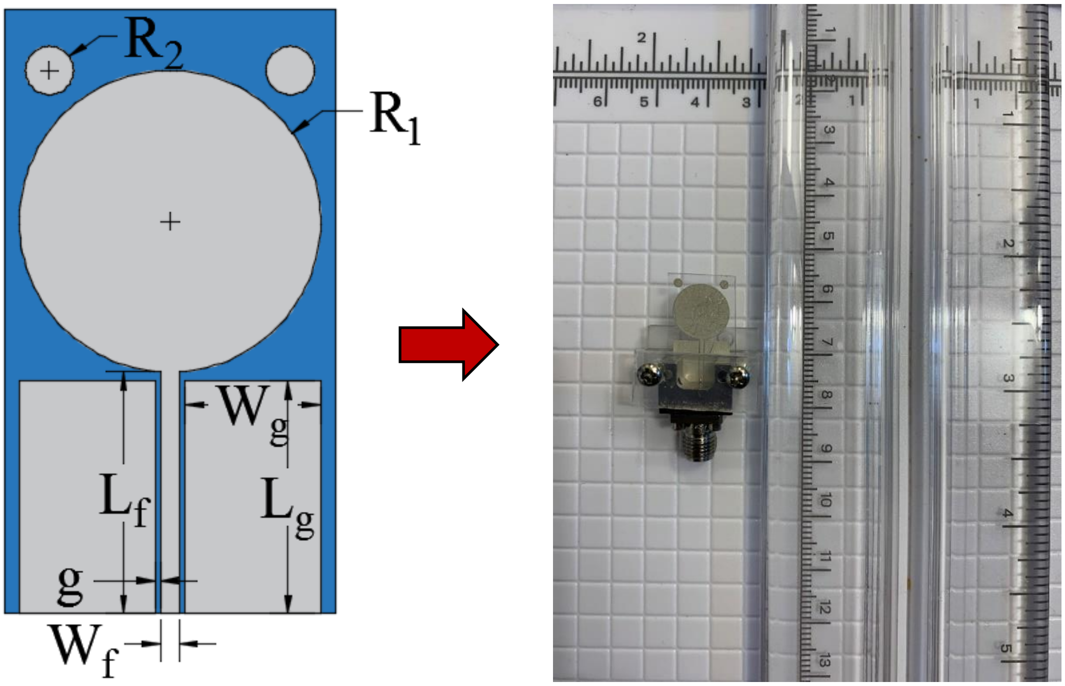

(a) (b)

Figure 5-8 Geometry of the U_{namd} CPW antenna on PET substrate, (a) schematic view, and (b) prototype picture

The CPW antenna will be used as the U_{band} antenna in prototype-II. Additionally, it is important to note that the gap of the CPW feed line was set to 0.2 mm, which is equal to our lowest screen printing accuracy. The CPW antenna parameters are W_f = 0.61 mm, L_f = 8.01 mm, W_g = 4.5 mm, L_g = 7.7 mm, R_1 = 5 mm, and R_2 = 1.6 mm.

The antenna was printed via conductive ink on the PET organic substrate as shown in Fig. 5-9. The other antennas on the substrate are not related to our study and are part of the NRC project.

Note that, as a result of using conductive ink and a low melting point of PET, the SMA connector cannot be soldered to the antenna. To eliminate the need for soldering, a non-soldering SMA connector was used.

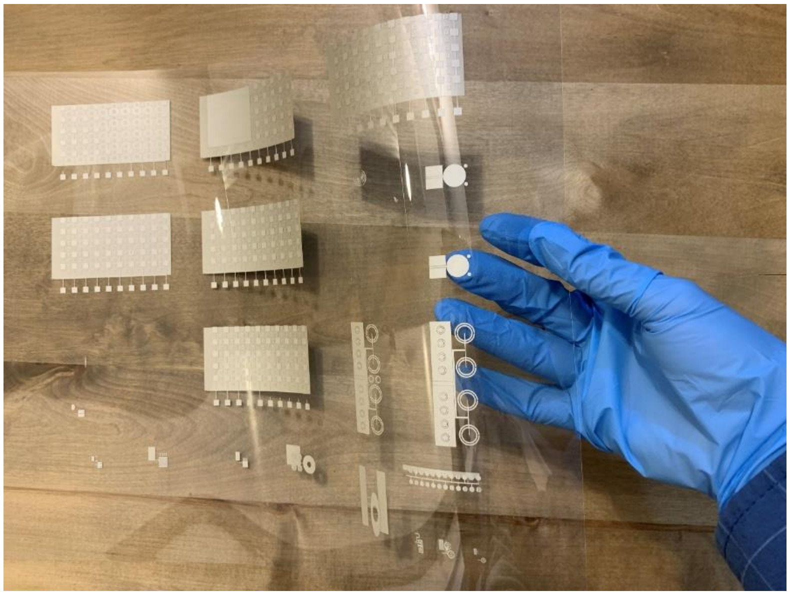

Figure 5-9 Screen printed antennas on transparent PET substrate via conductive ink

Fig. 5-10 shows the two fabricated prototype MMW antennas under the microscope. The accuracy of screen printing technology is lower compared to that of milling machines. This difference in fabrication accuracy is evident when comparing the two methods. For example, the screen-printed antenna has a wobbly edge, while the PCB antenna has a sharp one.

The antenna CPW line is very sensitive to the gap width which is presented in Fig. 5-10 (b). The wobbly edge of the CPW line causes an increase in line loss at higher frequencies. This is another reason why the operational frequency for measurements was chosen to be under 20 GHz.

5.3 Proposed Antenna Integrated Reflector Prototype Sketch

A 3D view of the antenna integrated reflector with a holder is shown in Fig. 5-11. The two reflector shapers bent the L_{band} as a cylindrical reflector with a 160 mm radius. Because of the flexible foam structure of the LB antenna-II, back holders were added to keep the antenna physically sturdy. A small gap of ~10 mm was introduced between the back holder and the antenna to prevent physical contact between the metal and the antenna. This helps reducing the resonant effect of the PLA dielectric on the L-band antenna's performance. This effect is similar to that used to radiate in DR antenna.

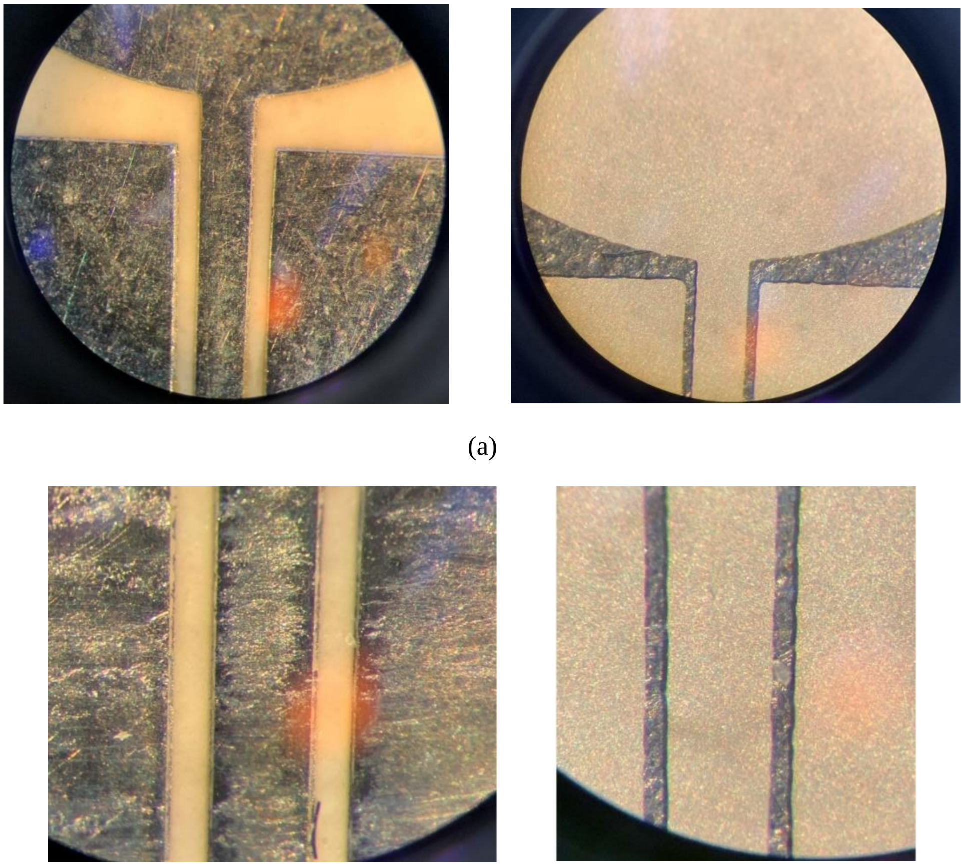

(a)

(b)

Figure 5-10 The MMW prototype antennas under a microscope left milling machined CBCPW, right screen printed CPW; (a) Feed line – patch connection, and (b) transmission line

10 mm spacers were added to reduce the effect of the 3D printed back holder on the RF antenna, especially to avoid shifting frequency (Because it can act like a dielectric resonator element or disturb the Quasi-TEM mode of the input signal in the microstrip feed line) [205].

A 3D printed structure was used to make the MMW feed holder. Additionally, it was used to shape the LB antenna-II as a cylindrical reflector with a 160 mm radius. Our 3D printer has an accuracy of approximately 0.3 mm, which is equivalent to around 1% of the wavelength at the central frequency of the CBCPW antenna. This level of precision should be sufficient to determine the location of the feed.

To avoid setting the feed point manually a 0.5 mm × 1.5 mm slot was created on the feed holder. The CBCPW MMW antenna was then inserted in this slot. The design of the MMW antenna holder was inspired by the NASA 70-meter dish model [207]. The 3D model is licensed free for educational and research purposes. The antenna body part was printed with PLA material. An Ultimaker $^{2+}$ 3D printer at the niversity of Ottawa MakerSpace was used to print the structure, Fig. 5-12.

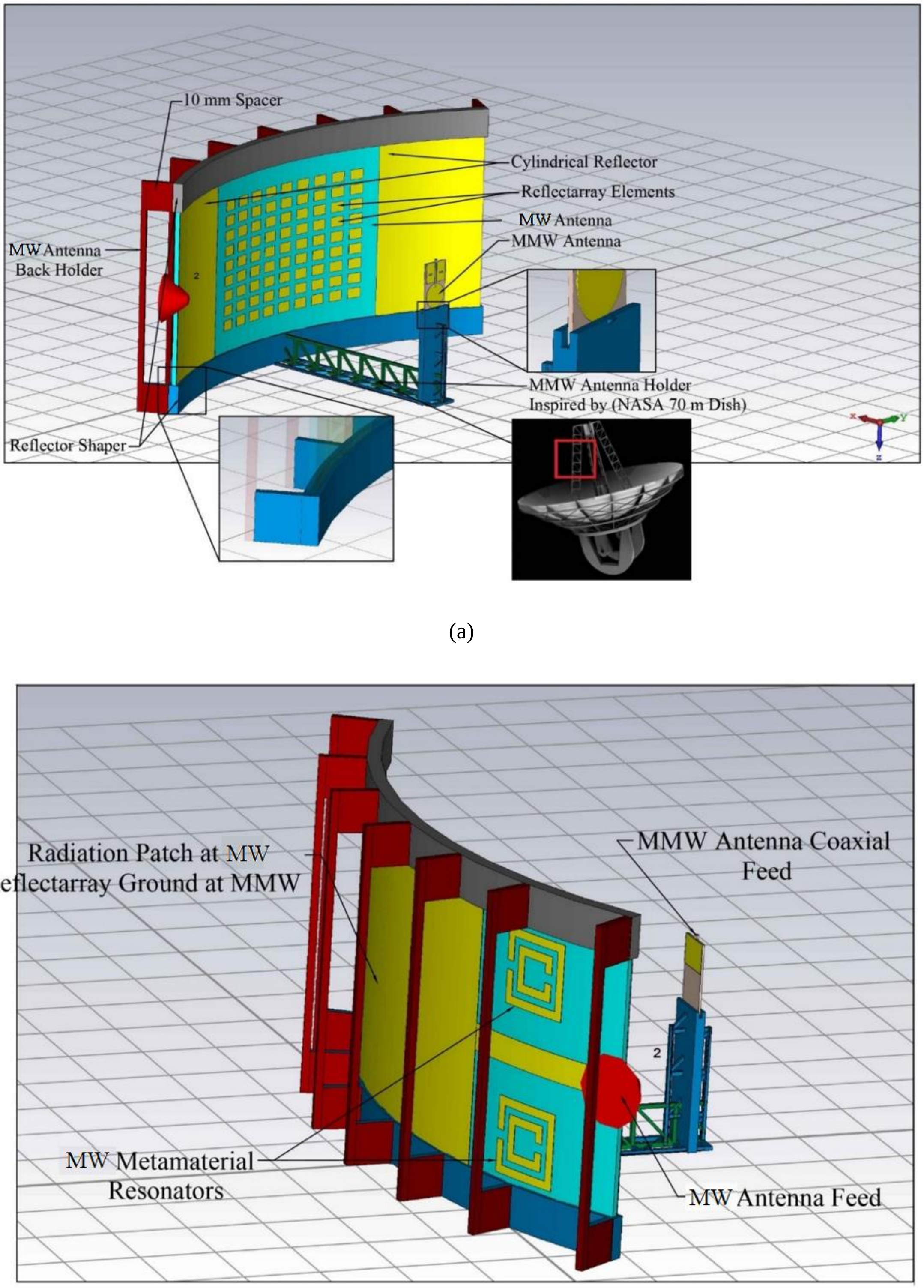

(a)

(b)

Figure 5-11 3D sketch of the proposed dual-band antenna integrated reflector with 3D printed holder; millimeter-wave (MMW) antenna refers to U_{band} antenna and microwave (MW) one refers to L_{band} one , (a) front view, and (b) back view

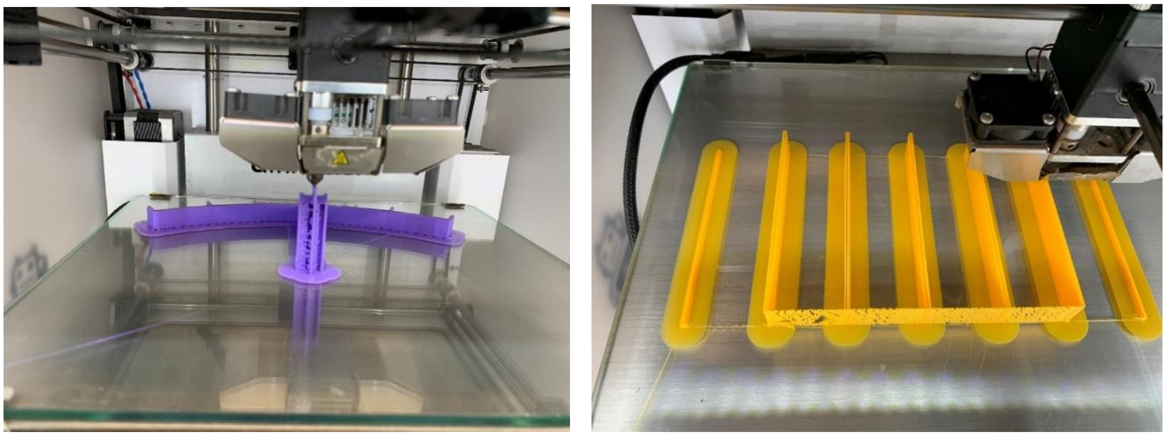

Figure 5-12 3D printing the antenna integrated reflector holder at uOttawa

Two proposed antenna integrated reflectors, which structure is shown in Fig. 5-11, were fabricated as prototypes I and II. The only difference between the two prototypes is their upper band antennas.

Prototype-I has the exact same structure as AIR-II, the LB antenna-II is used for the L_{band} and the CBCPW MMW antenna for U_{band}.

Prototype-II also has LB antenna-II for the L_{band}, but the PET CPW antenna was selected for the U_{band}.

5.4 Prototype-I Bandwidth Measurements

The prototype-I, Fig. 5-13, was tested up to 18 GHz, according to the measurement facilities. To eliminate long cable loss between the VNA and the antenna chamber, as well as to reduce measurement errors, the antenna was connected to the VNA using the shortest possible cable and measurements were taken outside the antenna chamber.

The prototype-I U_{band} S_{11} is presented in Fig. 5-14. A strong agreement can be observed between the measured and simulated bandwidths, which both cover the range of 6 GHz to 18 GHz. Furthermore, the measured BW is 100%, indicating a broad frequency range.

The simulation results for the U_{band} antenna (CBCPW) in both free space and within our AIR-II structure show no reduction in bandwidth. Additionally, the measurement results for the CBCPW antenna's bandwidth were found to be very close to the black dotted graph, rendering it unnecessary to plot. Note that the bandwidth of the CBCPW antenna outside our model is not considered to be highly significant for our purposes.

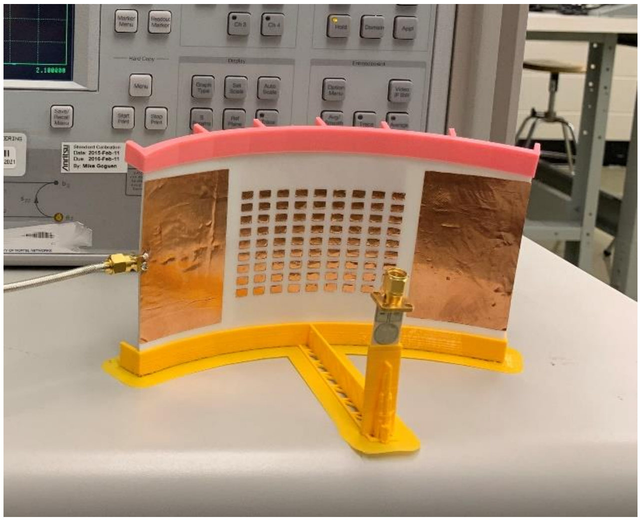

Figure 5-13 Prototype-I undergoing S-parameter measurements

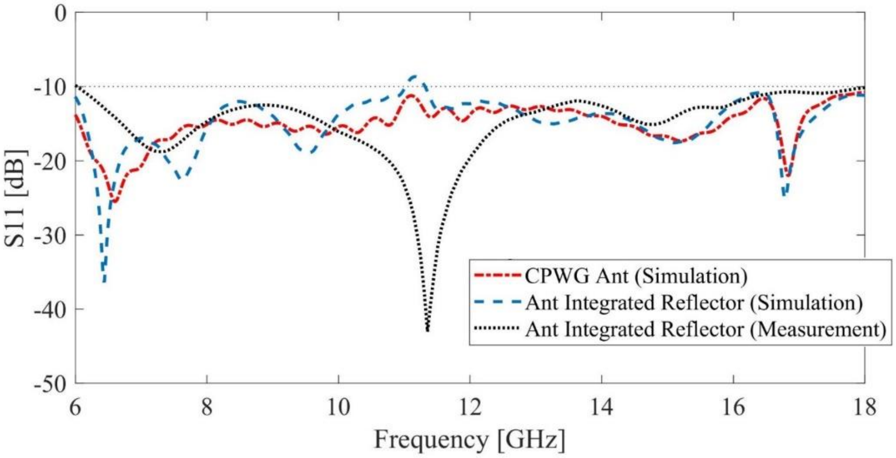

Figure 5-14 Measured S_{11} of the prototype-I U_{band}

5.5 Prototype-I Fairfield Measurements – Antenna Chamber

The schematic view of the antenna under test (AUT) gain measurement is shown in Fig. 5-15. The gain measurement is done in two steps. Initially, the Tx antenna is positioned. This antenna operates within the desired frequency range and has a linear polarization. Its gain is unknown, but as long as it has sufficient bandwidth at the test frequency, it does not impact the measurements. The Tx antenna is fixed in position and serves as the transmitter antenna, pointing towards the opposite side.

The network analyzer's first port is linked to an amplifier that enhances the VNA's output signal to compensate for any losses in the lines or connections. This increase in the transmitter signal results in a better signal-to-noise ratio, which ultimately leads to more accurate results. The second port of the network analyzer is linked to the receiver antenna located on the opposite side, which is rotated using a positioning system. This rotation allows for the measurement of the receiver antenna's two-dimensional radiation pattern over a 360-degree angle. The network analyzer's S_{21} measures the power transmitted from port one to port two, or the power received by the receiver antenna. At the cut plate, the main antenna lobe has the highest amount of power transmitted.

To conduct this test, the reference antenna is used as a receiver once, and then, the AUT is set as the receiver. The maximum received power by the reference antenna is denoted as P_r, while the maximum received power of the AUT is denoted as P_{au}. The AUT gain can be set as:

$$G_{aut} = G_r + P_{aut} - P_r \qquad (5\text{-}1)$$

where G_{aut} is the gain of the reference antenna in dBi, which is provided by the manufacturer company. P_{aut} and P_r are in dB scale with the same sign that is readable from the network analyzer (negative). Generally speaking, the received power by the reference horn antenna is higher than P_{aut}, because the AUT has a lower gain than the reference one.

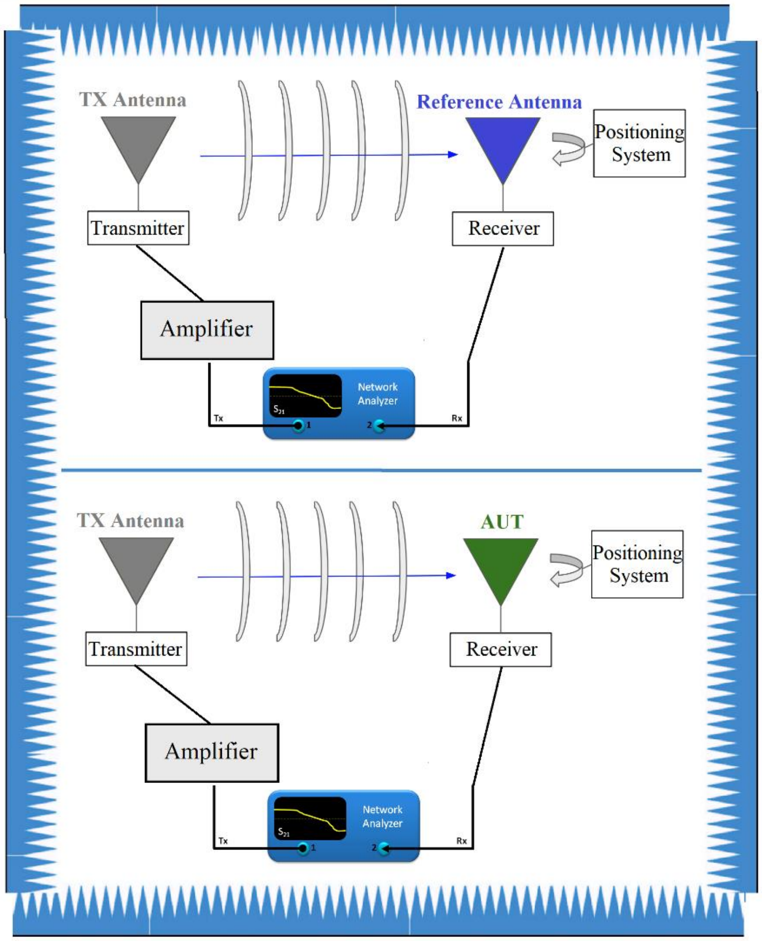

Figure 5-15 Schematic view of the AUT gain measurement setup

The antenna gain was measured twice: first by using a H-1498 broadband linearly polarized horn antenna as a standard one. This antenna has an operational frequency from 2 to 18 GHz. Then, by using a wideband dual polarization RCDLPHA2G18 horn antenna (2-18 GHz) for the reference antenna. This antenna has two ports, the second one was connected to a 50-ohm load during the measurements. The 3dB difference was considered in the gain calculation because of the circular polarization of the RCDLPHA antenna.

The gain of the proposed antenna in the U_{band} was measured twice: once in our model and a second time separately. The port one of the VNA was connected to the ZVA-02443HP+ 2-43.5 GHz RF amplifier (Fig. 5-16).

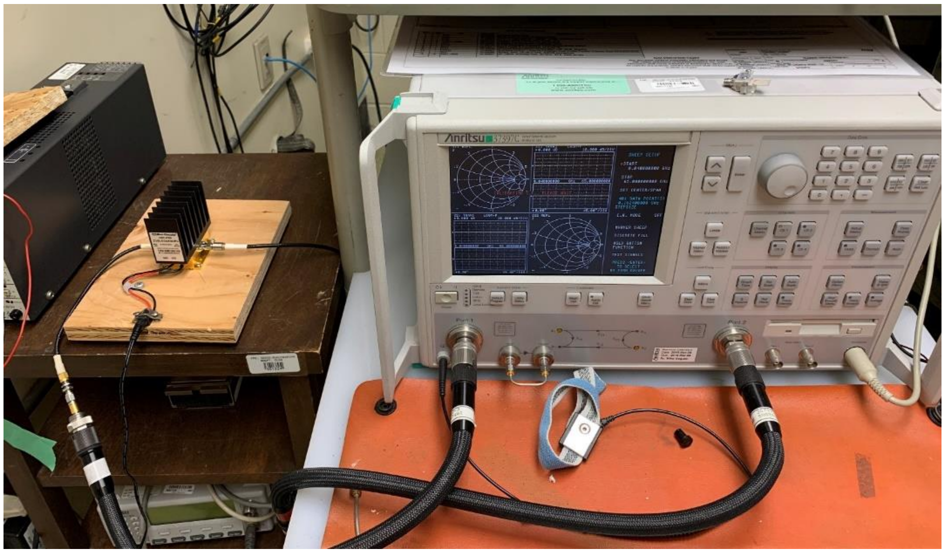

Figure 5-16 Far-field measurement setup, 37397 VNA and ZVA-02443HP+ amplifier

The setup for measuring the gain of prototype-I is depicted in Fig. 5-17. The CBCPW U_{band} antenna was fed from the top, and a yellow printed stand was used to hold it at the focal point.

The measured gain for Fig. 5-17 setup shows a gain drop in the whole antenna bandwidth. This drop is a result of the existence of the antenna holder and coaxial feed in front of the reflect, which is also known as feed blockage [78]. The antenna feeding position was rearranged, and the U_{band} antenna was rotated by 180 degrees to reduce feed blockage. Because of the symmetrical shape of the LB antenna-II which is the reflector, the radiation pattern of the proposed antenna is symmetrical, and the gain is the same after rotating the CBCPW antenna by 180 degrees. The new setup in Fig. 5-18 has half of the feed blockage compared to the previous. In this case The U_{band} antenna is fed and held from below.

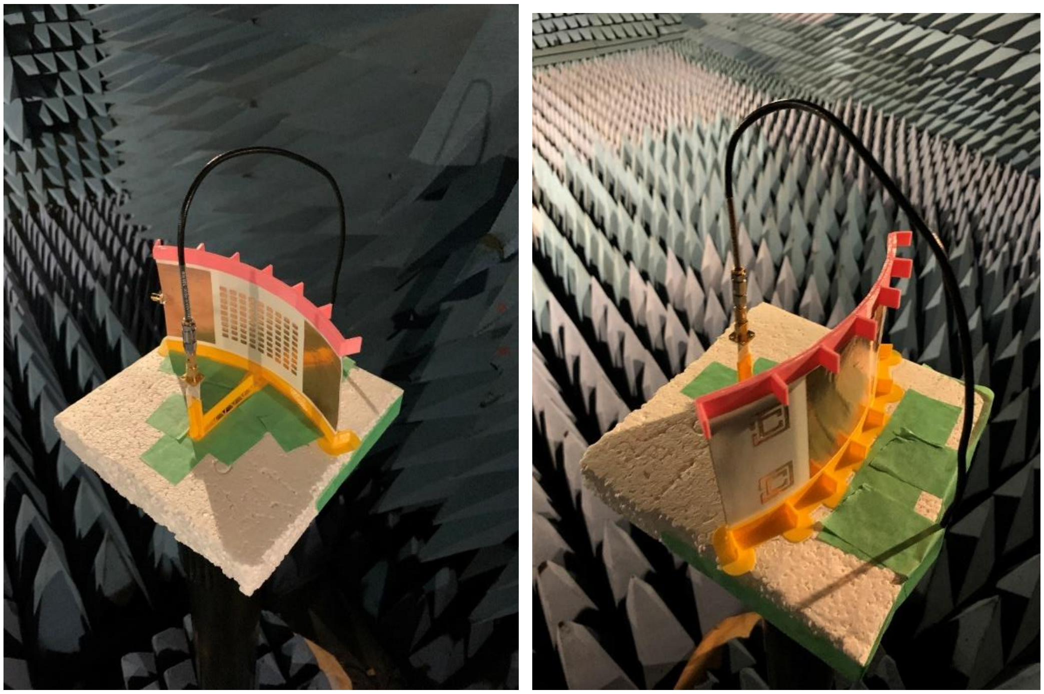

(a) (b)

Figure 5-17 Prototype-I in the antenna chamber; first set up, (a) front view, and (b) back view

The measured gain of the U_{band} antenna in our design (versus the single element CBCPW antenna) represented a significant gain improvement over the whole frequency, same as simulation, Fig. 5-19. The unavoidable aperture blockage of the coaxial feed put the measured gain slightly lower than the simulated one. But the measured gain follows the simulation results trend.

There are several factors that can impact the gain measurement of an antenna. One such factor is the signal-to-noise ratio (S/N) of the antenna chamber, which can vary with different frequencies. Additionally, the cable and connectors used in the measurement setup can exhibit different responses at different frequencies. Another factor to consider is the loss tangent of the PLA, which may not remain stable or show an expected upward trend as the frequency increases [208].

In this thesis, we are interested in the difference between the measured prototype and the CBCPW received power. Comparing these two together is a like-for-like analogy. Any external factors that can increase or decrease the antenna gain in the measurement are the same for each of them. Referring to equation (5-1) P_r indicates the antenna gain. Subtracting them, ΔP, gives the difference between gains.

The gain improvement in percentage is shown in Fig. 5-20. The linear amount of the gain was used to calculate the enhancement. The gain of the U_{band} antenna was considered as a reference and the ΔP as an increased one. Our method resulted in a significant gain improvement, with the gain increasing by more than 350% across the entire bandwidth. The maximum gain improvement is 1900% at frequencies of 12 GHz and 13.5 GHz.

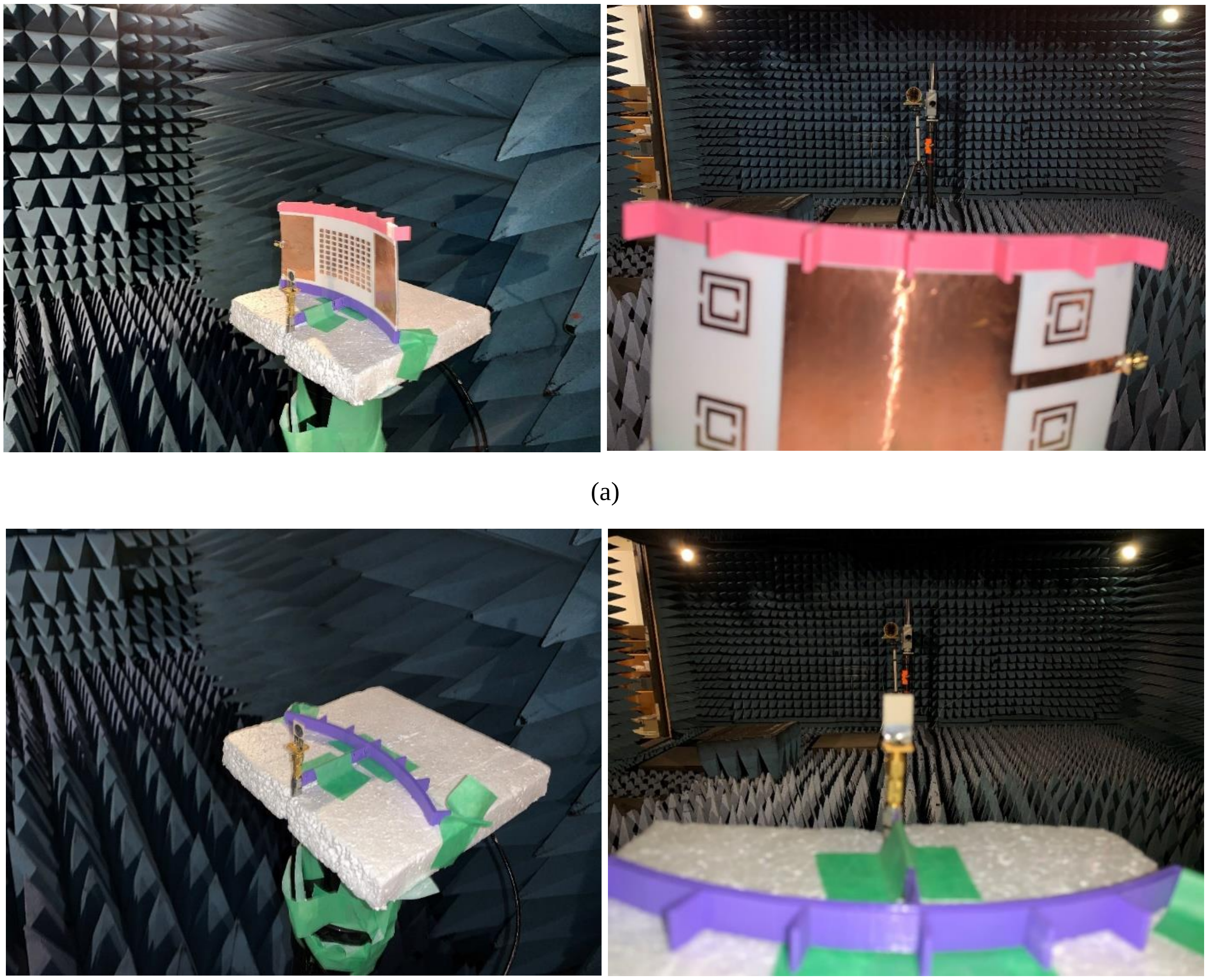

(a)

(b)

Figure 5-18 Fairfield measurement in antenna chamber, second setup (a) Prototype-I (b) single element CBCPW antenna; left front view, right back view

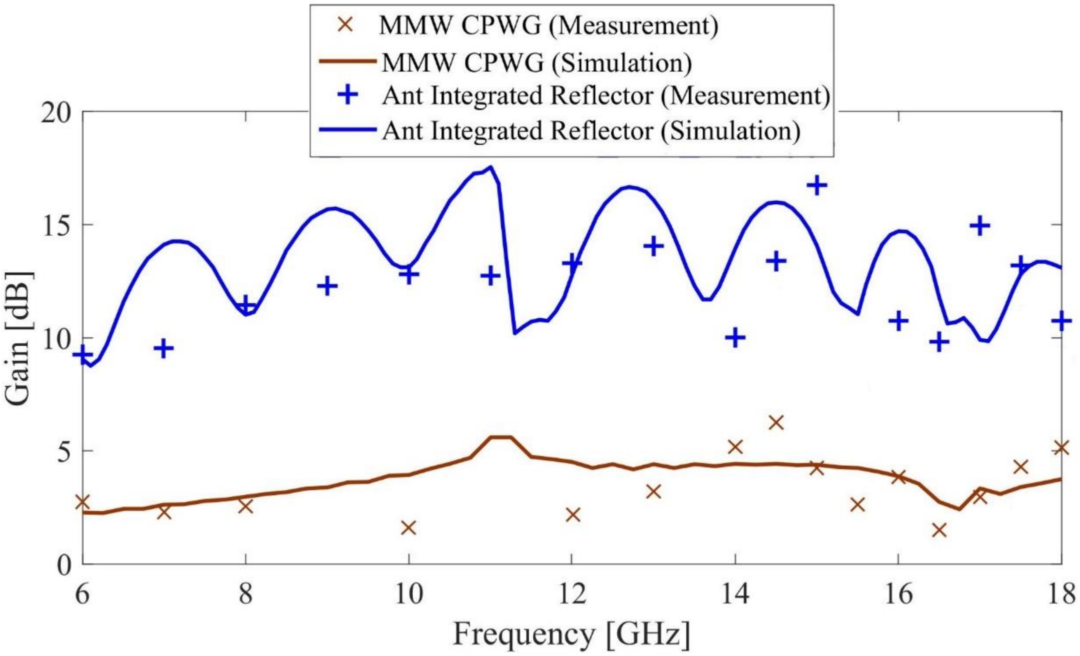

Figure 5-19 Measured gain of the prototype-I antenna vs. single element CBCPW antenna in 6 GHz – 18 GHz

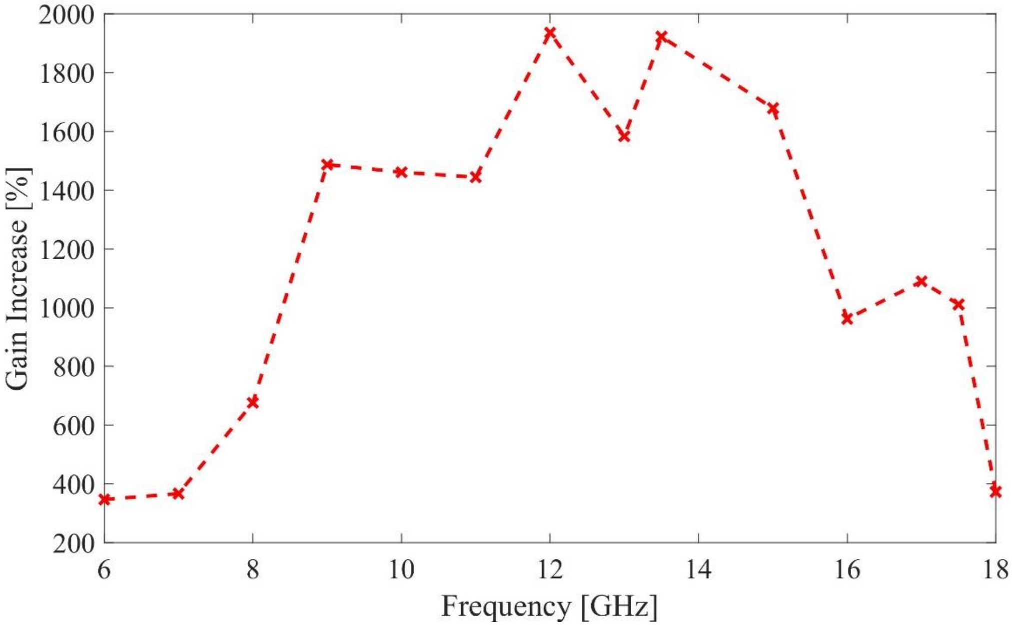

Figure 5-20 Antenna integrated reflector gain improvement compared to single element VS frequency; prototype-I

5.6 Prototype-I Radiation Pattern Measurements

The proposed method changed the upper band antenna radiation pattern from omnidirectional to directive. In contrast to the single element antenna out of our model, now it has a main stable lobe. Meanwhile, the proposed antenna's main lobe does not change at different modes.

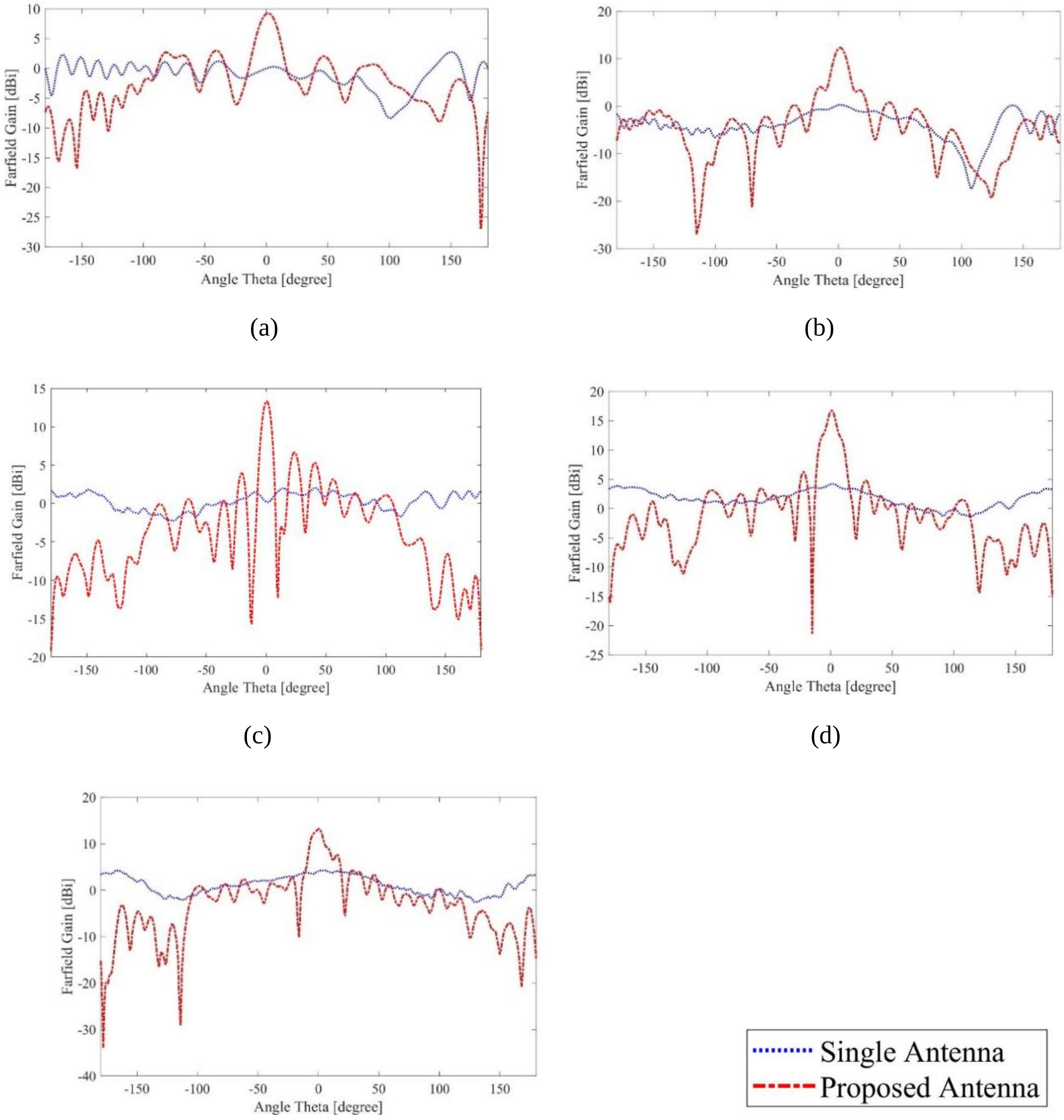

(a)

(b)

(c)

(d)

(e)

Figure 5-21 The radiation pattern of the single CBCPW antenna vs. while included in the prototype-I, (a) 6 GHz, (b) 9 GHz, (c) 12 GHz, (d) 15 GHz, and (e) 17.5 GHz

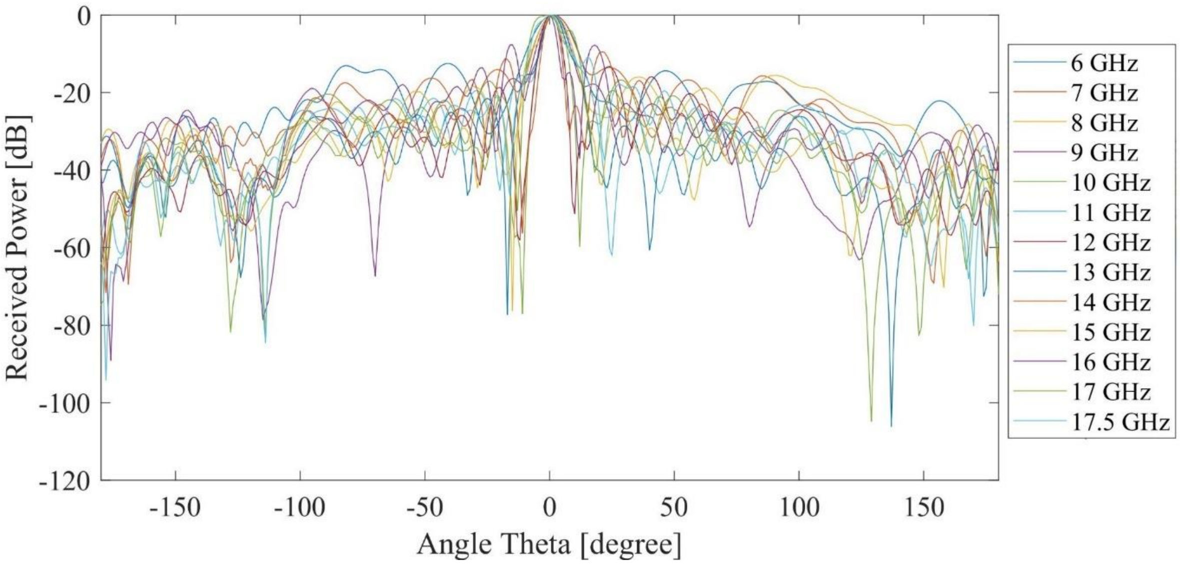

Figure 5-22 Received power by the prototype-I in 360 degrees in 20 log scale

The comparison between the radiation pattern of the single U_{band} antenna, the CBCPW one, and the proposed prototype-I, the CBCPW in our design, is presented in Fig. 5-21. The single CBCPW antenna has omnidirectional to bidirectional radiation pattern in the 6 GHz – 18 GHz bandwidth. The main lobe of the radiation pattern for a CBCPW antenna shifts direction with varying frequencies. This phenomenon is due to the antenna's wide bandwidth, which causes the radiation pattern to be excited by different modes [78].

At the beginning of the bandwidth, at 6 GHz, it has the main lobe at 150 degrees, and at 9 GHz it shifts to 0 degrees. Regarding the single antenna main lobe direction, our proposed method shows a directive radiation pattern. The proposed prototype antenna has a stable radiation pattern that remains constant at 0 degrees. The comparison of the main lobe levels between our model and the CBCPW antenna reveals that our model not only improves the CBCPW antenna gain, but also stabilizes its main lobe and radiation pattern. This phenomenon occurs due to the parabolic shape of the L_{band} antenna, which is similar to what was reported in [35]. The received power pattern in scale of $20 \log x$ in 360 degrees around the proposed antenna is shown in Fig. 5-22. It represents the fixed main lobe and high directivity in the studied areas with a step width of 1 GHz.

5.7 Prototype-II Bandwidth Measurements

As for prototype-II, Fig. 5-23, the LB antenna-II is for L_{band}, while the CPW PET antenna is for U_{band}. The process of measuring its S-parameters was similar to the one used for prototype-I. Prototype-II U_{band} S_{11} is shown in Fig. 5-24. The blue line refers to the single element CPW antenna and the red one when this CPW antenna is placed as a U_{band} in our model.

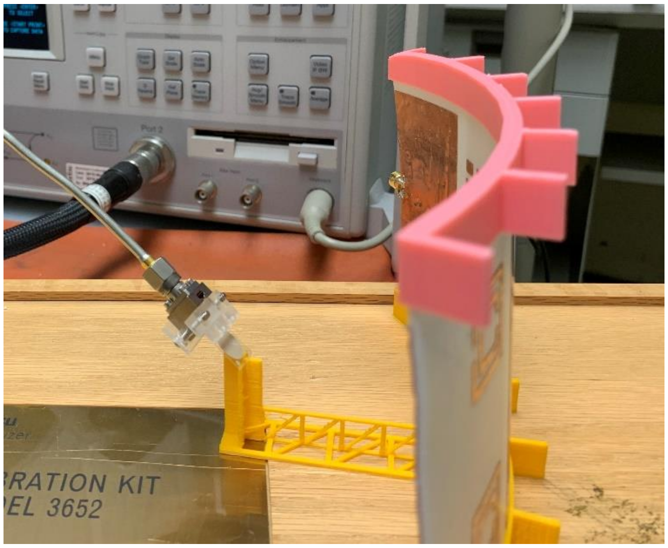

Figure 5-23 Prototype-II in antenna lab

The reflector does not change the antenna bandwidth, the antenna has a single resonant frequency at 15.4 GHz, and the prototype-II simulated bandwidth starts from 13 GHz up to 18 GHz (BW = 32%). Same as simulated data, measurement data showed wide bandwidth. Measured S_{11} has the same single resonance frequency as simulation with a small shift to a higher frequency. The small ripples are mainly because of the cable losses at such a high frequency. The measured single CPW antenna represented the same bandwidth as the black dashed line on the graph. We avoided including unnecessary plots and did not plot the graph because the bandwidth of the CPW in our structure is our subject.

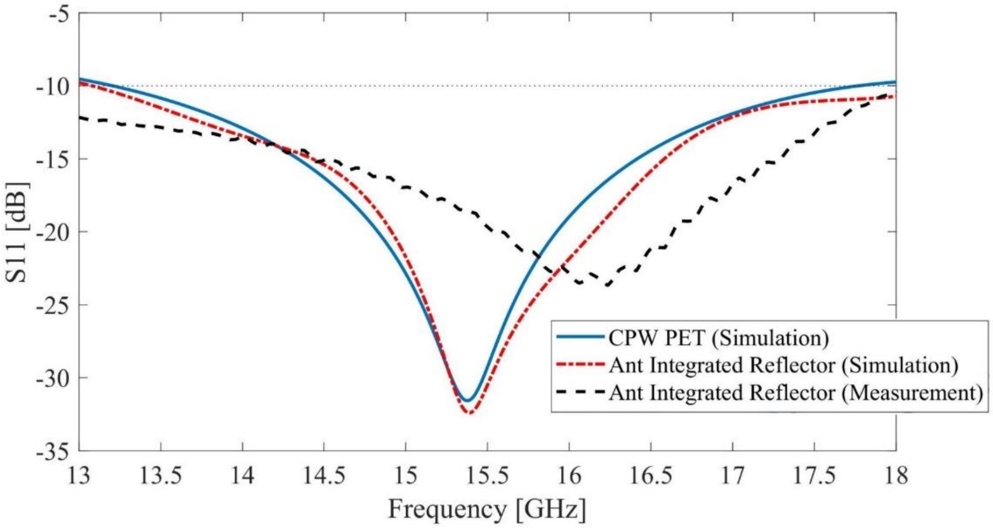

Figure 5-24 Measured S_{11} of the prototype-II upper band

5.8 Prototype-II Fairfield Measurements

Fig. 5-25 illustrates the experimental arrangement utilized to determine the gain and radiation pattern of prototype-II. During the initial measurements of prototype-I, the gain of prototype-II was evaluated utilizing the configuration depicted in Fig. 5-25 (a). The antenna was secured in its feed position by a 3D printed holder and excited by a coaxial cable from behind. However, due to the high feed blockage, as explained in detail in section 5-4, the gain obtained was very low. In the subsequent setup, shown in Fig. 5-25 (b), the antenna feed holder was removed, and the coaxial feed line was used to hold the antenna in place.

The prototype-II gain in Fig. 5-26 follows the simulation gain trend with a lower value; this drop can be compensated if we add the estimated aperture blockage to this value so that it will reach the simulated one, e.g., at 17 GHz, we have a measured 2.5 dB gain drop for Fig. 5-25 (a) vs (b) setups. Please note that the feed blockage in Fig. 5-25 (a) is twice as severe as the one seen in the Fig. 5-25 (b) configuration (the holder width and coaxial cable width are assumed to be the same in the wave path.). Therefore, this indicates that there is a reduction of approximately 2.5 dB in the measured results due to the feed blockage caused by the coaxial feed line. The agreement between the simulated and measured gain of the CPW antenna, using the setup depicted in Fig. 5-25(c), is demonstrated in Fig. 5-26.

The percentage improvement in measured gain, by considering the CPW single element antenna gain as a reference, is presented in Fig. 5-27. The measured gain improvement in percentage by considering the single element one as a reference is presented in Fig. 5-27. The percentage was calculated using a linear scale for the gain, and a significant increase can be observed. Specifically, the U_{band} gain has improved by at least 230 % and up to 760 %.

5.9 Prototype-II Radiation Pattern Measurements

The CPW antenna based on PET has a bidirectional radiation pattern because of its monopole structure. The radiation pattern changes slightly in the antenna’s wide bandwidth due to exciting different modes. But the proposed method changes its radiation pattern to a directive one with a single main lobe as presented in Fig. 5-28. The value of the main lobe in Prototype-II is consistently greater than that of CPW antenna due to Prototype-II's higher gain in comparison to CPW.

The power received by Prototype-II at various frequencies in dB scale ($20 \log x$) is illustrated in Fig. 2-29. The antenna maintains a constant main lobe direction throughout the operational bandwidth.

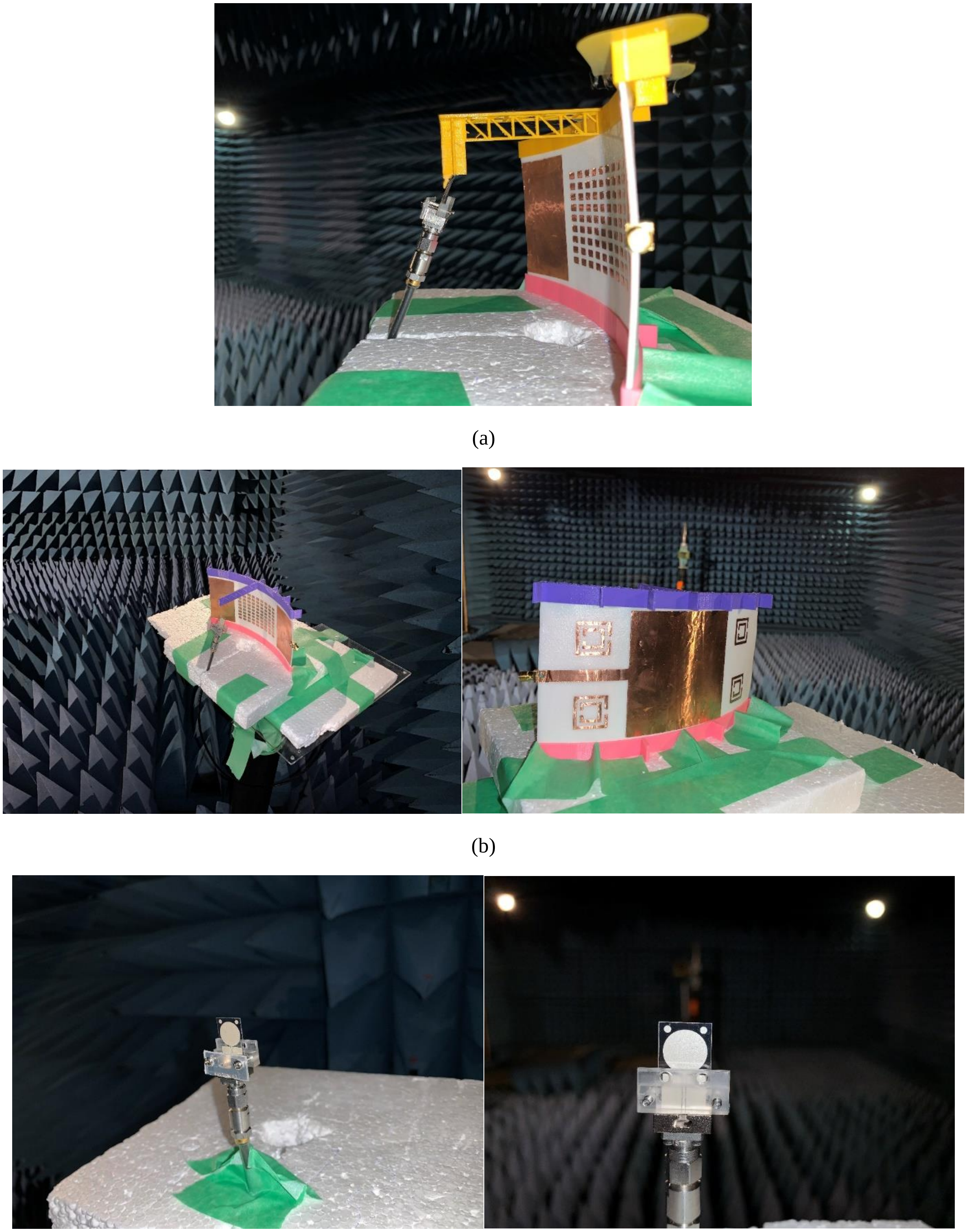

(a)

(b)

(c)

Figure 5-25 Far-field measurement in antenna chamber (a) prototype II – first setup (b) prototype II – final setup, and (c) single element CPW PET antenna; left front view, right back view

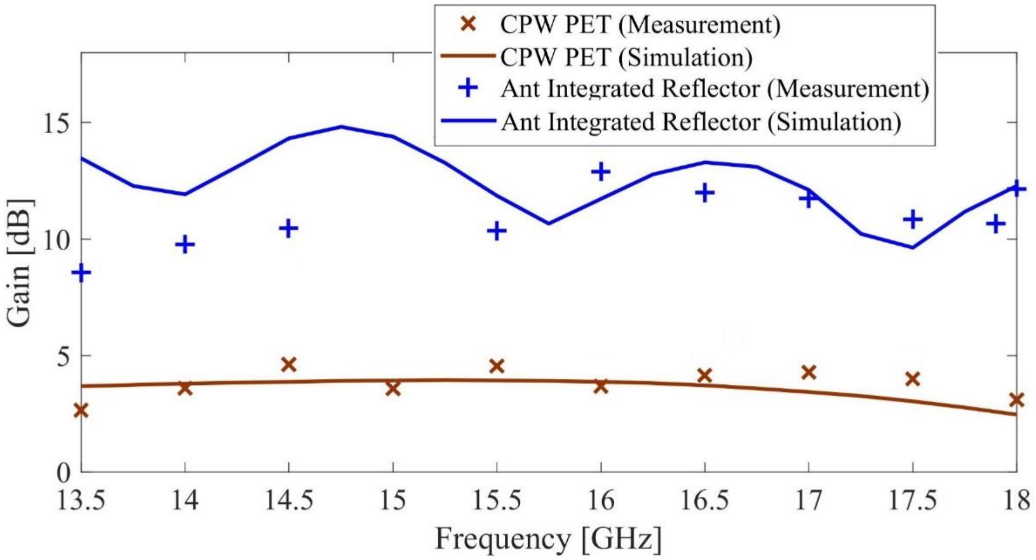

Figure 5-26 Measured gain of prototype-II antenna VS single element CPW PET antenna in 13.5 – 18 GHz

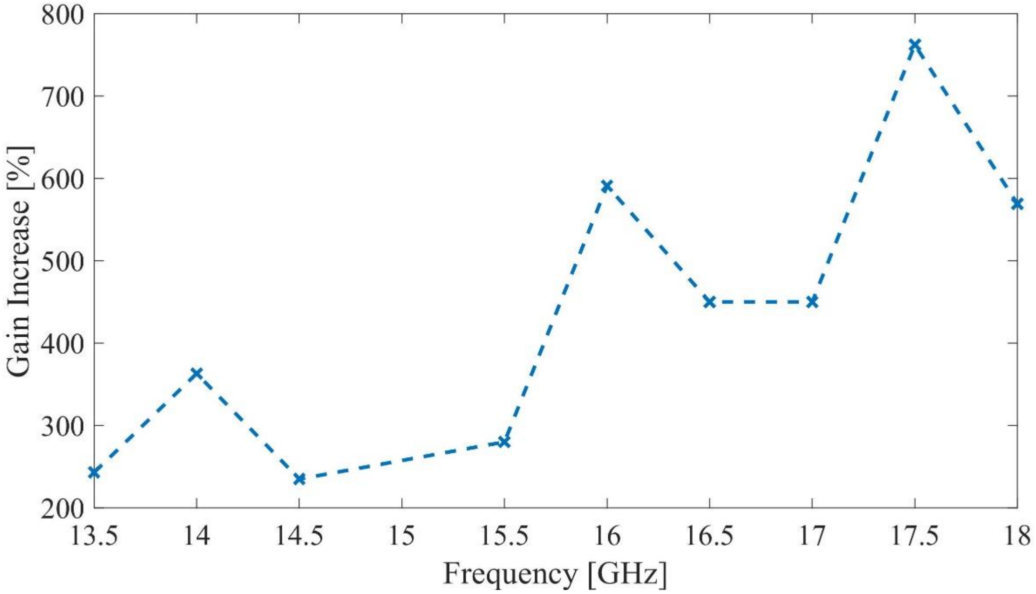

Figure 5-27 The gain improvement in our method compared to single element VS frequency; prototype-II

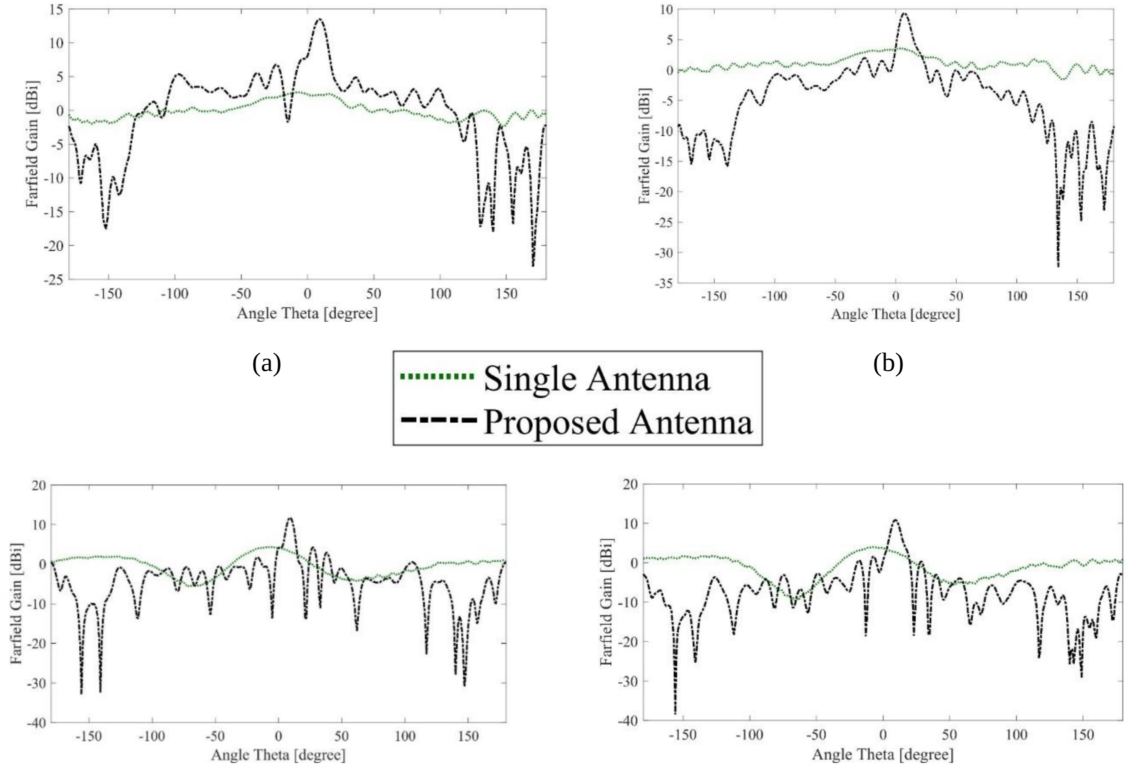

(a) (b)

(c) (d)

Figure 5-28 The radiation pattern of the single PET antenna VS in the proposed design II, (a) 13.5 GHz, (b) 14 GHz, (c) 17 GHz, and (d) 17.5 GHz

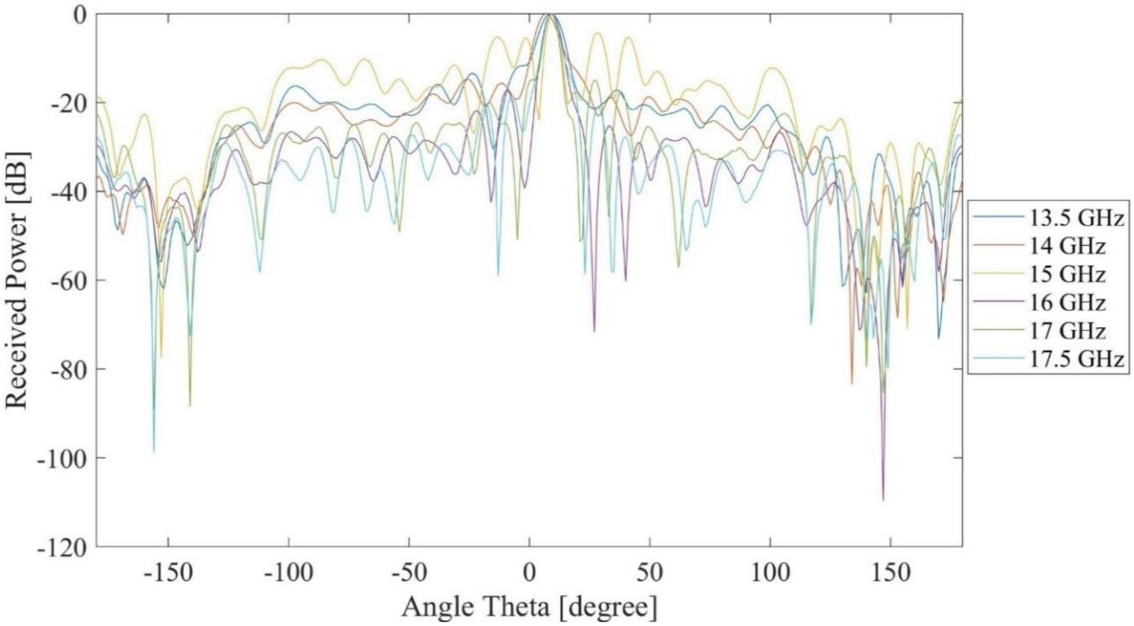

Figure 5-29 Received power by the proposed prototype antenna II in 360 degrees in 20 log scale

5.10 Prototypes Comparison

Both prototypes have fulfilled the aim and goal of this thesis work, as both antennas have recorded a measured FR that exceeds 8 and possess a wide bandwidth. They have dual bandwidths while prototype-I has a maximum bandwidth of 100%, and prototype-II has a bandwidth of up to 86%.

It was asserted that a significant gain improvement was achieved at U_{band}. Prototype-I showed a measured gain improvement of 12.6 dB, while prototype-II demonstrated a gain improvement of 8.7 dB.

The superior performances of our prototypes over existing dual-band antennas are shown in Table 5-1 in terms of bandwidth and FR. Table 5-2 compares the achieved gain improvement in our proposed method with published works.

5.11 Conclusion

Two antenna integrated reflector prototypes were fabricated and measured. Both prototypes proved the effectiveness and advantages of our proposed method to design a high-performance dual-band antenna with large FR. The prototype-I has a flexible L_{band} antenna (LB antenna-II) that operates around 1.4 GHz central frequency. The U_{band} antenna was fabricated on Rogers 4003 substrate and the antenna has a CBCPW planar structure. Prototype-I U_{band} has a measured bandwidth of 6 GHz – 18 GHz and -40 dB minimum S_{11}.

The prototype-II has the same LB antenna-II for its L_{band} with 32.3% measured bandwidth. The CPW antenna was used for the U_{band} antenna. The antenna was fabricated on transparent PET with conductive ink. The prototype-II upper bandwidth has a central frequency at 15.5 GHz. The prototype-II dual-band antenna achieved the maximum gain of 12.9 dB in measurement. The antenna U_{band} gain jumped significantly in the bandwidth, e.g., 760 % at 17.5 GHz.

Both prototype antennas have an omnidirectional radiation pattern at the L_{band} and a directive radiation pattern at the U_{band} as they were designed to work. The U_{band} antenna does not deteriorate the antenna performance in the L_{band} and vice versa. The L_{band} antenna acts as an microwave antenna and at the same time a reflectarray/cylindrical reflector for the U_{band} one.

Both prototypes have a very lightweight, compact size, and was made by a low-price fabrication method. It was easy to assemble the antenna, so they are good candidates for remote areas too.

Table 5-1 Comparison between our antennas and literature dual-band antennas

References	Operation Frequencies	FR	Max BW	Structure	Year
[209]	0.91 GHz / 2.41 GHz	2.7	≤ 2 %	Modified Split Ring	2021
[122]	0.69 GHz – 0.96 GHz / 3.3 GHz – 5 GHz	5	41 %	UB-FSS-LB and FSS	2020
[27]	5.4 GHz – 5.9 GHz / 13.2 GHz – 14.2 GHz	2.43	9 %	Co-Aperture Planar	2020
[24]	2.6 GHz / 3.5 GHz	1.4	≤ 2 %	metasurface-based decoupling method	2020
[123]	2 GHz – 4.9 GHz / 26 GHz – 28.88 GHz	~ 8	84 %	Microstrip	2020
[28]	3.5 GHz / 4.9 GHz	1.4	≤ 2 %	8 Loop Antenna Elements	2020
[18]	5.29 GHz – 6.12 GHz / 26 GHz – 29.5 GHz	4.86	14 %	Microstrip	2020
[113]	12.04 GHz – 13.88 GHz / 14.15 GHz – 14.58 GHz	1.1	14 %	SW-SIW	2020
[210]	3.42 GHz – 3.6 GHz / 4.7 GHz – 5.1 GHz	~ 1.4	8 %	Electromagnetic Bandgap (EBG)	2019
[188]	25.2 GHz – 34.3 GHz / 37.4 GHz – 41.5 GHz	~ 1.3	31 %	CPW-Fed	2019
[211]	8.2 GHz – 9.4 GHz / 13.2 GHz – 15.2 GHz	1.6	14 %	leaky-wave antenna (LWA) based on substrate-integrated waveguide (SIW)	2019
[25]	3.38 GHz / 4.96 GHz	1.5	≤ 2 %	waveguided metamaterial (WG-MTM)	2019
[114]	3.73 GHz – 3.89 GHz / 5.4 GHz – 5.85 GHz 24.4 GHz – 29.3 GHz	Max 7	18 %	Defected Ground Structure (DGS)	2019

[124]	5.8 GHz – 8.5 GHz / 35 GHz – 41.5 GHz	5.3	38 %	dual-mode composite microstrip line (DMC-MSL)	2018
[29]	2.5 GHz – 2.69 GHz / 3.3 GHz – 3.6 GHz	1.32	9 %	Filtering Stubs	2018
Prototype-I	**0.69 GHz – 1.74 GHz / 6 GHz – 18 GHz**	**9.9**	**100 %**	**Novel Antenna Integrated Reflector**	**2023**
Prototype-II	**0.69 GHz – 1.74 GHz / 13 GHz – 18 GHz**	**12.8**	**86 %**	**Novel Antenna Integrated Reflector**	**2023**

Table 5-2 Comparison between gain improvement in our method and literature

References	Gain Enhancement Method	Feed Antenna Configuration	Feeding Method	Peak Gain Enhancement (dB)
[212]	Artificial Magnetic Conductor (AMC) Reflector	Monopole Patch Antenna	CPW	8.7
[19]	Flat Metal Reflector	Partially Grounded Monopole Antenna	Microstrip	4.3
[213]	Frequency Selective Surface (FSS) Array	Monopole CPW Antenna	CPW	3.5
[214]	Frequency Selective Surface (FSS) Reflector	Slotted Ground Microstrip Antenna	Microstrip	4
Prototype-I	**Antenna Integrated Reflector**	**CBCPW Monopole Antenna**	**CBCPW**	**12.6**
Prototype-II	**Antenna Integrated Reflector**	**CPW Flexible Monopole Antenna**	**CPW**	**8.7**

Chapter 6 – Conclusions and Future Work

6.1 Summary of the Work Achieved

This thesis study was motivated by the need to have dual-band wireless communications with a large center FR. It is capable of working in both lower and upper bands, targeting 5G applications in 5G FR1 and FR2, respectively. Another advantage of our method for proposing a dual-band antenna is its ability to offer a wide bandwidth and achieve significant improvements in gain at the upper band.

To the best of the author's knowledge, none of the existing published approaches showed such a large central FR, wide bandwidth, and gain. Meanwhile, most of them suffer from a lack of a specific method to design a dual-band antenna.

In this thesis, a novel method to design a dual-band antenna with a large FR meanwhile significantly improve the U_{band} antenna gain was proposed. Meanwhile, the final dual-band antenna has an integrated structure. Out of this method, two antenna integrated reflectors were studied, and two prototypes showed the proof of concept.

First, a general model for the dual-band antenna integrated reflector was proposed and named Model IV based on theory and calculation. This model does not cater to a specific frequency and has the potential to generate a variety of antennas for different frequency ranges.

Subsequently, a L_{band} antenna named LB antenna-II was developed to meet the specific requirements of Model IV. Two antenna integrated reflectors (AIR-I and AIR-II) were then proposed, utilizing LB antenna-II along with different U_{band} antennas. It is noteworthy that these AIR-I and AIR-II structures are identical to that of Model IV, but were specifically simulated for distinct frequency bands.

Finally, the AIR-II was optimized to meet the measurement limits in our antenna chamber, and two prototypes, named prototype-I and prototype-II, were fabricated. Prototype-I was created based on the AIR-II design, while in prototype-II, the U_{band} antenna was replaced with another one that we have strong evidence to support as a viable concept in our methodology.

Prototype-I has a measured central FR of 9.9, while prototype-II has a ratio of 12.8. Both antennas exhibit a wide bandwidth and significant gain improvements. Prototype-I boasts a maximum bandwidth of 100%, while prototype-II has a bandwidth of 86%. The peak gain improvement for prototype-I was 12.6 dB, and for prototype-II it was 8.7 dB. In comparison to approximately 20 similar works in literature, both prototypes demonstrated superior performance.

6.2 Key Contributions

A new method for designing a dual-band antenna with a large FR has been proposed. The proposed model has a unique structure that achieves the large FR through the hybrid dual-band antenna design techniques, and the gain improvement in the U_{band} is achieved by using a parabolic reflector design for the antenna.

An L_{band} antenna has been designed to function both as a radiator and a reflector for other antennas. The back side of the L_{band} antenna consists of a combination of reflectarray elements and parabolic reflector structures. This design allows for a significant improvement in gain at the U_{band} at the frequency of the reflectarray elements, and also improves the U_{band} gain outside of the operational frequency of the reflectarray, thanks to the infinite bandwidth of the parabolic reflector. The radiation patch of the L_{band} antenna functions as both a L_{band} radiator and U_{band} reflectarray ground simultaneously.

Two antenna integrated reflectors were designed out of the method. They got simulated FR of 10.1 for the first one named AIR-I, 9.5 and 18 for the second one named AIR-II. The AIR-II U_{band} antenna was designed as a dual-band antenna with two upper bands: one located above 20 GHz and another below 20 GHz. The 20 GHz limit was due to our measurement facility in the antenna lab. Therefore, in this case, AIR-II FR = 18 (24 GHz / 1.35 GHz) was used to demonstrate the antenna's applications towards 5G. On the other hand, the FR = 9.5 (13 GHz / 1.35 GHz) was measured in the lab to serve as proof of concept for the AIR-II.

While one sample would have sufficed for the proof of concept, two samples were created and tested to allow for more comprehensive investigation and to produce additional data that would provide stronger support for the model presented in this thesis. Their S_{11}, gain, and radiation patterns were measured and found to closely match the simulation results. The model was designed in a way that allowed for low-cost fabrication using inexpensive 3D printer materials and a Circuit. The proposed antenna features a portable structure and can be assembled manually, as was done in the fabrication of prototypes I and II.

6.3 Future Work

The work presented can be further improved in different ways:

- Development of a generic method for multiband antenna design. The proposed method was provided for dual-band applications. However, further study can focus on obtaining several bands for multi-band communications, e.g., satellite and LoT applications. One method that can be achieved is by using a dual-band antenna for upper band, a similar approach to the one used in designing the AIR-II. An alternative approach could be to use three layers of antennas that work in tandem with one another. This would involve having separate antennas for the lower, middle, and upper bands, with the lower band antenna also acting as a reflector for the middle band antenna, and the middle band antenna serving as a reflector for the upper band antenna.

- Studying the miniaturizing of the antenna integrated reflector to make the whole structure planar and decrease the distance between the upper band and lower band antennas. This one can be quiet challenging because approaching the feed to the reflector will disturb the reflector performance and put the dish in the antenna near field. Meanwhile, approaching these antennas too closely together would decrease the upper band antenna's bandwidth. Using a flat reflector can make the structure planar, but on the flip side, this type of reflector cannot significantly increase the antenna gain. This type of antenna will be well-suited for applications where sacrificing gain in exchange for a smaller overall size is advantageous such as in portable devices.
- Finally, designing a flat lower band antenna as a planar reflectarray plate for the upper band feed antenna. Because of eliminating the parabolic reflector here, this approach eliminates the need for flexible antennas, simplifying the fabrication process. On the flip side, reflectarrays have limited bandwidth, and designing them to cover the wide bandwidth required for 5G FR2 is challenging. Additionally, the reflectarray elements can negatively impact the performance of the lower band antenna. This study provides a brief overview of reflectarrays used in conjunction with parabolic reflectors to increase antenna gain.

◆ References

[1] J. Guo, L. Cui, C. Li, and B. Sun, “Side-edge frame printed eight-port dual-band antenna array for 5G smartphone applications,” IEEE Trans. Antennas Propag., vol. 66, no. 12, pp. 7412–7417, 2018.

[2] D. P. Agrawal and Q.-A. Zeng, Introduction to Wireless and Mobile Systems. Cengage learning, 2015.

[3] R. O. Adeogun, “Joint resource allocation for dual—band heterogeneous wireless network,” in 2018 IEEE Wireless Communications and Networking Conference (WCNC), 2018, pp. 1–5.

[4] T. S. Rappaport, “Wireless Communications--Principles and Practice, (The Book End),” Microw. J., vol. 45, no. 12, pp. 128–129, 2002.

[5] W. Stallings and W. Stallings, Wireless Communications and Networks, 2nd ed. Upper Saddle River, NJ: Pearson Prentice Hall, 2005.

[6] Y. Zhang, Y. Zhang, D. Li, K. Liu, and Y. Fan, “Dual-polarized band-notched antenna without extra circuit for 2.4/5 GHz WLAN applications,” IEEE Access, vol. 7, pp. 84890–84896, 2019.

[7] O. Semiari, W. Saad, and M. Bennis, “Joint millimeter wave and microwave resources allocation in cellular networks with dual-mode base stations,” IEEE Trans. Wirel. Commun., vol. 16, no. 7, pp. 4802–4816, 2017.

[8] M. M. da Silva and J. Guerreiro, “On the 5G and beyond,” Appl. Sci., vol. 10, no. 20, p. 7091, 2020.

[9] L. Zhang et al., “A survey on 5G millimeter wave communications for UAV-assisted wireless networks,” IEEE Access, vol. 7, pp. 117460–117504, 2019.

[10] M. Zuo, J. Ren, R. Hou, X. Du, Z. Chen, and Y. Yin, “Compact dual-band antenna with large frequency ratio,” AEU-International J. Electron. Commun., vol. 141, p. 153978, 2021.

[11] Y.-F. Lin, H.-M. Chen, and C.-H. Lin, “Compact dual-band hybrid dielectric resonator antenna with radiating slot,” IEEE Antennas Wirel. Propag. Lett., vol. 8, pp. 6–9, 2008.

[12] H. Al-Saedi, J. A. Attari, W. M. A. Wahab, R. Mittra, and S. Safavi-Naeini, “Single-feed dual-band aperture-coupled antenna for 5G applications,” in 2018 18th International Symposium on Antenna Technology and Applied Electromagnetics (ANTEM), 2018, pp. 1–2, doi: 10.1109/ANTEM.2018.8572907.

[13] S. F. Abdulkarim, A. J. Salim, J. K. Ali, A. I. Hammoodi, M. T. Yassen, and M. R. Hassan, “A compact peano-type fractal based printed slot antenna for dual-band wireless applications,” in 2013 IEEE International RF and Microwave Conference (RFM), 2013, pp. 329–332, doi: 10.1109/RFM.2013.6757278.

[14] U. Naeem, S. Bila, M. Thévenot, and E. Arnaud, “Design methodology for dual-band hybrid antennas with off-resonance loading,” IET Microwaves, Antennas Propag., vol. 11, no. 14, pp. 2077–2082, 2017.

[15] Y. Chen, J. Zhao, and S. Yang, “A novel stacked antenna configuration and its applications in dual-band shared-aperture base station antenna array designs,” IEEE Trans. Antennas Propag., vol. 67, no. 12, pp. 7234–7241, 2019.

[16] B. J. Xiang, S. Y. Zheng, H. Wong, Y. M. Pan, K. X. Wang, and M. H. Xia, “A flexible dual-band antenna with large frequency ratio and different radiation properties over the two bands,” IEEE Trans. Antennas Propag., vol. 66, no. 2, pp. 657–667, 2017.

[17] J.-D. Zhang, W. Wu, and D.-G. Fang, “Dual-band and dual-circularly polarized shared-aperture array antennas with single-layer substrate,” IEEE Trans. Antennas Propag., vol. 64, no. 1, pp. 109–116, 2015.

[18] S. Iffat Naqvi et al., "Integrated LTE and millimeter-wave 5G MIMO antenna system for 4G/5G wireless terminals," Sensors, vol. 20, no. 14, p. 3926, 2020.

[19] P. Jiang, W. Jiang, W. Hu, and S. Gong, “An interlaced grid dual-band dual-polarized bandpass FSS with a large band ratio,” IEEE Antennas Wirel. Propag. Lett., vol. 21, no. 5, pp. 1027–1031, 2022.

[20] Z. Hamzavi-Zarghani and Z. Atlasbaf, “A new broadband single-layer dual-band reflectarray antenna in X-and Ku-bands,” IEEE Antennas Wirel. Propag. Lett., vol. 14, pp. 602–605, 2014.

[21] C. Han, J. Huang, and K. Chang, “A high efficiency offset-fed X/Ka-dual-band reflectarray using thin membranes,” IEEE Trans. Antennas Propag., vol. 53, no. 9, pp. 2792–2798, 2005.

[22] T. Su, X. Yi, and B. Wu, “X/Ku dual-band single-layer reflectarray antenna,” IEEE Antennas Wirel. Propag. Lett., vol. 18, no. 2, pp. 338–342, 2019.

[23] R. Dilli, “Analysis of 5G wireless systems in FR1 and FR2 frequency bands,” in 2020 2nd International Conference on Innovative Mechanisms for Industry Applications (ICIMIA), 2020, pp. 767–772.

[24] F. Liu, J. Guo, L. Zhao, G. Huang, Y. Li, and Y. Yin, "Dual-band metasurface-based decoupling method for two closely packed dual-band antennas," IEEE Trans. Antennas Propag., vol. 68, no. 1, pp. 552–557, 2020, doi: 10.1109/TAP.2019.2940316.

[25] C. Guo, H. Zhai, and S. Liu, "A new dual-band microstrip antenna array with high isolation by waveguided metamaterial structure," Microw. Opt. Technol. Lett., vol. 61, no. 5, pp. 1365–1370, 2019.

[26] Y. Zhu, Y. Chen, and S. Yang, “Decoupling and low-profile design of dual-band dual-polarized base station antennas using frequency-selective surface,” IEEE Trans. Antennas Propag., vol. 67, no. 8, pp. 5272–5281, 2019.

[27] J. Wu, C. Wang, and Y. X. Guo, "Dual-band co-aperture planar array antenna constituted of segmented patches," IEEE Antennas Wirel. Propag. Lett., vol. 19, no. 2, pp. 257–261, 2020, doi: 10.1109/LAWP.2019.2958845.

[28] X.-. T. Yuan, Z. Chen, J. Li, and T. Yuan, "A compact dual-band and high-isolation MIMO antenna system for 5G smartphone applications," in 2020 IEEE MTT-S International Microwave Workshop Series on Advanced Materials and Processes for RF and THz Applications (IMWS-AMP), 2020, pp. 1–3, doi: 10.1109/IMWS-AMP49156.2020.9199661.

[29] Y. Liu, S. Wang, N. Li, J. Wang, and J. Zhao, "A compact dual-band dual-polarized antenna with filtering structures for sub-6 GHz base station applications," IEEE Antennas Wirel. Propag. Lett., vol. 17, no. 10, pp. 1764–1768, 2018.

[30] J. Guo, J. Fan, L. Sun, and B. Sun, “A four-antenna system with high isolation for mobile phones,” IEEE Antennas Wirel. Propag. Lett., vol. 12, pp. 979–982, 2013.

[31] B. Feng, L. Li, and J.-C. Cheng, “A dual-band dual-polarized stacked microstrip antenna with high-isolation and band-notch characteristics for 5G microcell communications,” IEEE Trans. Antennas Propag., vol. 67, no. 7, pp. 4506–4516, 2019.

[32] P. J. (Peter J. Wood, Reflector Antenna Analysis and Design. Stevenage [Eng.] ; P. Peregrinus on behalf of the Institution of Electrical Engineers, 1980.

[33] M. Faridani, R. A. Sadeghzadeh, and M. Khatir, “Terahertz dual-band dipole antenna with novel small flat quartz-copper reflector,” Optik (Stuttg)., vol. 136, 2017, doi: 10.1016/j.ijleo.2017.02.055.

[34] A. Chatterjee and S. K. Parui, “Performance enhancement of a dual-band monopole antenna by using a frequency-selective surface-based corner reflector,” IEEE Trans. Antennas Propag., vol. 64, no. 6, pp. 2165–2171, 2016, doi: 10.1109/TAP.2016.2552543.

[35] J. W. M. Baars, The Paraboloidal Reflector Antenna in Radio Astronomy and Communication Theory and Practice, 1st ed. 20. New York, NY: Springer New York, 2007.

[36] H. Xu, X. Zhao, and B. Li, “A low-RCS parabolic reflector antenna using absorptive frequency-selective reflector,” in 2021 International Applied Computational

Electromagnetics Society (ACES-China) Symposium, 2021, pp. 1–2, doi: 10.23919/ACES-China52398.2021.9581547.

[37] P. Nayeri, F. Yang, and A. Z. Elsherbeni, Reflectarray Antennas: Theory, Designs, and Applications. Wiley Online Library, 2018.

[38] J. Huang and J. A. Encinar, Reflectarray Antennas. IEEE, 2007.

[39] S. Hossain, "5G wireless communication systems," Am. J. Eng. Res., vol. 2, no. 10, pp. 344–353, 2013.

[40] J. Rodriguez, Fundamentals of 5G Mobile Networks. John Wiley & Sons, 2015.

[41] S. Li, L. Da Xu, and S. Zhao, "5G internet of things: A survey," J. Ind. Inf. Integr., vol. 10, pp. 1–9, 2018.

[42] J. Li et al., "5g new radio for public safety mission critical communications," arXiv Prepr. arXiv2103.02434, 2021.

[43] Y. Corre, T. Tenoux, J. Stéphan, F. Letourneux, and Y. Lostanlen, "Analysis of outdoor propagation and multi-cell coverage from ray-based simulations in sub-6GHz and mmwave bands," in 2016 10th European Conference on Antennas and Propagation (EuCAP), 2016, pp. 1–5.

[44] S. Sicari, A. Rizzardi, and A. Coen-Porisini, "5G In the internet of things era: An overview on security and privacy challenges," Comput. Networks, vol. 179, p. 107345, 2020, doi: 10.1016/j.comnet.2020.107345.

[45] S. Čaušević and A. Medić, "4G to 5G network evolution: Advantages and differences," SAR J., vol. 4, no. 4, pp. 153–159, 2021, doi: 10.18421/SAR44-01.

[46] "What is 5G? how will it Transform our world?," Ericsson, 30-Mar-2023. [Online]. Available: https://www.ericsson.com/en/5g. [Accessed: 05-Apr-2023].

[47] A. Ali, N. González-Prelcic, and A. Ghosh, "Millimeter wave V2I beam-training using base-station mounted radar," in 2019 IEEE Radar Conference (RadarConf), 2019, pp. 1–5.

[48] B. Bulut, "5G NR C-V2V for high speed train safety applications," in 2020 28th Signal Processing and Communications Applications Conference (SIU), 2020, pp. 1–4, doi: 10.1109/SIU49456.2020.9302510.

[49] M. Dighriri, A. S. D. Alfoudi, G. M. Lee, and T. Baker, "Data traffic model in machine to machine communications over 5G network slicing," in 2016 9th International Conference on Developments in eSystems Engineering (DeSE), 2016, pp. 239–244, doi: 10.1109/DeSE.2016.54.

[50] T. Zemen, “Wireless 5G ultra reliable low latency communications: European and Austrian research initiatives,” Elektrotechnik und Informationstechnik, vol. 135, no. 7, pp. 445–448, 2018, doi: 10.1007/s00502-018-0645-0.

[51] X. Ge, “Ultra-reliable low-latency communications in autonomous vehicular networks,” IEEE Trans. Veh. Technol., vol. 68, no. 5, pp. 5005–5016, 2019, doi: 10.1109/TVT.2019.2903793.

[52] D. Jiang and G. Liu, “An Overview of 5G Requirements,” 5G Mob. Commun., pp. 3–26, 2016.

[53] J. L. Carcel, B. Mouhouche, M. Fuentes, E. Garro, and D. Gomez-Barquero, “IMT-2020 key performance indicators: Evaluation and extension towards 5G new radio point-to-multipoint,” in BMSB, 2019, pp. 1–5, doi: 10.1109/BMSB47279.2019.8971948.

[54] A. Tamayo-Dominguez, J.-M. Fernandez-Gonzalez, and M. S. Castaner, “Low-cost millimeter-wave antenna with simultaneous sum and difference patterns for 5G point-to-point communications,” IEEE Commun. Mag., vol. 56, no. 7, pp. 28–34, 2018.

[55] M. A. M. Albreem, “5G wireless communication systems: vision and challenges,” in 2015 International Conference on Computer, Communications, and Control Technology (I4CT), 2015, pp. 493–497.

[56] E. F. Y. Bureau, “How does BDMA technology work in 5G network?,” Electronics For You, 26-Jun-2020. [Online]. Available: https://www.electronicsforu.com/technology-trends/learn-electronics/bdma-technology-5g-network. [Accessed: 05-Apr-2023].

[57] H. Tan, W. Li, T. Wang, J. Fang, and Z. Feng, “The analysis on the candidate frequency bands of future mobile communication systems,” China Commun., vol. 12, no. Supplement, pp. 140–149, 2015.

[58] Y. Wang, J. Li, L. Huang, Y. Jing, A. Georgakopoulos, and P. Demestichas, “5G mobile: Spectrum broadening to higher-frequency bands to support high data rates,” IEEE Veh. Technol. Mag., vol. 9, no. 3, pp. 39–46, 2014.

[59] N. Shoaib, S. Shoaib, R. Y. Khattak, I. Shoaib, X. Chen, and A. Perwaiz, “MIMO antennas for smart 5G devices,” IEEE access, vol. 6, pp. 77014–77021, 2018.

[60] C. Hausl, J. Emmert, M. Mielke, B. Mehlhorn, and C. Rowell, “Mobile network testing of 5G NR FR1 and FR2 networks: Challenges and solutions,” in 2022 16th European Conference on Antennas and Propagation (EuCAP), 2022, pp. 1–5.

[61] S. Bin Iqbal, A. Awada, U. Karabulut, I. Viering, P. Schulz, and G. P. Fettweis, “Analysis and performance evaluation of mobility for multi-panel user equipment in 5G networks,” in 2022 IEEE 95th Vehicular Technology Conference:(VTC2022-Spring), 2022, pp. 1–7.

[62] D. Liu, U. Pfeiffer, J. Grzyb, and B. Gaucher, Advanced Millimeter-Wave Technologies: Antennas, Packaging and Circuits. John Wiley & Sons, 2009.

[63] T. E. Bogale, X. Wang, and L. B. Le, “mmWave Communication Enabling Techniques for 5G Wireless Systems: A Link Level Perspective,” in MmWave Massive MIMO, Elsevier, 2017, pp. 195–225.

[64] K. Y. Kapusuz, A. Vanden Berghe, S. Lemey, and H. Rogier, “Partially filled half-mode substrate integrated waveguide leaky-wave antenna for 24 GHz automotive radar,” IEEE Antennas Wirel. Propag. Lett., vol. 20, no. 1, pp. 33–37, 2020.

[65] N. Ashraf, O. Haraz, M. A. Ashraf, and S. Alshebeili, “28/38-GHz dual-band millimeter wave SIW array antenna with EBG structures for 5G applications,” in 2015 international conference on information and communication technology research (ICTRC), 2015, pp. 5–8.

[66] J. Bruder, J. Carlo, J. Gurney, and J. Gorman, “IEEE standard for letter designations for radar-frequency bands,” IEEE Aerosp. Electron. Syst. Soc., pp. 1–3, 2003.

[67] 5G FR2 Frequency Bands - everything RF [Online], Available: https://www.everythingrf.com/community/5g-fr2-frequency-bands

[68] C.-C. Chong, Millimeter-wave wireless communication systems : theory and applications. New York: New York : Hindawi Pub. Corp., c2007., 2007.

[69] S. O. Tatu and E. Moldovan, “V-band multiport heterodyne receiver for high-speed communication systems,” EURASIP J. Wirel. Commun. Netw., vol. 2007, pp. 1–7, 2006.

[70] T. Rath, “Minimally invasive surgery for the treatment of lung cancer—indications,” MMW Fortschr. Med., vol. 155, no. 13, pp. 38–40, 2013.

[71] K. A. Lukin, “Millimeter wave noise radar applications: Theory and experiment,” in Fourth International Kharkov Symposium’Physics and Engineering of Millimeter and Sub-Millimeter Waves’. Symposium Proceedings (Cat. No. 01EX429), 2001, vol. 1, pp. 68–73.

[72] E. Gonzalez-Sosa, R. Vera-Rodriguez, J. Fierrez, and V. M. Patel, “Exploring body shape from mmw images for person recognition,” IEEE Trans. Inf. Forensics Secur., vol. 12, no. 9, pp. 2078–2089, 2017.

[73] S. Mumtaz, J. Rodriguez, and L. Dai, "MmWave Massive MIMO: A Paradigm for 5G," Academic Press, 2016.

[74] F. Boccardi, R. W. Heath, A. Lozano, T. L. Marzetta, and P. Popovski, “Five disruptive technology directions for 5G,” IEEE Commun. Mag., vol. 52, no. 2, pp. 74–80, 2014.

[75] R. Fisher, “60 GHz WPAN standardization within IEEE 802.15.3c,” in 2007 International Symposium on Signals, Systems and Electronics, 2007, pp. 103–105, doi: 10.1109/ISSSE.2007.4294424.

[76] C. J. Hansen, “WiGiG: Multi-gigabit wireless communications in the 60 GHz band,” IEEE Wirel. Commun., vol. 18, no. 6, pp. 6–7, 2011.

[77] K.-C. Huang and D. J. Edwards, Millimetre wave antennas for gigabit wireless communications: a practical guide to design and analysis in a system context. John Wiley & Sons, 2008.

[78] C. A. Balanis, Antenna Theory: Analysis and Design. John wiley & sons, 2016.

[79] M. Marcus and B. Pattan, “Millimeter wave propagation: spectrum management implications,” IEEE Microw. Mag., vol. 6, no. 2, pp. 54–62, 2005.

[80] K. Chang, RF and Microwave Wireless Systems. New York, NY, USA: Wiley, 2000.

[81] M. Arvas and M. Alsunaidi, “Analysis of oxygen absorption at 60 GHz frequency band,” in 2019 IEEE International Symposium on Antennas and Propagation and USNC-URSI Radio Science Meeting, 2019, pp. 2127–2128.

[82] W. Tashan, I. Shayea, S. Aldirmaz-Colak, T. A. Rahman, A. A. El-Saleh, and M. Roslee, “Rain rate and rain attenuation over millimeter waves in tropical regions based on real measurements,” in 2021 IEEE 15th Malaysia International Conference on Communication (MICC), 2021, pp. 120–125.

[83] J. Wells, "Faster than fiber: The future of multi-G/s wireless," IEEE Microw. Mag., vol. 10, no. 3, pp. 104–112, 2009.

[84] L. Kahana, D. Rozban, M. Gihasi, A. Abramovich, Y. Yitzhaky, and N. Kopeika, “Inexpensive millimeter-wave communication channel using glow discharge detector and satellite dish antenna,” Electronics, vol. 9, no. 4, p. 677, 2020.

[85] J. L. Volakis, Antenna Engineering Handbook. McGraw-Hill Education, 2007.

[86] “Parabola,” Wikipedia, 26-Mar-2023. [Online]. Available: https://en.wikipedia.org/wiki/Parabola. [Accessed: 05-Apr-2023].

[87] M. Cosker, L. Lizzi, F. Ferrero, R. Staraj, and J. Ribero, "Realization of 3-D flexible antennas using liquid metal and additive printing technologies," IEEE Antennas Wirel. Propag. Lett., vol. 16, pp. 971–974, 2017.

[88] S. Ahmed, F. A. Tahir, A. Shamim, and H. M. Cheema, "A compact kapton-based inkjet-printed multiband antenna for flexible wireless devices," IEEE Antennas Wirel. Propag. Lett., vol. 14, pp. 1802–1805, 2015.

[89] H. A. E. Elobaid, S. K. A. Rahim, M. Himdi, X. Castel, and M. A. Kasgari, "A transparent and flexible polymer-fabric tissue UWB antenna for future wireless networks," IEEE Antennas Wirel. Propag. Lett., vol. 16, pp. 1333–1336, 2017.

[90] M. Tang, T. Shi, and R. W. Ziolkowski, "Flexible efficient quasi-yagi printed uniplanar antenna," IEEE Trans. Antennas Propag., vol. 63, no. 12, pp. 5343–5350, 2015.

[91] M. Faridani and R. A. Sadeghzadeh, "Multi-band rectangular monopole microstrip antenna with modified feed junction for microwave wireless applications," in Fundamental Research in Electrical Engineering, 2019, pp. 1009-1015.

[92] J. Colaco and R. Lohani, “Design and implementation of microstrip circular patch antenna for 5G applications,” in 2020 International Conference on Electrical, Communication, and Computer Engineering (ICECCE), 2020, pp. 1–4.

[93] A. Kaur and P. K. Malik, “Multiband elliptical patch fractal and defected ground structures microstrip patch antenna for wireless applications.,” Prog. Electromagn. Res. B, vol. 91, 2021.

[94] M. T. Islam, M. N. Shakib, and N. Misran, “Multi-slotted microstrip patch antenna for wireless communication,” Prog. Electromagn. Res. Lett., vol. 10, pp. 11–18, 2009.

[95] N. Irfan, M. C. E. Yagoub, and K. Hettak, “Design of a microstrip-line-fed inset patch antenna for RFID Applications,” Int. J. Eng. Technol., vol. 4, no. 5, p. 558, 2012.

[96] M. U. Khan, M. S. Sharawi, and R. Mittra, “Microstrip patch antenna miniaturisation techniques: a review,” IET Microwaves, Antennas Propag., vol. 9, no. 9, pp. 913–922, 2015.

[97] I. Singh and V. S. Tripathi, “Micro strip patch antenna and its applications: a survey,” Int. J. Comp. Tech. Appl, vol. 2, no. 5, pp. 1595–1599, 2011.

[98] G. Christina, “A Review on microstrip patch antenna performance improvement techniques on various applications,” J. Trends Comput. Sci. Smart Technol., vol. 3, no. 3, pp. 175–189, 2021.

[99] P. K. Malik, S. Padmanaban, and J. B. Holm-Nielsen, Microstrip Antenna Design for Wireless Applications. CRC Press, 2021.

[100] Z. N. Chen and M. Y. W. Chia, Broadband Planar Antennas: Design and Applications. John Wiley & Sons, 2006.

[101] J. Yang, H. Wang, Z. Lv, and H. Wang, “Design of miniaturized dual-band microstrip antenna for WLAN application,” Sensors, vol. 16, no. 7, p. 983, 2016.

[102] S. Zhong, X. Yan, and X. Liang, “UWB planar antenna technology,” Front. Electr. Electron. Eng. China, vol. 3, pp. 136–144, 2008.

[103] H. F. Abutarboush, H. Nasif, R. Nilavalan, and S. W. Cheung, “Multiband and wideband monopole antenna for GSM900 and other wireless applications,” IEEE Antennas Wirel. Propag. Lett., vol. 11, pp. 539–542, 2012.

[104] M. R. Aghda, M. R. Kamarudin, and H. U. Iddi, “M-shape surrounded with ring patch wideband monopole printed antenna,” Microw. Opt. Technol. Lett., vol. 54, no. 2, pp. 482–486, 2012.

[105] M. Faridani, G. Xiao, R. E. Amaya, N. Javanbakht, and M. C. E. Yagoub, “A kapton-based flexible wideband antenna with metamaterial resonators for millimeter-wave wireless applications,” in 2021 IEEE International Symposium on Antennas and Propagation and USNC-URSI Radio Science Meeting (APS/URSI), 2021, pp. 1055–1056.

[106] M. Midrio, S. Boscolo, F. Sacchetto, C. G. Someda, A. D. Capobianco, and F. M. Pigozzo, “Planar, compact dual-band antenna for wireless LAN applications,” IEEE Antennas Wirel. Propag. Lett., vol. 8, pp. 1234–1237, 2009.

[107] I. Budhiraja, R. Kumar, and M. Pal, “Slotted dual arrowhead multi-band rectangular microstrip patch antenna,” Int. J. Sci. Eng. Res., vol. 3, no. 9, pp. 758–762, 2012.

[108] W. X. An, H. Wong, K. L. Lau, S. F. Li, and Q. Xue, “Design of broadband dual-band dipole for base station antenna,” IEEE Trans. Antennas Propag., vol. 60, no. 3, pp. 1592–1595, 2011.

[109] T. Masri, M. K. Abd Rahim, O. Ayop, F. Zubir, N. A. Samsuri, and H. A. Majid, “Electromagnetic band gap structures incorporate with dual band microstrip antenna array,” Prog. Electromagn. Res. M, vol. 11, pp. 111–122, 2010.

[110] W. C. Mok, S. H. Wong, K. M. Luk, and K. F. Lee, “Single-layer single-patch dual-band and triple-band patch antennas,” IEEE Trans. Antennas Propag., vol. 61, no. 8, pp. 4341–4344, 2013.

[111] “IPhone - supported 5G and LTE Networks,” Apple (Canada). [Online]. Available: https://www.apple.com/ca/iphone/cellular/. [Accessed: 05-Apr-2023].

[112] T. S. Rappaport, "Special session on mmWave communications," presented at the IEEE International Conference on Communications (ICC), Budapest, Hungary, 2013

[113] J. Luo, P. Huang, D. Lei, Z. Li, and L. Li, "Dual-band antenna made of slow-wave substrate integrated waveguide," in 2020 IEEE MTT-S International Microwave Workshop Series on Advanced Materials and Processes for RF and THz Applications (IMWS-AMP), 2020, pp. 1–3, doi: 10.1109/IMWS-AMP49156.2020.9199708.

[114] S. I. Naqvi et al., "An integrated antenna system for 4G and millimeter-wave 5G future handheld devices," IEEE Access, vol. 7, pp. 116555–116566, 2019, doi: 10.1109/ACCESS.2019.2936513.

[115] Z. Wang, G. Zhang, Y. Yin, and J. Wu, “Design of a dual-band high-gain antenna array for WLAN and WiMAX base station,” IEEE Antennas Wirel. Propag. Lett., vol. 13, pp. 1721–1724, 2014.

[116] Y. Cui, R. Li, and P. Wang, “Novel dual-broadband planar antenna and its array for 2G/3G/LTE base stations,” IEEE Trans. Antennas Propag., vol. 61, no. 3, pp. 1132–1139, 2012.

[117] M. Ferrando-Rocher, J. I. Herranz-Herruzo, A. Valero-Nogueira, and M. Baquero-Escudero, “Dual-band single-layer slot array antenna fed by K/Ka-band dual-mode resonators in gap waveguide technology,” IEEE Antennas Wirel. Propag. Lett., vol. 20, no. 3, pp. 416–420, 2021.

[118] C.-X. Mao, S. Gao, Y. Wang, Q.-X. Chu, and X.-X. Yang, “Dual-band circularly polarized shared-aperture array for C -/ X -band satellite communications,” IEEE Trans. Antennas Propag., vol. 65, no. 10, pp. 5171–5178, 2017.

[119] S. He and J. Xie, “Analysis and design of a novel dual-band array antenna with a low profile for 2400/5800-MHz WLAN systems,” IEEE Trans. Antennas Propag., vol. 58, no. 2, pp. 391–396, 2009.

[120] D. S. Bagri, “Pros and cons of using arrays of small antennas versus large single dish antennas for Deep Space Network,” in 2009 IEEE Aerospace conference, 2009, pp. 1–9.

[121] Y.-X. Sun and K. W. Leung, “Substrate-integrated two-port dual-frequency antenna,” IEEE Trans. Antennas Propag., vol. 64, no. 8, pp. 3692–3697, 2016.

[122] Y. Zhu, Y. Chen, and S. Yang, "Integration of 5G rectangular MIMO antenna array and GSM antenna for dual-band base station applications," IEEE Access, vol. 8, pp. 63175–63187, 2020, doi: 10.1109/ACCESS.2020.2984246.

[123] M. Khalid, S. I. Naqvi, Y. Amin, and H. Tenhunen, "An integrated 4G Array with mm-wave 5G MIMO Antenna for Future Mobile applications," in 2020 3rd International Conference on Computing, Mathematics and Engineering Technologies (iCoMET), 2020, pp. 1–6, doi: 10.1109/iCoMET48670.2020.9073898.

[124] Y. Li and J. Wang, "Dual-band leaky-wave antenna based on dual- mode composite microstrip line for microwave and millimeter-wave applications," IEEE Trans. Antennas Propag., vol. 66, no. 4, pp. 1660–1668, 2018, doi: 10.1109/TAP.2018.2800705.

[125] Cornell Ece Open Courseware. [Online]. Available: https://ocw.ece.cornell.edu/courses/ece-3030-electromagnetic-fields-and-waves-2/ece-3030-lectures-notes-and-handouts-2/. [Accessed: 14-Jan-2023].

[126] T. S. Bird, “Reflector Antennas,” Singapore: Springer Singapore, 2016, pp. 853–922.

[127] Axis of symmetry (parabola). [Online]. Available: https://www.learnalberta.ca/content/memg/Division04/Axis%20of%20Symmetry%20(Parabola)/index.html#:~:text=The%20axis%20of%20symmetry%20of,axis%20of%20symmetry%20are%20vertical. [Accessed: 16-Jan-2023].

[128] P. Bevelacqua, “The parabolic reflector antenna (satellite dish),” Parabolic Dish Reflector. [Online]. Available: https://www.antenna-theory.com/antennas/reflectors/dish.php. [Accessed: 14-Jan-2023].

[129] J. W. M. Baars, "The Paraboloidal Reflector Antenna in Radio Astronomy and Communication," vol. 348, Springer, 2007.

[130] E. Notes, “Parabolic reflector antenna gain,” Electronics Notes. [Online]. Available: https://www.electronics-notes.com/articles/antennas-propagation/parabolic-reflector-antenna/antenna-gain-directivity.php. [Accessed: 17-Jan-2023].

[131] B. R. Mahafza, "Radar Systems Analysis and Design Using MATLAB," Chapman and Hall/CRC, 2005.

[132] “Trihedral corner reflector - miwv.com.” [Online]. Available: https://www.miwv.com/wp-content/uploads/2020/06/Trihedral-Reflectors-for-Radar-Applications.pdf. [Accessed: 18-Jan-2023].

[133] H. Rahman, Fundamental Principles of Radar. CRC Press, 2019.

[134] E. F. Knott, J. F. Schaeffer, and M. T. Tulley, "Radar Cross Section," SciTech Publishing, 2004.

[135] D.-I. (F. H. C. Wolff, “Radar basics,” Radar tutorial. [Online]. Available: https://www.radartutorial.eu/17.bauteile/bt47.en.html. [Accessed: 17-Jan-2023].

[136] “Corner reflectors,” Microwaves101. [Online]. Available: https://www.microwaves101.com/encyclopedias/corner-reflectors. [Accessed: 17-Jan-2023].

[137] M. Nagasaka, S. Nakazawa, and S. Tanaka, “Prototype of a dual-circularly polarized parabolic reflector antenna with microstrip antenna array for 12-GHz band satellite broadcasting reception,” in 2016 10th European Conference on Antennas and Propagation (EuCAP), 2016, pp. 1–5.

[138] B. P. A. Mahatmanto and C. Apriono, “Gain performance analysis of a parabolic reflector fed with a rectangular microstrip array antenna,” in 2020 IEEE International Conference on Industry 4.0, Artificial Intelligence, and Communications Technology (IAICT), 2020, pp. 142–145.

[139] R. Mishra, "An Overview of Microstrip Antenna," HCTL Open Int. J. Technol. Innov. Res., vol. 21, no. 2, pp. 39-55, 2016.

[140] S. Chattopadhyay (Ed.), "Trends in Research on Microstrip Antennas," Nov. 2017, doi: 10.5772/65580.

[141] F. Sabath, E. L. Mokole, U. Schenk, and D. Nitsch, Ultra-Wideband, Short-Pulse Electromagnetics 7. Springer, 2007.

[142] S. K. Koul and Z. Wani, Novel Millimetre Wave Antennas for MIMO and 5G Applications. Springer, 2021.

[143] M. Faridani and M. C. E. Yagoub, “Novel planar wideband antenna integrated with compact flat reflector for millimeter-wave communications,” in 2018 Fifth International Conference on Millimeter-Wave and Terahertz Technologies (MMWaTT), 2018, pp. 31–33.

[144] K. Janeczek, G. Kozioł, T. Serzysko, and M. Jakubowska, “Investigation of RFID tag antennas printed on flexible substrates using two types of conductive pastes,” in 3rd Electronics System Integration Technology Conference ESTC, 2010, pp. 1–5.

[145] R. Colella et al., “Comparison of fabrication techniques for flexible UHF RFID tag antennas [wireless corner],” IEEE Antennas Propag. Mag., vol. 59, no. 5, pp. 159–168, 2017.

[146] “Nanovna,” NanoRFE, 05-Jul-2022. [Online]. Available: https://nanorfe.com/nanovna-v2.html. [Accessed: 09-Feb-2023].

[147] Y. Zhou, S. Sivapurapu, M. Swaminathan, and S. K. Sitaraman, “Mechanical and high-frequency electrical study of printed, flexible antenna under deformation,” IEEE Trans. Components, Packag. Manuf. Technol., vol. 10, no. 7, pp. 1088–1100, 2020.

[148] R. Shadid, M. Haerinia, and S. Noghanian, “Study of rotation and bending effects on a flexible hybrid implanted power transfer and wireless antenna system,” Sensors, vol. 20, no. 5, p. 1368, 2020.

[149] Administrator, “Determining positive and negative moment in a beam.: Arch Exam Academy,” Arch Exam Academy | ARE Tutoring - Online ARE Practice Exams, 08-Nov-2013. [Online]. Available: https://archexamacademy.com/determining-positive-and-negative-moment-in-a-beam/. [Accessed: 04-Feb-2023].

[150] Q. H. Dang, S. J. Chen, D. C. Ranasinghe, and C. Fumeaux, “Dual-band reconfigurable flexible antenna with independent frequency tunability,” IEEE Antennas Wirel. Propag. Lett., 2022.

[151] S. J. Chen, T. Kaufmann, and C. Fumeaux, “Wearable textile microstrip patch antenna for multiple ISM band communications,” in 2013 IEEE Antennas and Propagation Society International Symposium (APSURSI), 2013, pp. 1860–1861.

[152] S. J. Chen, C. Fumeaux, B. Chivers, and R. Shepherd, “A 5.8-GHz flexible microstrip-fed slot antenna realized in PEDOT: PSS conductive polymer,” in 2016 IEEE International Symposium on Antennas and Propagation (APSURSI), 2016, pp. 1317–1318.

[153] A. Komolafe et al., “Integrating flexible filament circuits for e-textile applications,” Adv. Mater. Technol., vol. 4, no. 7, p. 1900176, 2019.

[154] A. Refmon Industries, “How is aluminium a material better than copper?,” Refmon_Industries. [Online]. Available: https://www.refmon.in/blog/aluminium-material-better-than-copper#:~:text=A%20More%20Flexible%20Metal,eddy%20losses%20in%20the%20process. [Accessed: 06-Feb-2023].

[155] C. F. Coombs, Printed Circuits Handbook, sixth edition, 6th ed. New York: McGraw-Hill, 2008.

[156] W. F. Avery and Y. Baskin, “Techniques for soldering to aluminum,” Welding Journal, vol. 97, no. 5, pp. 48–54, 2018.

[157] X. Li et al., “Enabling paper-based flexible circuits with aluminium and copper conductors,” Flex. Print. Electron., vol. 4, no. 4, p. 45007, 2019.

[158] M. AL-Haddad, N. Jamel, and A. N. Nordin, “Flexible antenna: a review of design, materials, fabrication, and applications,” in Journal of Physics: Conference Series, 2021, vol. 1878, no. 1, p. 12068.

[159] Rachel, “Techniques for soldering aluminum,” Superior Flux & Mfg. Co., 07-Jun-2018. [Online]. Available: https://superiorflux.com/techniques-for-soldering-aluminum/#:~:text=Aluminum%20needs%20heat%20to%20accept,up%20to%20the%20right%20temperature. [Accessed: 05-Mar-2023].

[160] “210-6 C-FOAM PF-2 & PF-4 - cuming microwave.” [Online]. Available: https://www.cumingmicrowave.com/pdf/210-Dielectrics/210-6%20C-FOAM%20PF-2%20&%20PF-4.pdf [Accessed: 05-Feb-2023].

[161] R. Kumari and B. Choudhury, Multiscale Modelling of Advanced Materials. Springer, 2020.

[162] M. Alibakhshikenari et al., “Impedance bandwidth improvement of a planar antenna based on metamaterial-inspired T-matching network,” IEEE Access, vol. 9, pp. 67916–67927, 2021.

[163] R. Sahoo and D. Vakula, “Gain enhancement of conformal wideband antenna with parasitic elements and low index metamaterial for WiMAX application,” AEU-International J. Electron. Commun., vol. 105, pp. 24–35, 2019.

[164] A. K. Singh, M. P. Abegaonkar, and S. K. Koul, “Miniaturized multiband microstrip patch antenna using metamaterial loading for wireless application,” Prog. Electromagn. Res. C, vol. 83, pp. 71–82, 2018.

[165] Y. Dong and T. Itoh, “Metamaterial-based antennas,” Proc. IEEE, vol. 100, no. 7, pp. 2271–2285, 2012.

[166] C. Caloz and A. Rennings, “Overview of resonant metamaterial antennas,” in 2009 3rd European Conference on Antennas and Propagation, 2009, pp. 615–619.

[167] V. Dehghanian, J. Nielsen, and G. Lachapelle, “Diversity gain through antenna blocking,” Int. J. Antennas Propag., vol. 2012, 2012.

[168] J. Krogerus, J. Toivanen, C. Icheln, and P. Vainikainen, “Effect of the human body on total radiated power and the 3-D radiation pattern of mobile handsets,” IEEE Trans. Instrum. Meas., vol. 56, no. 6, pp. 2375–2385, 2007.

[169] V. Raghavan, M.-L. Chi, M. A. Tassoudji, O. H. Koymen, and J. Li, “Antenna placement and performance tradeoffs with hand blockage in millimeter wave systems,” IEEE Trans. Commun., vol. 67, no. 4, pp. 3082–3096, 2019.

[170] F. Jia, S. Liao, and Q. Xue, "A dual-band dual-polarized antenna array arrangement and its application for base station antennas," IEEE Antennas Wirel. Propag. Lett., vol. 19, no. 6, pp. 972–976, 2020, doi: 10.1109/LAWP.2020.2985171.

[171] W. Chang et al., “Influence of strain on microwave dielectric properties of (Ba, Sr) TiO 3 thin films,” J. Appl. Phys., vol. 87, no. 6, pp. 3044–3049, 2000.

[172] J. Bor, O. Lafond, H. Merlet, P. Le Bars, and M. Himdi, “Technological process to control the foam dielectric constant application to microwave components and antennas,” IEEE Trans. Components, Packag. Manuf. Technol., vol. 4, no. 5, pp. 938–942, 2014.

[173] V. T. Morgan, “The effects of temperature, mechanical pressure and air pressure on the dielectric properties of multilayers of dry kraft paper,” in Proceedings of 1994 4th International Conference on Properties and Applications of Dielectric Materials (ICPADM), 1994, vol. 2, pp. 884–886.

[174] Libretexts, “2.3: Spherical Mirrors,” Physics LibreTexts, 12-Sep-2022. [Online]. Available: https://phys.libretexts.org/Bookshelves/University_Physics/Book%3A_University_Physics_(OpenStax)/University_Physics_III_-_Optics_and_Modern_Physics_(OpenStax)/02%3A_Geometric_Optics_and_Image_Formation/2.03%3A_Spherical_Mirrors#:~:text=R%3DCF%2BFP.&text=In%20other%20words%2C%20in%20the,f%3DR2. [Accessed: 16-Feb-2023].

[175] V. Boljanovic, “Sheet Metal Forming Processes and Die Design,” Industrial Press Inc., 2004.

[176] A. Telsang, B. V Srividya, and S. Vedargarbham, “A study on reflector antennas and design of reflector antenna for 5GHz band,” Int. Res. J. Eng. Technol., vol. 4, no. 07, 2017.

[177] krn5, “CST Studio Suite 3D EM Simulation and Analysis Software,” 3D EM simulation and analysis software. [Online]. Available: https://www.3ds.com/products-services/simulia/products/cst-studio-suite/. [Accessed: 20-Feb-2023].

[178] H. R. Bindhu and M. N. Sujatha, “Wideband slot antenna gain enhancement using metasurface reflector,” Glob. Transitions Proc., vol. 2, no. 2, pp. 344–349, 2021.

[179] S. Jana and A. Ghosh, “Design of a single-layered Ka-band reflectarray antenna using ‘E’-shaped elements for gain enhancement,” in 2021 10th International Conference on Internet of Everything, Microwave Engineering, Communication and Networks (IEMECON), 2021, pp. 1–5.

[180] P. Jiang, W. Jiang, and S. Gong, “A mesh-type low RCS reflectarray antenna based on spoof surface plasmon polariton,” IEEE Antennas Wirel. Propag. Lett., vol. 20, no. 2, pp. 224–228, 2020.

[181] R. Deng, F. Yang, S. Xu, and M. Li, “A low-cost metal-only reflectarray using modified slot-type Phoenix element with 360° phase coverage,” IEEE Trans. Antennas Propag., vol. 64, no. 4, pp. 1556–1560, 2016.

[182] K. Chang and L.-H. Hsieh, Microwave Ring Circuits and Related Structures, vol. 156. John Wiley & Sons, 2004.

[183] J. B. Pendry, A. J. Holden, D. J. Robbins, and W. J. Stewart, “Magnetism from conductors and enhanced nonlinear phenomena,” IEEE Trans. Microw. Theory Tech., vol. 47, no. 11, pp. 2075–2084, 1999.

[184] D. Computer Simulation Technology (CST), “Accuracy in simulation with CST Studio Suite 2016,” Microwave Journal, 28-Sep-2018. [Online]. Available: https://www.microwavejournal.com/articles/25734-accuracy-in-simulation-with-cst-studio-suite-2016. [Accessed: 11-Feb-2023].

[185] D. Imran et al., “Millimeter wave microstrip patch antenna for 5G mobile communication,” in 2018 international conference on engineering and emerging technologies (ICEET), 2018, pp. 1–6.

[186] M. Faridani and M. C. E. Yagoub, “12-Element wideband microstrip array antenna for high data rate terahertz communications,” Optik (Stuttg)., vol. 171, pp. 886–890, 2018, doi: https://doi.org/10.1016/j.ijleo.2018.06.136.

[187] G. Chittimoju and U. D. Yalavarthi, “A comprehensive review on millimeter waves applications and antennas,” in Journal of Physics: Conference Series, 2021, vol. 1804, no. 1, p. 12205.

[188] C.-Z. Han, G.-L. Huang, and T. Yuan, “A dual-band millimeter-wave antenna for 5G mobile applications,” in 2019 IEEE International symposium on antennas and propagation and USNC-URSI Radio science meeting, 2019, pp. 1083–1084.

[189] Y. Sun, X. Yang, M. Yang, and X. Sun, “77GHz CPWG-feed antenna array for applications of imaging radar,” in 2021 13th International Symposium on Antennas, Propagation and EM Theory (ISAPE), 2021, pp. 1–3.

[190] M. Alvandian, M. Fakharzadeh, and M. R. Naeini, “Coupling reduction of printed Yagi antenna arrays for millimeter-wave imaging applications,” in 2019 IEEE International Symposium on Antennas and Propagation and USNC-URSI Radio Science Meeting, 2019, pp. 1767–1768.

[191] J. Coonrod, “Microwave PCB Structure Considerations: Microstrip vs. Grounded Coplanar Waveguide,” 2015.

[192] Q. Lu, L. Zhou, C. Tan, and L. Guanghua, “A novel wide beam UWB antenna design for Through-the-Wall radar,” in 2010 International Conference on Microwave and Millimeter Wave Technology, pp. 1912–1915, 2010.

[193] X. Q. Yang, Y. Y. Zhai, C. Xu, and G. Z. Jia, “Design of antipodal Vivaldi antenna with better performances for ultra wideband applications,” Int. J. Appl. Electromagn. Mech., vol. 46, no. 3, pp. 527–536, 2014.

[194] S. Ahdi Rezaeieh and M. Kartal, “Miniaturized leaf-shaped monopole antenna with filtering properties,” Microw. Opt. Technol. Lett., vol. 54, no. 11, pp. 2638–2642, 2012.

[195] W. Cao, B. Zhang, A. Liu, T. Yu, D. Guo, and Y. Wei, “Broadband high-gain periodic endfire antenna by using I-shaped resonator (ISR) structures,” IEEE Antennas Wirel. Propag. Lett., vol. 11, pp. 1470–1473, 2012.

[196] H. Wang, S.-F. Liu, L. Chen, W.-T. Li, and X.-W. Shi, “Gain enhancement for broadband vertical planar printed antenna with H-shaped resonator structures,” IEEE Trans. Antennas Propag., vol. 62, no. 8, pp. 4411–4415, 2014.

[197] A. Kumar, S. Dwari, G. P. Pandey, B. K. Kanaujia, and D. K. Singh, “A high gain wideband circularly polarized microstrip antenna,” Int. J. Microw. Wirel. Technol., vol. 12, no. 7, pp. 678–687, Sep. 2020.

[198] R. V. S. Ram Krishna and R. Kumar, “Slotted ground microstrip antenna with FSS reflector for high-gain horizontal polarisation,” Electron. Lett., vol. 51, no. 8, pp. 599–600, 2015.

[199] S. K. Sharma and L. Shafai, “Printed Antennas for Wireless Communications,” 1st ed., Chichester, UK: Wiley, 2010, pp. 215–261.

[200] S. Kampeephat, P. Kamphikul, W. Silabut, and R. Wongsan, “Improving the gain of monopole antenna using wire medium structure and dielectric,” in 2019 8th Asia-Pacific Conference on Antennas and Propagation (APCAP), 2019, pp. 422–423.

[201] S. N. Makarov, V. Iyer, S. Kulkarni, and S. R. Best, Antenna and EM Modeling with MATLAB Antenna Toolbox. John Wiley & Sons, 2021.

[202] V. N. Analyzer, "Operation Manual," Anritsu, P, no. 10410-00252, 2007.

[203] E. Notes, “How to calibrate a vector network analyzer, VNA,” Electronics Notes. [Online]. Available: https://www.electronics-notes.com/articles/test-methods/rf-vector-network-analyzer-vna/how-to-calibrate-vna.php. [Accessed: 05-Apr-2023].

[204] S. Zhang, C. C. Njoku, W. G. Whittow, and J. C. Vardaxoglou, “Novel 3D printed synthetic dielectric substrates,” Microw. Opt. Technol. Lett., vol. 57, no. 10, pp. 2344–2346, 2015.

[205] A. Petosa, "Dielectric Resonator Antenna Handbook," Artech House, Boston, 2007.

[206] W. Zhang, Y.-C. Jiao, B. Yang, and Z. Hong, “CPW-fed ultrawideband antenna with 3.5/5.5 GHz dual band-notched characteristics,” in 2011 IEEE International Conference on Microwave Technology & Computational Electromagnetics, 2011, pp. 327–330.

[207] “70-meter dish,” NASA. [Online]. Available: https://nasa3d.arc.nasa.gov/detail/70-meter-dish. [Accessed: 05-Apr-2023].

[208] E. Pittella, L. D’Alvia, E. Palermo, and E. Piuzzi, “Microwave characterization of 3D printed PLA and PLA/CNT composites,” in 2021 IEEE 6th International Forum on Research and Technology for Society and Industry (RTSI), 2021, pp. 52–56.

[209] H. Liao, R. M. Bilal, and A. Shamim, “A large frequency ratio dual-band microstrip antenna with consistent radiation pattern for Internet of Sea applications,” in 2021 15th European Conference on Antennas and Propagation (EuCAP), 2021, pp. 1–5.

[210] X. Tan, W. Wang, Y. Wu, Y. Liu, and A. A. Kishk, "Enhancing isolation in dual-band meander-line multiple antenna by employing split EBG structure," IEEE Trans. Antennas Propag., vol. 67, no. 4, pp. 2769–2774, 2019, doi: 10.1109/TAP.2019.2897489.

[211] D. Wei, J. Li, J. Liu, G. Yang, and W. Zhang, "Dual-band substrate-integrated waveguide leaky-wave antenna with a simple feeding way," IEEE Antennas Wirel. Propag. Lett., vol. 18, no. 4, pp. 591–595, 2019, doi: 10.1109/LAWP.2019.2897163.

[212] P. Prakash, M. P. Abegaonkar, A. Basu, and S. K. Koul, “Gain enhancement of a CPW-fed monopole antenna using polarization-insensitive AMC structure,” IEEE Antennas Wirel. Propag. Lett., vol. 12, pp. 1315–1318, 2013.

[213] R. A. Abdulhasan, R. Alias, K. N. Ramli, F. C. Seman, and R. A. Abd-Alhameed, “High gain CPW-fed UWB planar monopole antenna-based compact uniplanar frequency selective

surface for microwave imaging," Int. J. RF Microw. Comput. Eng., vol. 29, no. 8, p. e21757, 2019.

[214] R. V. S. Ram Krishna and R. Kumar, "Slotted ground microstrip antenna with FSS reflector for high-gain horizontal polarisation," Electron. Lett., vol. 51, no. 8, pp. 599–600, 2015.